



Defence Research and
Development Canada

Recherche et développement
pour la défense Canada



Aerodynamics of flapping wings

Aero-NAV project final report

François Lesage
Nicolas Hamel
DRDC Valcartier

Weixing Yuan
Patrick Zdunich
Richard Lee
NRC - Aerospace

Defence Research and Development Canada – Valcartier

Technical Report

DRDC Valcartier TR 2013-012

August 2013

Canada

Aerodynamics of flapping wings

Aero-NAV project final report

François Lesage
Nicolas Hamel
DRDC Valcartier

Weixing Yuan
Patrick Zdunich
Richard Lee
NRC - Aerospace

Defence Research and Development Canada – Valcartier

Technical Report
DRDC Valcartier TR 2013-012
August 2013

IMPORTANT INFORMATIVE STATEMENTS

- © Her Majesty the Queen in Right of Canada, as represented by the Minister of National Defence, 2013
- © Sa Majesté la Reine (en droit du Canada), telle que représentée par le ministre de la Défense nationale, 2013

Abstract

The development of a new class of military systems known as Nano Air Vehicle (NAV) (7.5 cm and 10 g) is possible in the not too distant future as a result of technological progress in a number of areas. The NAVs will likely use flapping wings as there is strong evidence that, for very small craft, flapping-wing performance is superior to other options due to dynamic effects. This report summarizes the work done under the Aero-NAV project, a Technology Investment Fund project that investigated flapping wing aerodynamics for NAV applications. A vehicle concept was defined in order for the project to focus on particular dimensions, motion characteristics, and performance parameters. From this concept, simpler test cases were defined to assist in understanding the physical phenomena. Tools and capabilities were developed by combining high-accuracy predictions and experimentations with engineering modelling. The detailed flow physics were captured using a highly accurate unsteady CFD solution at low Reynolds number. A tailored experimental facility (water tunnel at NRC) was developed for flapping wings operating at high frequency with a complex 3-dimensional pattern. A less computationally intensive engineering-type method (Vortex Lattice Method) capable of capturing the fundamental aerodynamics and approximating the forces and moments generated over a wide range of wing motions, was developed and used to identify optimum wing shape and motion. Optimization results were obtained for multiple flexible wings giving a thrust-to-power ratio of 19.3 g/W.

Résumé

Le développement d'une nouvelle classe de systèmes militaires connus sous le nom Nano Air Vehicle (NAV) (7,5 cm et 10 g) est possible dans un avenir pas trop lointain, à la suite des progrès technologiques dans un certain nombre de domaines. Ils utiliseront probablement des ailes battantes comme il y a des preuves solides que pour les très petits véhicules, la performance des ailes battantes est supérieure à d'autres options en raison des effets dynamiques. Ce rapport résume le travail réalisé dans le cadre du projet Aero-NAV, un projet du Fonds d'investissement technologique qui a étudié l'aérodynamique du battement d'aile pour des applications NAV. On a défini un concept de véhicule pour que le projet se concentre sur des dimensions, caractéristiques de mouvement et paramètres de performance particuliers. À partir de ce concept, on a défini des cas test simples pour aider à la compréhension des phénomènes physiques. On a développé des outils et des capacités en combinant des prédictions et des expérimentations de haute précision avec la modélisation d'ingénierie. On a capturé la physique détaillée des fluides à l'aide d'une solution CFD instationnaire à bas nombre de Reynolds. On a développé une installation expérimentale sur mesure (tunnel hydraulique au CNRC) pour des ailes battantes à haute fréquence avec un mouvement tridimensionnel complexe. On a développé une méthode d'ingénierie (méthode Vortex Lattice) demandant moins de capacité de calcul, capable de capturer l'aérodynamique fondamentale et d'approximer les forces et de moments engendrés sur une large gamme de mouvements d'ailes. On a utilisé celle-ci pour identifier une forme d'aile et de mouvement optimale. On a obtenu des résultats d'optimisation pour des ailes flexibles multiples donnant un rapport poussée-puissance de 19,3 g/W.

This page intentionally left blank.

Executive summary

Aerodynamics of flapping wings: Aero-NAV project final report

**Francois Lesage; Nicolas Hamel; Weixing Yuan; Patrick Zdunich; Richard Lee;
DRDC Valcartier TR 2013-012; Defence R&D Canada – Valcartier; August 2013.**

The development of a new class of military systems known as Nano Air Vehicle (NAV) (smaller than 7.5 cm and less than 10 grams) is possible in the not too distant future as a result of technological progress in a number of areas. Their potential, with their small size and hover capability, opens up new possibilities in the formulation of military strategies with respect to information superiority in urban operations. Their distinct flight envelope will include hover, perching, and other high agility manoeuvres. The real mission niche for these small aircraft may well be indoors where there is no existing reconnaissance asset available for area surveillance.

These vehicles will likely use flapping wings as there is strong evidence that for very small craft, flapping-wing performance is superior to other options due to dynamic effects. Insect flight has been successful in nature for millions of years and relies on unsteady aerodynamics to produce high lift coefficients and excellent maneuverability. An essential step towards engineering realization of flapping-wing flight is the understanding of the issues for the fully three-dimensional (3-D) motion representative of insect wing beat kinematics.

This report summarizes the work done under the Aero-NAV project, a Technology Investment Fund project that investigated flapping wing aerodynamics for NAV applications. A vehicle concept was defined in order for the project to focus on particular dimensions, motion characteristics and performance parameters. From this concept, simpler test cases were defined to assist in understanding the physical phenomena. Tools and capabilities were developed by combining high-accuracy predictions and experimentations with engineering modelling. The detailed flow physics were captured using a highly accurate unsteady CFD solution at low Reynolds number. A tailored experimental facility (water tunnel at NRC) was developed for flapping wings operating at high frequency with a complex 3-dimensional pattern. A less computationally-intensive engineering-type method (Vortex Lattice Method) capable of capturing the fundamental aerodynamics and approximating the forces and moments generated over a wide range of wing motions, was developed and used to identify optimum wing shape and motion.

The main successes are: (1) the definition of the general characteristics of a notional NAV, (2) the analysis of high amplitude flapping and twisting motion typical of hovering and not studied previously elsewhere, (3) the identification, through optimization with the engineering method, of several complex 3D flexible wing planforms and flapping kinematics producing significantly improved thrust-to-power ratio, (4) an engineering method calibrated with higher-accuracy results from CFD and water tunnel, (5) water tunnel experiments using a larger wing and a lower flapping frequency allowing a match of the three main non-dimensional parameters: Reynolds number, reduced frequency and flapping amplitude to chord ratio, and (6) successful but challenging CFD solution of the complex and large amplitude motion of the wing and the time dependent generation of the leading edge vortex and its subsequent trajectory past the airfoil, with requirements on high grid resolution and accurate viscous closure models.

The follow-on to this project would still be at the level of basic research. The tools and the optimised configurations developed in the TIF project are expected to serve in further analyses.

The impact of the project on Canadian Defence is to provide advice on the potential and the perspectives of nano-air-vehicle for future military applications. These systems are not likely to exist in the battlefield for several years but when they become available they are expected to have a significant impact on information superiority in urban operations.

Sommaire

Aerodynamics of flapping wings : Aero-NAV project final report

Francois Lesage ; Nicolas Hamel ; Weixing Yuan ; Patrick Zdunich ; Richard Lee ; DRDC Valcartier TR 2013-012 ; R & D pour la défense Canada – Valcartier; août 2013.

Le développement d'une nouvelle classe de systèmes militaires connus sous le nom Nano Air Vehicle (NAV) (moins de 7,5 cm et de moins de 10 grammes) est possible dans un avenir pas trop lointain, à la suite des progrès technologiques dans un certain nombre de domaines. Leur potentiel, de par leur petite taille et capacité de vol stationnaire, ouvre de nouvelles possibilités dans la formulation des stratégies militaires à l'égard de maîtrise de l'information dans les opérations urbaines. Leur enveloppe de vol distincte comprendra vol stationnaire, se percher, et d'autres manœuvres d'agilité élevés. Le vrai créneau de mission de ces petits véhicules pourrait bien être à l'intérieur où il n'y a pas de d'éléments de reconnaissance existant pour la surveillance de zone.

Ils utiliseront probablement des ailes battantes comme il y a des preuves solides que pour les très petits véhicules, la performance des ailes battantes est supérieure à d'autres options en raison des effets dynamiques. Le vol de l'insecte est un succès dans la nature depuis des millions d'années et s'appuie sur l'aérodynamique instationnaire pour produire des coefficients de portance élevée et une excellente maniabilité. Une étape essentielle vers la réalisation de l'ingénierie du vol par ailes battantes est de mieux comprendre les enjeux du mouvement tridimensionnel représentatif de la cinématique du battement d'aile d'insectes.

Ce rapport résume le travail réalisé dans le cadre du projet Aero-NAV, un projet du Fonds d'investissement technologique qui a étudié l'aérodynamique du battement d'aile pour des applications NAV. On a défini un concept de véhicule pour que le projet se concentre sur des dimensions, caractéristiques de mouvement et paramètres de performance particuliers. A partir de ce concept, on a défini des cas test simples pour aider à la compréhension des phénomènes physiques. On a développé des outils et des capacités en combinant des prédictions et des expérimentations de haute précision avec la modélisation d'ingénierie. On a capturé la physique détaillée des fluides à l'aide d'une solution CFD instationnaire à bas nombre de Reynolds. On a développé une installation expérimentale sur mesure (tunnel hydraulique au CNRC) pour des ailes battantes à haute fréquence avec un mouvement tridimensionnel complexe. On a développé une méthode d'ingénierie (méthode Vortex Lattice) demandant moins de capacité de calcul, capable de capturer l'aérodynamique fondamentale et d'approximer les forces et de moments engendrés sur une large gamme de mouvements d'ailes. On a utilisé celle-ci pour identifier une forme d'aile et de mouvement optimale.

Les principaux succès sont les suivants: (1) la définition des caractéristiques générales d'un NAV notionnel, (2) l'analyse du mouvement de battement et de torsion de forte amplitude typique de vol stationnaire et pas étudié auparavant ailleurs, (3) l'identification, par optimisation de la méthode d'ingénierie, de plusieurs formes 3D complexes d'ailes flexibles et des cinématiques de battement produisant un rapport poussée-puissance nettement améliorée, (4) une méthode d'ingénierie calibrée avec des résultats de grande précision en provenance de CFD et tunnel

hydraulique, (5) des expériences de tunnel hydraulique utilisant une plus grande aile et une plus faible fréquence de battement permettant une concordance pour les trois principaux paramètres sans dimension: le nombre de Reynolds, la fréquence réduite et le rapport amplitude de battement à la corde, et (6) une solution CFD efficace mais remplie de défis du mouvement complexe et d'amplitude importante de l'aile et de la génération du tourbillon de bord d'attaque en fonction du temps et de sa trajectoire ultérieure passé la voilure, avec les exigences en matière de résolution élevée de grille et des modèles précis de fermeture visqueux.

La suite donnée à ce projet serait encore au stade de la recherche fondamentale. Les outils et les configurations optimisées développées dans le projet FIT pourront servir à d'autres analyses.

L'impact du projet sur la défense canadienne est de fournir des conseils sur le potentiel et les perspectives des NAVs pour de futures applications militaires. Il est peu probable que ces systèmes existeront dans le champ de bataille avant plusieurs années, mais quand ils seront disponibles, ils devraient avoir un impact significatif sur la supériorité d'information dans les opérations urbaines.

Table of contents

Abstract	i
Résumé	i
Executive summary	iii
Sommaire	v
Table of contents	vii
List of figures	x
List of tables	xiii
1 Introduction.....	1
2 Notional nano-air vehicle defined.....	3
2.1 Concept definition	3
2.2 Flapping Kinematics.....	6
2.3 Dimensionless Parameters for NAV.....	7
2.3.1 Reynolds Number	7
2.3.1.1 Reynolds number based on frequency	7
2.3.1.2 Reynolds number based on RMS wing speed.....	8
2.3.1.3 Reynolds number based on combined freestream and plunging- induced velocity	8
2.3.1.4 Reynolds Number for notional NAV	8
2.3.2 Reduced Frequency	10
2.3.3 Flap Amplitude to Chord Ratio	10
3 2D standard test cases.....	11
3.1 Rigid airfoil in air	11
3.2 Rigid airfoil in water	12
3.3 Rigid airfoil in water with reflection planes.....	14
3.4 Flexible airfoil with single torsion joint in water	15
3.5 Flexible cambered airfoil in water.....	15
4 3D standard test cases.....	17
4.1 Wing geometry	17
4.2 Flapping Kinematics.....	19
4.3 Non-dimensional parameters.....	20
5 2D and 3D water tunnel testing	23
5.1 Water Tunnel.....	23
5.2 Setup for the Standard 2D Test Case.....	23
5.3 2D flexible wing model	25
5.4 Setup for the Standard 3D Test Case.....	25
6 CFD computations setup.....	29
6.1 INSFlow computations.....	29

6.1.1	Flow solver	29
6.1.2	Setup for the Standard 2D Test Case	29
6.1.3	Setup for the Standard 3D Test Case	30
6.2	Fluent	30
7	Water tunnel and CFD results	33
7.1	Standard 2D Test Case	33
7.1.1	Drag and Lift Forces	33
7.1.2	Flowfield over the NACA 0005 Airfoil	34
7.1.3	Effect of Cross-Sectional Profile	37
7.2	Standard 2D Test Case with reflection planes	38
7.3	Flexible cambered thin airfoil results	44
7.4	Standard 3D Test Case	48
7.4.1	Lift and Drag Forces	48
7.4.2	Effect of Cross-Sectional Profile	49
7.5	Remarks	49
8	Engineering design and optimization tool	51
8.1	2D model	51
8.1.1	Attached flow model	51
8.1.1.1	Application of Attached Flow Model	52
8.1.2	Separated Flow Model	53
8.1.2.1	Stall Angle of Attack	53
8.1.2.2	Stall Location	54
8.1.2.3	Stall (LEV) Model	54
8.1.2.4	Application of the Separated Flow Model	55
8.1.3	Output from the code	58
8.2	3D model	59
9	Optimum flapping motions identified from VLM	61
9.1	Optimization in two dimensions	61
9.1.1	Target disk loading	61
9.1.2	Thrust relationship to V^2	61
9.1.3	Single variable optimization	61
9.1.4	Multi-variable optimization	62
9.2	Optimization in three dimensions	63
9.2.1	NAV flexible wing optimization (flap < 40 degrees)	64
9.2.2	NAV flexible wing optimization (using clap-fling)	66
10	Fluid-structure interaction for flexible flapping airfoils in 2D	69
10.1	Aeroelastic study of multi-segment wings in 2D	69
10.2	Fluid-structure interaction using OpenFOAM	70
11	Conclusion and recommendations	73
11.1	Novelty, Technical Advances, Knowledge Gained	73
11.2	Project Successes	74

11.3	Intellectual Property	74
11.4	Impact of the Project	74
11.5	Follow-on Plans.....	75
11.6	Recommendations	75
12	References.....	77
	List of symbols/acronyms.....	81

List of figures

Figure 1: From a vehicle concept to simpler test cases	2
Figure 2: Analysis methods from water tunnel to optimized configurations	2
Figure 3: Representative NAV.	4
Figure 4: Description of airfoil flapping showing pitching and plunging	7
Figure 5: Time history of the effective angle of attack in accordance with the pitching-plunging motion of the airfoil. The letters at top correspond to the letters appearing in Figure 20 and Figure 21	14
Figure 6: Leading and trailing edge position for 2D test in water	15
Figure 7: A scale schematic showing 3D wing planform including flap axis, water level, root chord, tip chord and span. All dimensions are in mm. Redundant dimensions are shown in grey.	18
Figure 8: Scale drawings showing the 3D test case geometry in the water tunnel.....	19
Figure 9: Eidetics Flow Visualization Water Tunnel at the NRC Institute of Aerospace Research.	23
Figure 10: Left: the 2-DOF motion rig; Right: the two-dimensional airfoil model between two reflection planes	24
Figure 11: Calibration setup and the flexible wing in test section	25
Figure 12: The 3-DOF motion rig	26
Figure 13: The three-dimensional wing model is installed in the balance.	27
Figure 14: The bi-fold five-component balance used for the standard 3D test case	27
Figure 15: First moving mesh technique, in red the pitching & heaving zone (rigid body motion), in green the heaving zone (grid layering) and in purple the stationary part .	31
Figure 16: Second moving mesh technique, rigid body motion only	31
Figure 17: Vortices shed by the heaving NACA 0012 airfoil $Re=20\,000$, (a) experimental, (b) numerical laminar, (c) numerical turbulent and (d) Fluent laminar	32
Figure 18: Lift and drag coefficient of the heaving and pitching NACA 0012 airfoil	32
Figure 19: Measured and computed drag and lift forces for the pitching-plunging NACA 0005 airfoil. Standard 2D test case (wing span 25.4cm). The shaded band represents uncertainty in the lift measurement. The letters represent the occurrence of the PIV and CFD results shown in the next Figure.....	33
Figure 20: Downstroke : Experimental (left) and computed (right) spanwise vorticity (ω_z) distribution over the pitching-plunging NACA 0005 airfoil. Standard 2D test case; The temporal occurrence of each frame is identified in the previous Figure. The abbreviation “LEV” represents “leading-edge vortex”; the subscripts “L” and “U” represent lower and upper surface, respectively.	35

Figure 21:Upstroke (Continued from previous Figure).....	36
Figure 22: Measured lift force for pitching-plunging NACA 0005 and flat-plate airfoils. Standard 2D test case.	38
Figure 23: The setup of the reflection planes simulates clap-fling wing-wing interaction	39
Figure 24: Downstroke; at left and centre are spanwise vorticity (ω_z) distributions over the pitching-plunging NACA 0005 airfoil at $Re = 10.5 \times 10^3$, with reflection planes at 1.03c from the central position.....	40
Figure 25: Upstroke: Continued from previous figure	41
Figure 26: Computed lift coefficients compared with experimental results for the case with reflection planes located at 1.03c from the central position.....	42
Figure 27: Effect of the proximity of the reflection plane on the lift and drag coefficients.....	42
Figure 28: Computed spanwise vorticity (ω_z) distribution over the pitching-plunging NACA 0005 airfoil at $Re = 10.5 \times 10^3$, with reflection planes at 1.15c	43
Figure 29: Computed aerodynamic coefficients of the cambered airfoil in comparison with NACA 0005 airfoil.....	44
Figure 30: Downstroke: Computed dimensionless pressure distribution over the airfoils at Re $= 10.5 \times 10^3$, $V_\infty = 0.0635$ m/s, second-order CFD solution.....	45
Figure 31: Upstroke: Continued from previous figure	46
Figure 32: Computed spanwise vorticity (ω_z) distribution over the flexible cambered thin airfoil at $Re = 10.5 \times 10^3$, $V_\infty = 0.0635$ m/s, second-order CFD solution.....	47
Figure 33: Measured and computed lift and drag forces for the flapping NACA 0005 wing. Standard 3D test case; The shaded bands represent the uncertainty in the lift and drag measurements.....	48
Figure 34: Measured lift and drag forces for flapping NACA 0005 and flat plate wings. Standard 3D test case: $V_\infty = 0.0635$ m/s, $Re_f = 14.3 \times 10^3$, $f = 0.46$ Hz.....	49
Figure 35: Drag coefficient comparisons between the attached-flow panel model and Fluent. Note the slight phase shift and discrepancies at the extremes of thrust/drag production.	52
Figure 36: Attached-flow panel method to compare drag coefficient for a range of reduced frequencies that cover fast forward flight to near-hover.	53
Figure 37: The separated-flow panel model captures the jog in the drag portion of the cycle, where initially drag production is decreased then increased. The attached-flow solution is plotted for comparison.	56
Figure 38: Low reduced frequency case ($k=0.1$) comparison of panel model to Fluent Navier Stokes solution.	57
Figure 39: High reduced frequency case ($k=10$) comparison of panel model to Fluent Navier- Stokes solution.	57
Figure 40: Forces resulting from fish-tail type optimum (2D).....	63

Figure 41:Optimal planform for flexible NAV wing	65
Figure 42: Rear view showing "time-lapse" of the wing's TE deformation	66
Figure 43: Computed vorticity field in propulsion regime at three instants over a flapping cycle, comparing a totally rigid wing (on the left) to two flexible wings.	70
Figure 44: Case 100 : vorticity (top left) and pressure (top right) fields; instantaneous thrust (bottom left) and power (bottom right) coefficients.....	71

List of tables

Table 1: Dimensions of representative NAV	5
Table 2: Notional mass breakdown for the conceptual NAV	5
Table 3: Calculated parameters of representative NAV	11
Table 4: Parameters for 2D test cases in air and in water.....	13
Table 5: Parameters for 3D test case in water	20
Table 6: PIV recording parameters for the 2D test case.....	25
Table 7: Balance characteristics	26
Table 8: Summary of clap-fling (wing-wing interaction) effect (1 st -order CFD results)	43
Table 9: Aerodynamic performance of the cambered airfoil (2 nd -order CFD results)	44

This page intentionally left blank.

1 Introduction

The development and acquisition of a new class of military systems known as Nano Air Vehicle (NAV) (smaller than 7.5 cm and less than 10 grams) is possible in the not too distant future as a result of technological progress in a number of areas such as aerodynamics, micro-electronics, sensors, micro-electromechanical systems and micro-manufacturing. The potential of nano air vehicles, with their small size and hover capability, opens up new possibilities in the formulation of military strategies with respect to information superiority in urban operations. Their distinct flight envelope will include hover, perching, and other high agility manoeuvres. The real mission niche for these small aircraft may well be indoors where there is no existing reconnaissance asset available for area surveillance.

These vehicles will likely use flapping wings as there is strong evidence that for very small craft, flapping-wing performance is superior to other options due to dynamic effects that create much higher average lift at low Reynolds numbers. Insect flight has been successful in nature for millions of years and relies on unsteady aerodynamics to produce high lift coefficients and excellent maneuverability. Insects fly by oscillating (plunging) and rotating (pitching) their wings through large angles, while sweeping them forwards and backwards. The dramatic lift-boosting unsteady aerodynamic phenomena that are exploited by insect flapping wings are however not yet fully understood. An essential step towards engineering realization of flapping-wing flight is the understanding of the issues for the fully three-dimensional (3-D) motion representative of insect wing beat kinematics.

The Aero-NAV TIF project at DRDC Valcartier investigated flapping wing aerodynamics for NAV applications. Tools and capabilities were developed by combining high-accuracy predictions and experimentations with engineering modelling. The detailed flow physics were captured using a highly accurate unsteady CFD solution at low Reynolds number. A tailored experimental facility (water tunnel at the Institute for Aerospace Research of NRC) was developed for flapping wings operating at high frequency with a complex 3-dimensional pattern. A less computationally-intensive engineering-type method (Vortex lattice method) capable of capturing the fundamental aerodynamics and approximating the forces and moments generated over a wide range of wing motions, was developed and used to identify optimum wing shape and motion.

A vehicle concept was initially defined in order for the project to focus on particular dimensions, motion characteristics and performance parameters. From this concept, simpler test cases were then defined to assist in understanding the physical phenomena through water tunnel tests or CFD: a two-dimensional rigid wing, a three-dimensional rigid wing and a two-dimensional flexible wing (Figure 1). The water tunnel was used to test these configurations in water. CFD was applied to the same configurations in water for validation and further computations were done in air. The Vortex Lattice Method then used the water tunnel results and the CFD results for calibrating some parameters (leading edge suction efficiency, friction drag coefficient, stall trigger angle, nascent leading edge vortex calibration factor). Once calibrated, the VLM was used to estimate optimised wing shape and motion for a vehicle with rigid wings, flexible wings, and flexible wings using wing interactions (clap-fling). The process from water tunnel testing to optimised configurations is depicted in Figure 2.

This is the final report of the Aero-NAV project. It summarizes the work done during the four years of the project (2006-2010). During that period, thirty-two documents were published [1]-[33]. The reader is referred to these documents for further details.

This work was carried out under the Technology Investment Fund project “Flapping wings for nano air vehicles – Aero-NAV” (12pz12).

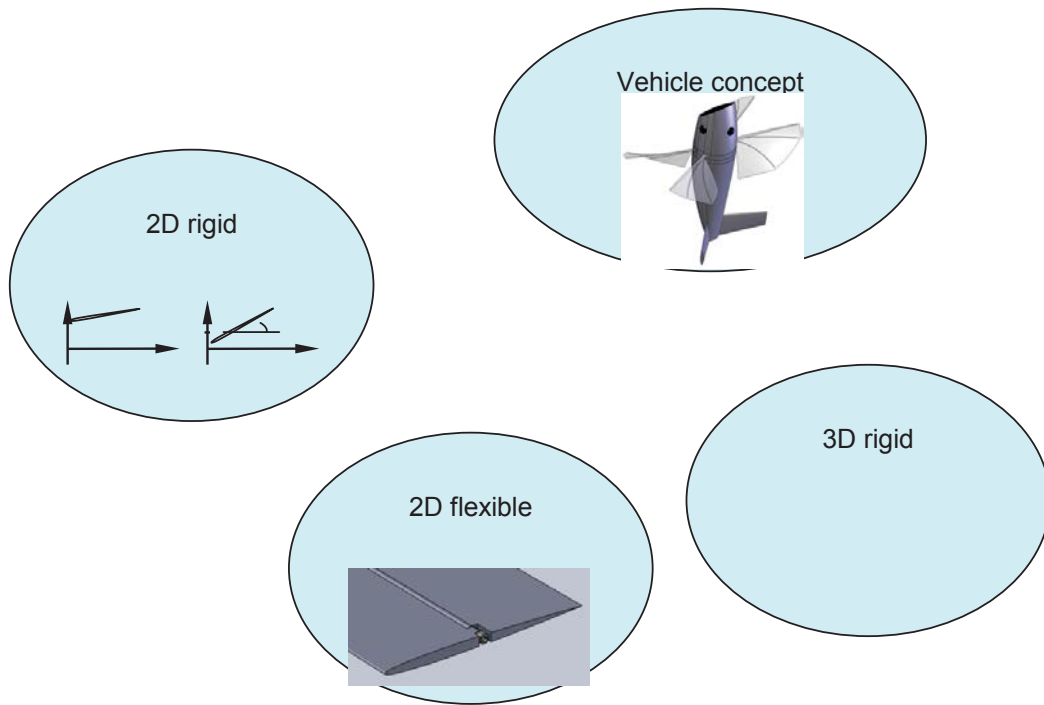


Figure 1: From a vehicle concept to simpler test cases

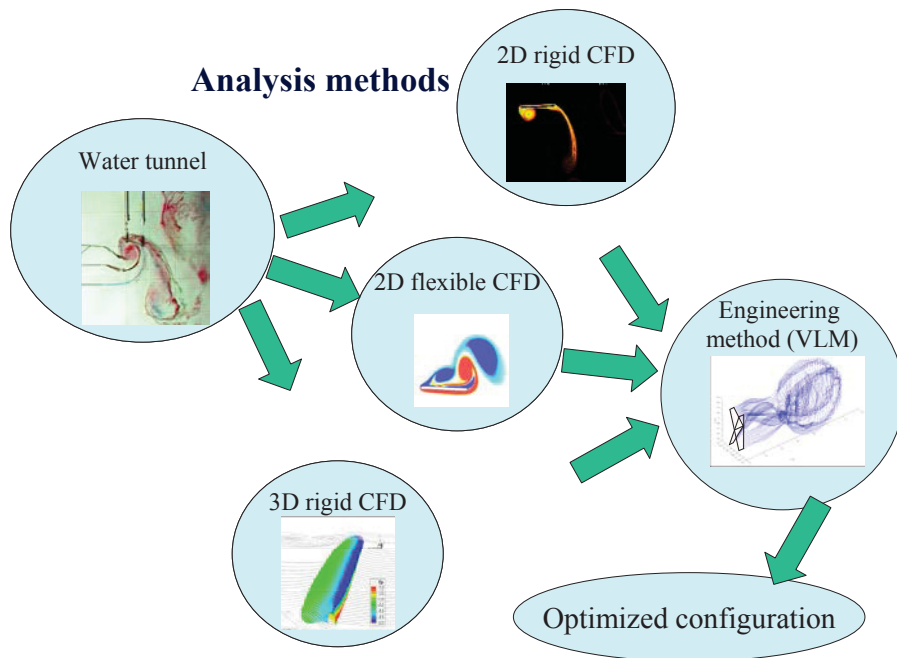


Figure 2: Analysis methods from water tunnel to optimized configurations

2 Notional nano-air vehicle defined

2.1 Concept definition

In order to guide NAV development and to illustrate potential military uses for a nano air vehicle, candidate missions were identified:

- High speed ingress, hover at target, and return
- Outdoor urban perch and stare
- Indoor autonomous or assisted navigation of low speed and/or hovering flight
- Outdoor hover outside a window

These missions are not addressed by existing assets. A study [31] identified the approximate flight performance requirements necessary to conduct such missions and the characteristics of some existing small flight vehicles. In order to achieve these missions, desirable NAV characteristics were investigated. The following characteristics were examined:

- Noise emission
- Perching and releasing
- Power requirements (hover and forward flight)
- Aerodynamic efficiency
- Hover efficiency (clap-fling phenomenon)
- Flapping wings compared to props and rotors
- Power sources (batteries, thermo electric generators, electromagnetic motors, ultrasonic motors, internal combustion, external combustion, fuel cells)
- Control actuator requirements and force generation
- Actuation methods (servos, shape memory alloys, piezoelectric actuators)
- Notional concepts and weight estimates

As a result of this analysis, a notional nano air vehicle was defined based on the mission requirements, expected progress in complementary technologies, and the experience of Advanced Subsonics in working on the Mentor micro air vehicle (MAV), the world's first hovering flapping wing vehicle which first flew in March 2002 [34]. The notional vehicle was defined in order for the project to focus on particular dimensions, motion characteristics and performance parameters.

Like the Mentor, the target NAV flaps its wings in a three dimensional manner. That is, the wing is finite and the wing tips move farther and faster than the root of the wing. Figure 3 illustrates the notional NAV. The system has the following geometrical characteristics:

- 4 wing "Double-Hummingbird" X-wing configuration developed for Mentor
- Capable of hover and fast translation flight
- Single degree of freedom root-flapping actuation
- Very thin flat wings

- Aeroelastic tailoring to passively give appropriate camber and span dependent twist

Table 1 lists a number of geometric properties of a reasonable NAV and Table 2 gives the mass breakdown for the vehicle.

The notional NAV will exploit the clap-fling phenomenon [31] in order to obtain improved thrust to power ratio (already verified to 40%) and very high thrust for limited disk area. The flapping mechanism will be by a single DOF actuation since the mechanism does not need to be overly complicated and therefore is light and robust.

A program goal for a Figure of Merit = 0.5 was set at this scale and disk loading (a 50% conversion efficiency to thrust power). This translates to a thrust to power of approximately 16 g/W for the wings only and an average of 0.6 W input at the wings to drive them.

The notional NAV control will be using the wings only. This should make the vehicle more manoeuvrable and less susceptible to changes in free stream velocity (descent or gusts). In order to keep the NAV within 20 cm of a prescribed path, the thrust needs to be altered only by 5% per wing, the control force must be achieved within about 0.1 to 0.2 seconds (8 to 16 flaps). This is because position is held by rotating the entire vehicle substantially to change the direction of the thrust vector to counteract the gust. Rapid rotation of the vehicle requires only a small differential change of the thrust generated by opposite wings. This is based on gusts of nearly double the induced velocity.

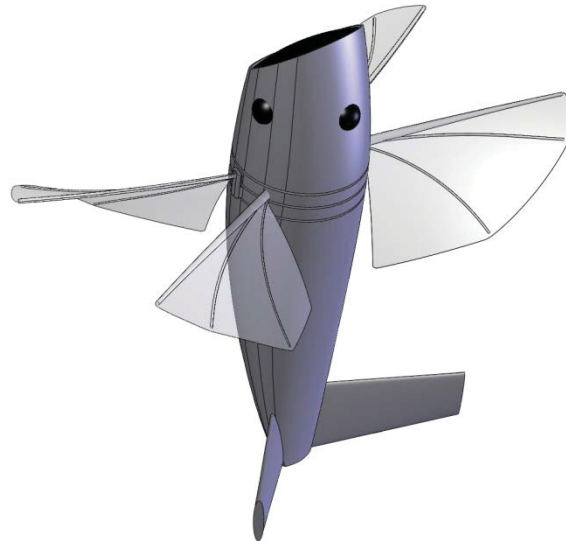


Figure 3: Representative NAV.

Table 1: Dimensions of representative NAV

mass (m)	10 g = 0.01 kg
weight (W) = thrust (T)	~0.1 N
span (b)	7.5 cm = 0.075 m
semi-span (b/2)	3.75 cm = 0.0375 m
body diameter	1.5 cm
airfoil chord at 58% of span (reference chord) (c_{ref})	0.019 m
frequency (f)	80 Hz (best estimate of req'd freq)
flap angle amplitude (Γ)	38 deg (= 0.66 rad)
peak to peak flap angle (2Γ)	76 deg (= 1.32 rad)
pitch amplitude (θ_0)	50 degrees (0.87 rad)
mean pitch (θ_1)	0 deg
phase shift (by which plunging leads pitching) (δ)	90 deg (1.57 rad)
freestream velocity (V_∞)	3 m/s
kinematic viscosity of fluid - air (ν)	1.51e-5 m ² /s
disk area (A)	= $\pi r^2 = \pi(0.0375\text{m})^2 = 0.00442\text{m}^2$
disk loading (T/A)	23.9 N/m ²

Table 2: Notional mass breakdown for the conceptual NAV

Component	Mass
Battery/Power Source	5g
Payload	2g
Onboard electronics for navigation and communications	0.5g
Complete vehicle structure	1g
Wing flapping actuator	1.5g

In the case of a hover, which is of particular interest, the vehicle's velocity (freestream velocity) is zero. Therefore for the hover case the "freestream velocity" is estimated as the velocity induced by the wings by using actuator disk theory (momentum theory) [31] and the values in Table 1:

$$V_{induced} = \sqrt{\frac{T}{2\rho A}} = \sqrt{\frac{0.1 \text{ N}}{2(1.225 \text{ kg/m}^3)(0.00442 \text{ m}^2)}} = 3.0 \text{ m/s} \quad (1)$$

Where the average induced velocity ($V_{induced}$) is a function of the thrust produced (T), the fluid density (ρ), and the disk area (A).

2.2 Flapping Kinematics

The flapping motion of a wing is rather complex and involves a combination motions in the different axes. Non-dimensional parameters such as Reynolds number or advance ratio are important in order to compare physical phenomena at different scales. For the notional NAV, it is assumed that wings undergo simple harmonic motion in angle. In other words, the angular flapping motion of the wing from the root and the angular pitching motion of the wing from the leading edge are simple harmonic motions. For this vehicle, the point about which the airfoil pitches will be the leading edge (LE). This is not unreasonable given the way Mentor's wings operated and is consistent with a passively twisted wing of the type envisioned for an eventual flight vehicle.

The angular displacement of the leading edge of the airfoil due to root flapping is defined as follows:

$$\gamma(t) = -\Gamma \sin(2\pi ft + \delta) \quad (2)$$

Where:

γ is the flap angle of the leading edge about which airfoil pitches

Γ is the amplitude (peak value) of the root flapping angle

f is the flapping frequency

t is the time

δ is the phase angle (the angle by which pitching lags flapping)

The pitching motion of the airfoil about the leading edge is described as:

$$\theta(t) = \theta_l + \theta_0 \sin(2\pi ft) \quad (3)$$

Where:

θ is the pitching displacement (angle) of the airfoil, positive counterclockwise

θ_l is the mean pitch position of the airfoil (for the test case this will be zero)

θ_0 is the rotational amplitude (peak value)

f is the flapping frequency

t is the time

These pitching and plunging motions are illustrated below in Figure 4. Plunging (h) is the translational motion due to flapping as viewed in a two-dimensional plane.

It was found during the Mentor program, as well as by numerous researchers, that a phase angle between pitching and plunging of around $\pi/2$ rad (90 deg) produces good results and this will be used as a starting point. Given that the phase angle is $\delta = \pi/2$ rad, at the initial condition ($t=0$) the airfoil is at zero degrees angle of attack.

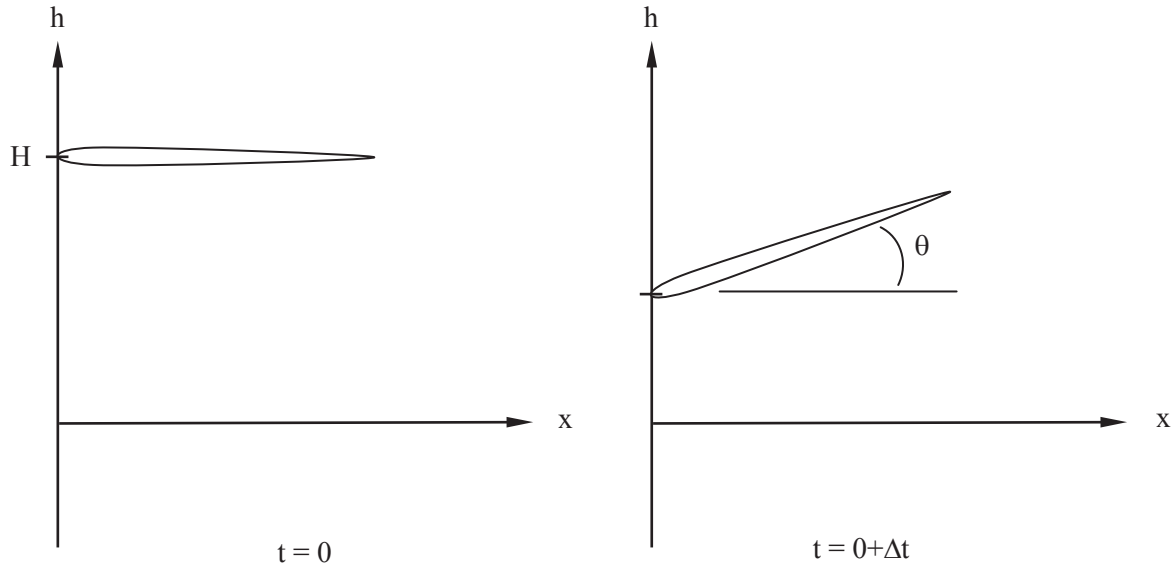


Figure 4: Description of airfoil flapping showing pitching and plunging

2.3 Dimensionless Parameters for NAV

Certain dimensionless parameters are required for the purposes of constructing test cases that are suitable for simulation and experimentation and are analogous to the conditions expected on an actual NAV. Three parameters are required for similarity and they are Reynolds number, reduced frequency, and flap amplitude to chord ratio.

2.3.1 Reynolds Number

In a fixed wing aircraft, definition of Reynolds number is straightforward as the wings are stationary with respect to the body-fixed frame of reference and the velocity term in the calculation is simply the freestream velocity (vehicle velocity). Now consider a flapping-wing vehicle in which the wing velocity may be a significant portion of the vehicle's overall velocity. In this case, the reference velocity is not obvious. Consider also a hovering flapping-wing vehicle. In this case, would the wing's velocity be used, or would one use the velocity of the jet induced by the flapping wings or some combination of these? For these reasons, three alternate formulations of Reynolds number that rely on the wing's speed rather than the vehicle's have been developed. In the first case frequency appears explicitly and in the second, the RMS value of wing speed is used.

2.3.1.1 Reynolds number based on frequency

The Reynolds number can be based on the maximum value of wing flap velocity ($V_{yMax} = 2\pi fH$). H is the flap amplitude defined as the semi-arc length covered by the flapping motion.

$$\text{Re}_f = \frac{2\pi H f c}{\nu} \quad (4)$$

2.3.1.2 Reynolds number based on RMS wing speed

An alternate formulation uses the RMS value of wing velocity and is defined here. Consider the usual form for Reynolds number:

$$\text{Re} = \frac{Vc}{\nu} \quad (5)$$

Let us define the characteristic velocity as the RMS value of the wing's velocity:

$$V_{RMS} = \frac{V_{yMax}}{\sqrt{2}} = \frac{(2\pi fH)}{\sqrt{2}} \quad (6)$$

This results in a definition of Reynolds number based on RMS velocity:

$$\text{Re}_{RMS} = \frac{Vc}{\nu} = \frac{(2\pi fH)c}{\sqrt{2}\nu} \quad (7)$$

2.3.1.3 Reynolds number based on combined freestream and plunging-induced velocity

Here the representative velocity is defined as the vector sum of the freestream velocity and the maximum plunging-induced velocity (V_{yMax}). This reference velocity could also be used in the calculation of other dimensionless parameters such as nondimensional pitch rate, reduced frequency, Strouhal number, advance ratio.

$$V_{ref} = ||V_{\infty} + V_{yMax}|| \quad (8)$$

The generalized Reynolds number is:

$$\text{Re}_{generalized} = \rho ||V_{\infty} + V_{yMax}|| c / \mu \quad (9)$$

2.3.1.4 Reynolds Number for notional NAV

The notional NAV has wings that flap about an axis at the root of the wing. Therefore, the tip moves more and faster than portions of the wing that are closer to the root. In either of the definitions of Reynolds number discussed earlier, the value depends on the flapping amplitude (which in three dimensions may also vary with spanwise location). For this example, the location 58% from the root is chosen as representative of the working section of the wing. The semispan of the notional vehicle is 3.75 cm. Using the formula for arc length, the flapping amplitude at the 58% span location is given as:

$$H \approx \frac{S}{2} = \frac{r2\Gamma}{2} = \frac{(0.0375\text{m} * 0.58) \left(\frac{76\text{deg} \pi \text{ rad}}{180 \text{ deg}} \right)}{2} = 0.01425\text{m} \quad (10)$$

The flapping frequency is $f = 80\text{Hz}$ and the chord length is $c = 0.019\text{m}$.

The maximum value of wing flap velocity is therefore $V_{peak} = 7.2 \text{ m/s}$

Using the Reynolds number definition based on frequency this gives a Reynolds number for the NAV of:

$$\text{Re}_f = \frac{2\pi H f c}{\nu} = \frac{2\pi(0.01425\text{m})(80\text{Hz})(0.019\text{m})}{1.51e-5\text{m}^2/\text{s}} = 9012 \approx 9000 \quad (11)$$

Based on the RMS definition, it is:

$$\text{Re}_{\text{RMS}} = 9012 / \sqrt{2} = 6372 \quad (12)$$

And, the generalized Reynolds number is based on the combined freestream (induced) and plunging-induced velocity:

$$V_{ref} = \sqrt{(3\text{ m/s})^2 + (7.2\text{ m/s})^2} = 7.8\text{ m/s} \quad (13)$$

$$\text{Re}_{\text{generalized}} = 9763 \quad (14)$$

The Reynolds number will be different for a different span location. It is of interest to the program to consider another span location : 77%. Using the formula for arc length, the flapping amplitude at the 77% span location is given as:

$$H \approx \frac{S}{2} = \frac{r2\Gamma}{2} = \frac{(0.0375\text{m} * 0.77) \left(\frac{76\text{deg} \pi \text{ rad}}{180 \text{ deg}} \right)}{2} = 0.019\text{m} \quad (15)$$

The flapping frequency is $f = 80\text{Hz}$ and the chord length is $c = 0.019\text{m}$. Using the Reynolds number definition based on frequency this gives a Reynolds number for the NAV of:

$$\text{Re}_f = \frac{2\pi H f c}{\nu} = \frac{2\pi(0.019\text{m})(80\text{Hz})(0.019\text{m})}{1.51e-5\text{m}^2/\text{s}} = 12017 \quad (16)$$

The generalized Reynolds number is: 12595

2.3.2 Reduced Frequency

The reduced frequency (k), is functionally equivalent to Strouhal number and is commonly defined as follows:

$$k = \frac{\omega c}{2V_{\infty}} = \frac{(2\pi f)c}{2V_{\infty}} = \frac{\pi f c}{V_{\infty}} \quad (17)$$

where ω is the circular frequency, c is the chord, f is the frequency in Hz and V_{∞} is the freestream velocity. Using the induced velocity for freestream velocity, the reduced frequency for the NAV is:

$$k = \frac{\pi f c}{V_{\infty}} = \frac{\pi(80 \text{ Hz})(0.019 \text{ m})}{3 \text{ m/s}} = 1.6 \quad (18)$$

2.3.3 Flap Amplitude to Chord Ratio

The flap amplitude to chord ratio varies with the span location. To effectively capture in 2D what is happening in 3D, the flapping amplitude to chord ratio of the NAV wing at 58% of span was considered. At this location the flap amplitude to chord ratio is $H/c = 0.01425 \text{ m} / 0.019 \text{ m} = 0.75$. This geometric parameter will be matched in the 2D test cases.

The value of this ratio at 77% of span as measured from the root is also of interest as it is used for the 3D test cases. At this location the flap amplitude to chord ratio is $H/c = 1.0$.

3 2D standard test cases

Standard test cases for both water tunnel experiments and CFD simulation were defined based on the notional nano air vehicle. From the characteristics of the notional vehicle, a first test case was defined representing a two-dimensional “cut” of the wing at 58% of the span from the root. The fluid in this case is air. A second test case was constructed to be functionally similar, but with properties well suited to the existing water tunnel facility and test rig as well as the existing CFD codes and meshing methods. The fluid in this case is water.

3.1 Rigid airfoil in air

A representative 2D flapping test-case was developed to suit the CFD component of research based on the representative NAV which, of course, undergoes 3D flapping. Therefore, a representative 2D case is formulated based on 3D wing kinematics, by choosing a representative section at 58% of span as measured from the root. This spanwise location was purposely chosen to result in a H/c ratio of 0.75 which is the maximum value the water tunnel test rig can produce. From this, the additional parameters listed in Table 3 are calculated.

Table 3: Calculated parameters of representative NAV

Radius at 58% span (r)	$r = 0.58 * b / 2 = 0.02175 \text{ m}$
Arc length of path at 58% span (S)	$S = r\Gamma = 0.02175 \text{ m} * 1.31 \text{ rad} = 0.02847 \text{ m}$
Plunge amplitude at 58% of span (H)	$H = S/2 = 0.01424 \text{ m}$
Amplitude to chord ratio (H/c)	$H/c = 0.75$

For this test case, the flapping motion is two-dimensional. That is, a wing of infinite span (or simply an airfoil) undergoing only pitching and plunging. The position of the airfoil at any time is given by the linear superposition of the motion due to plunging and that due to pitching. These motions are periodic and differentiable functions. The position due to plunging is given by:

$$y(t) = H \sin(2\pi ft + \delta) \quad (19)$$

Where:

- y is the linear plunge displacement of the point about which airfoil pitches (leading edge - LE)
- H is the amplitude (peak value) of the point about which the airfoil pitches
- f is the flapping frequency
- t is the time
- δ is the phase angle (the angle by which pitching lags plunging)

The airfoil's rotational position due to pitching is given by:

$$\theta(t) = (\theta_1 + \theta_0 \sin(2\pi ft)) \quad (20)$$

Where:

θ is the rotational displacement (angle) of the airfoil

θ_l is the mean rotational position of the airfoil (for the test case this will be zero)

θ_0 is the rotational amplitude (peak value)

f is the flapping frequency

t is the time

The velocity of the wing is given by the time derivatives of position:

$$\frac{dy}{dt} = V_{plunge} = 2\pi f H \cos(2\pi f t + \delta) \quad (21)$$

$$\frac{d\theta}{dt} = \omega = 2\pi f \theta_0 \cos(2\pi f t) \quad (22)$$

The test case is defined by the parameters of Table 4 which match the notional vehicle.

The airfoil should be as thin as possible to best approximate an actual NAV wing of the type used on the Mentor vehicle. Two different airfoils are considered: a symmetrical NACA 0005 airfoil section and a flat plate with a 5% thickness.

The three non-dimensional parameters for similarity are matched with the notional NAV at 58% of the chord:

- $k = 1.59$ (23)

- $h = H/c = 0.75$ (24)

- $Re_{generalized} = 9763$ (25)

3.2 Rigid airfoil in water

The dimensionless parameters for the notional vehicle developed previously are matched as much as possible to produce a case suitable for the IAR's water tunnel facility (Section 5.1).

The maximum pitch angle that can be developed in the water tunnel, θ_0 , is 30 degrees from the axis of the freestream velocity and is therefore used. The maximum plunge amplitude for a reasonable size wing was found to be $H = 1.88$ in (4.77 cm) for an airfoil chord of 2.5 in (6.35 cm). This gives the required value of H/c (at 58% of notional vehicle span).

$$\frac{H}{c} = \frac{1.88in}{2.5in} = 0.75 \quad (26)$$

To calculate flapping frequency, the reduced frequency is matched and the lowest possible freestream velocity is used (0.064 m/s) :

$$k = \frac{\pi f c}{V_{\infty}} = 1.6 \quad (27)$$

$$\Rightarrow f = \frac{kV_{\infty}}{\pi c} = \frac{(1.6)(0.064 \text{ m/s})}{\pi(0.064 \text{ m})} = 0.51 \text{ Hz} \approx 0.5 \text{ Hz} \quad (28)$$

Checking the Reynolds number shows that this parameter can be matched almost exactly with the constraints of the flapping rig and water tunnel.

The Reynolds number based on frequency is:

$$\text{Re}_f = \frac{2\pi H f c}{\nu} = \frac{2\pi(0.048 \text{ m})(0.5 \text{ Hz})(0.064 \text{ m})}{1.004 \text{ e-}6 \text{ m}^2/\text{s}} = 9488 \quad (29)$$

The generalized Reynolds number is:

$$\text{Re}_{\text{generalized}} = \rho ||V_{\infty} + V_{\text{induced}}|| c / \mu = 10\,500 \quad (30)$$

Again, the airfoil should be as thin as possible to best approximate an actual NAV wing of the type used on the Mentor vehicle. Two different airfoils are considered: a symmetrical NACA 0005 airfoil section and a flat plate with a 2.5% thickness (square leading and trailing edges).

Table 4: Parameters for 2D test cases in air and in water

Variable	Symbol	Value in air	Value in water
Frequency	f	80 Hz	0.5 Hz
plunge amplitude	H	0.01425 m	0.048 m (1.88 in)
twist amplitude	θ_0	50 deg (0.87 rad)	30 deg (0.524 rad)
mean twist	θ_1	0 deg	0 deg
phase shift (by which plunging leads pitching)	δ	90 deg	90 deg
airfoil chord	c	0.019 m	0.064m (2.5in)
airfoil max thickness	d	0.00038 m (0.38mm) 2% thickness	NACA 0005 + 2.5% flat plate (square leading edge)
freestream velocity	V_{∞}	3 m/s	0.064 m/s (2.5 in/s)
kinematic viscosity	ν	1.51e-5 m ² /s	1.004 e-6 m ² /s
Reynolds number	$\text{Re}_{\text{generalized}}$	9800	10 500

This complex flapping motion will cause a deviation in the local angle of attack from the steady case. The plunging motion combined with the pitch oscillation about the pivot point (leading edge) generates an instantaneous angle of attack (α). The instantaneous angle of attack at the leading edge is plotted in Figure 5 with the values of H, f, and θ . To help readers compare with the predictions of thin airfoil theory or panel methods, the effective angle of attack as defined by the three-quarter chord is also plotted in Figure 5. For some panel methods, the three-quarter chord angle of attack is a simple and intuitive trigger of submodels, such as a leading-edge separation model and a trailing-edge separation model.

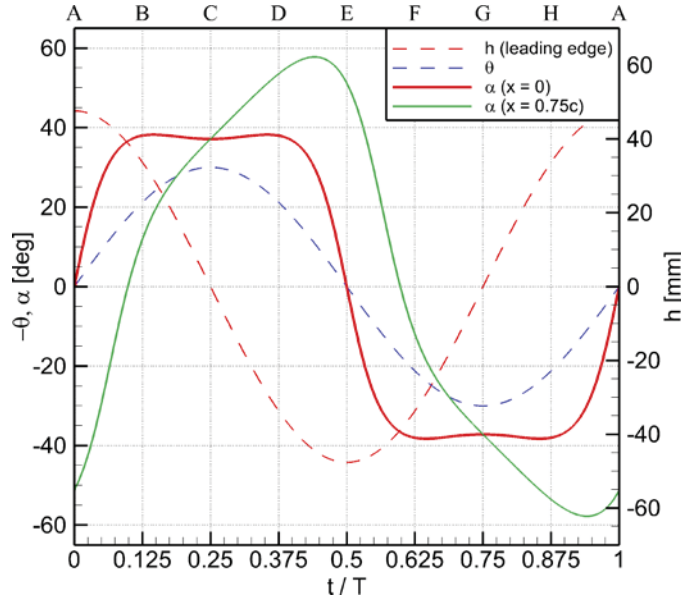


Figure 5: Time history of the effective angle of attack in accordance with the pitching-plunging motion of the airfoil. The letters at top correspond to the letters appearing in Figure 20 and Figure 21

3.3 Rigid airfoil in water with reflection planes

It is well known that there is a beneficial interference between wings operating in close proximity to one another at extremes of stroke (clap-fling effect). The notional vehicle attempts to take advantage of this effect. In order to better understand this phenomenon, a two dimensional test case with similarity to this situation was designed.

For the notional vehicle, at its extreme position the trailing edge gets very close to the trailing edge of the wing adjacent to it. Since the two adjacent wings do the mirror image of one another, a reflection plane located at mid-position between the two wings would produce a similar effect.

This idea is used to design a two-dimensional test case with attributes of the clap-fling effect. Two reflection planes, one for the upstroke and one for the downstroke, were therefore used to simulate the clap-fling effect with the rigid 2D airfoil.

With the airfoil dimension and motion defined previously for the water tunnel test, the lowest position of the trailing edge is 0.0579 m from the central position (Figure 6) or 0.912c. Four reflection plane positions giving various gaps between the trailing edge and the reflection plane were defined. These reflection plane positions (from the central position) are:

$$1.03c = 0.912c + 0.12c \text{ (gap)}$$

$$1.15c = 0.912c + 0.238c \text{ (gap)}$$

$$1.30c = 0.912c + 0.388c \text{ (gap)}$$

$$1.45c = 0.912c + 0.538c \text{ (gap)}$$

Note that there should be no boundary layer on the reflection plane or this one should be minimized.

All parameters defining the motion and the airfoil geometry are identical to those of the 2D rigid airfoil in water.

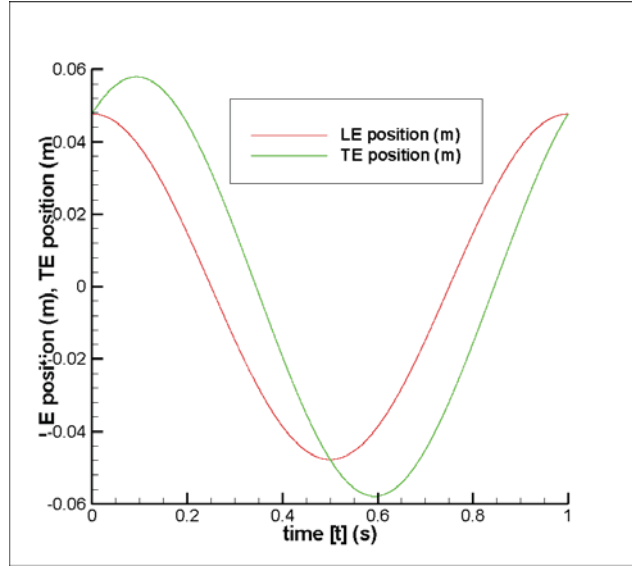


Figure 6: Leading and trailing edge position for 2D test in water

3.4 Flexible airfoil with single torsion joint in water

A simple configuration of a flexible airfoil was defined and used for this test case. Chord-wise flexibility can be represented by continuous flexibility along the chord or by a finite number of torsion joints connecting rigid sections. For this case, the flexible airfoil is represented by its simplest form: two rigid sections connected a single torsion joint. This torsion joint is located at mid-chord.

A NACA0005 cross-section is used. The chord is 6.35 cm as for the rigid airfoil in water. The same motion values as for the 2D rigid airfoil in water (frequency, plunge amplitude, twist amplitude, phase shift and freestream velocity) are used. The stiffness of the torsion spring is the added parameter for this test and several values can be used by changing the spring. Also, the twist amplitude of 30 degrees will be varied considering that the airfoil flexibility provides passively a similar effect.

3.5 Flexible cambered airfoil in water

As a result of an optimization exercise with the Vortex Lattice Method (see Chapters 8 and 9), an airfoil with a camber varying with the flapping cycle was defined and later used in the VLM and CFD analysis.

The airfoil's camber line is given by:

$$y = x^\lambda \quad (31)$$

The camber exponent is described by:

$$\lambda = \Lambda \sin(2\pi(2f)t + \delta_{camber}) + (\lambda_{mean}) \quad (32)$$

The parameters optimized for a test case in air [10] were adopted for the pitch-plunge plate in water:

$$\Lambda = 1.5, \lambda_{mean} = 2.5, \delta_{camber} = 270^\circ$$

The length of the curve was rescaled such that the curved chord length was equal to $c = 0.064$ m.

Then, the airfoil was rotated so that the TE lies on the original uncambered chord line. This decoupled camber from pitching.

Finally the sign of the function that described the camber line was taken from the sign of the following function:

$$f(t) = \sin\left(2\pi f t + \frac{\delta_{camber}}{2} + \frac{\pi/2}{2}\right) \quad (33)$$

All the other parameters describing the motion are identical to that of the 2D rigid airfoil in water.

4 3D standard test cases

4.1 Wing geometry

Note that like Mentor and birds, the notional NAV is also a root-flapper. That is, the wing is flapped through an angle at the root causing the wing tips to move farther and faster than the root of the wing. In this way the 3D case differs from the standard 2D AeroNAV test cases.

This 3D test case mimics as closely as possible the notional NAV while adhering to the constraints of the NRC 3D water tunnel test rig. Figure 7 shows the wing planform, tip chord and flapping axis. Figure 8 shows the wing in the water tunnel. The wing is shown with its maximum pitch amplitude and flap amplitude, though in the test case these do not occur simultaneously. Note that the wing is placed relatively centrally in the tunnel cross-section and the wing does not come closer than 70mm the tunnel wall in this conservative placement of the wing where flap and pitch angles are at their maxima.

Repeatability is of primary importance for the experimental work. Therefore, a rigid wing is specified for the 3D water tunnel rig even though actual NAV wings would be flexible and would twist in response to the aerodynamic and inertial loads that they experience. The span dependent twist of the NAV wing will be approximated by pitching the entire wing on the water tunnel rig about its leading edge.

Another difference between the notional NAV and this water-tunnel case is the length of the wing extension which goes from the wing root to the flapping axis. A relatively long wing root extension is needed between the strain gauge balance and the wing. This root extension is a rod of circular cross section with diameter suitable for the rig. For simplicity, this rod is eliminated entirely in the test case description (and in the CFD computations) and only the wing is modeled with its flapping axis.

The airfoil should be as thin as possible to best approximate an actual NAV wing of the type used on the Mentor vehicle. Two different airfoils are considered: a symmetrical NACA 0005 airfoil section and a flat plate with a 5% thickness.

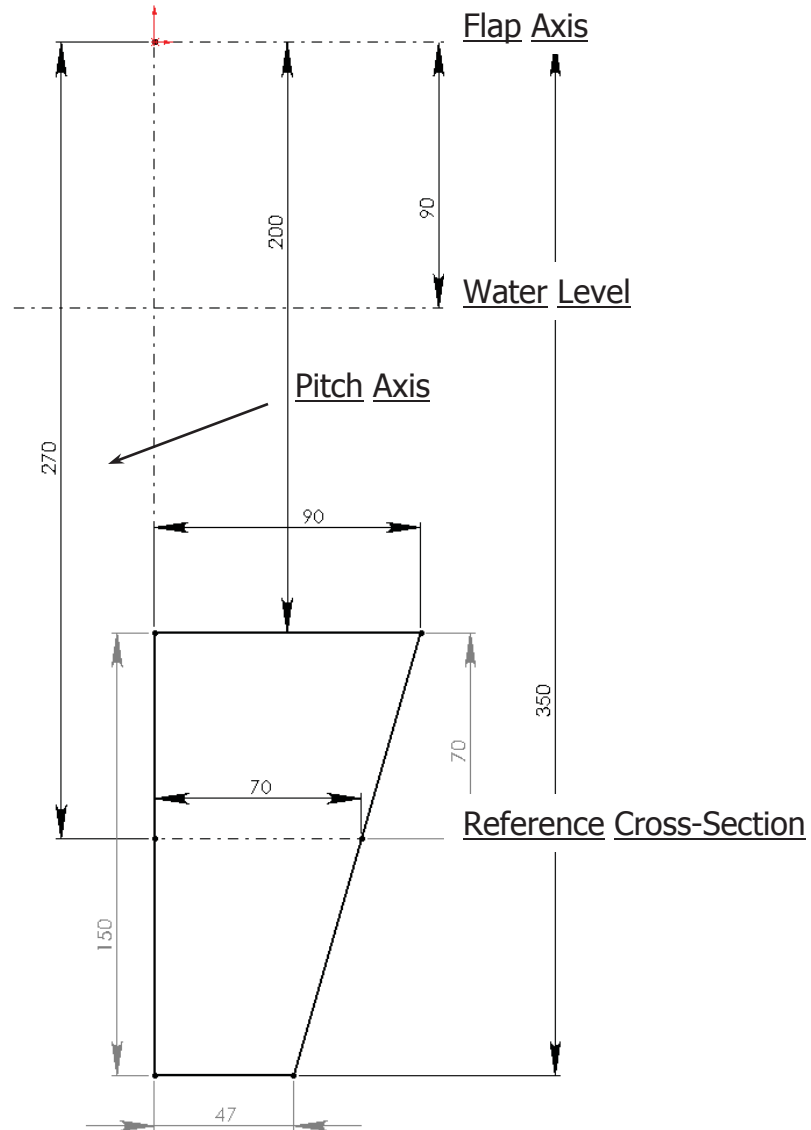


Figure 7: A scale schematic showing 3D wing planform including flap axis, water level, root chord, tip chord and span. All dimensions are in mm. Redundant dimensions are shown in grey.

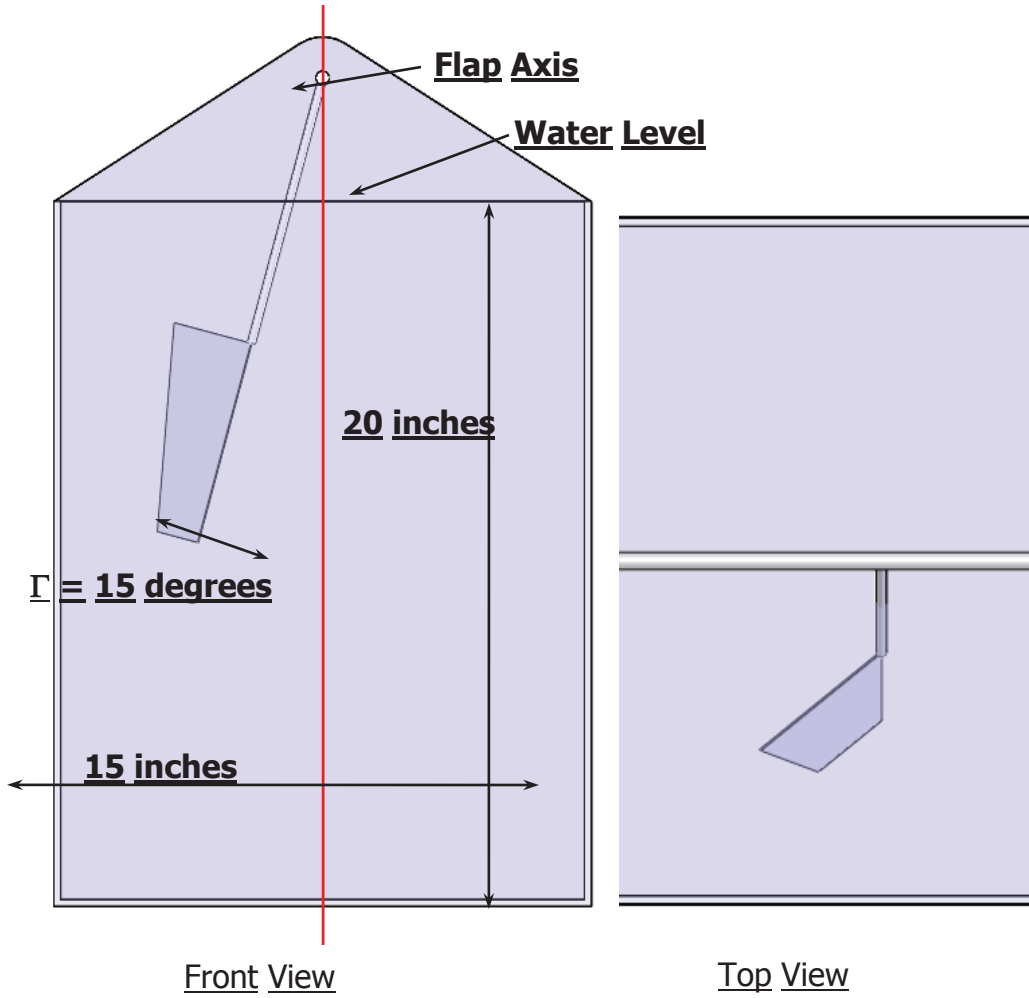


Figure 8: Scale drawings showing the 3D test case geometry in the water tunnel

4.2 Flapping Kinematics

The 3D motion of the wing is defined below. The angular displacement of the leading edge of the airfoil due to root flapping is defined as follows:

$$\gamma(t) = -\Gamma \sin(2\pi ft + \delta) \quad (34)$$

Where:

γ is the flap angle of the leading edge about which airfoil pitches

Γ is the amplitude (peak value) of the root flapping angle

f is the flapping frequency

t is the time

δ is the phase angle (the angle by which pitching lags flapping)

The pitching motion of the airfoil about the leading edge (Figure 7) is described as:

$$\theta(t) = \theta_1 + \theta_0 \sin(2\pi ft) \quad (35)$$

Where:

θ is the pitching displacement (angle) of the airfoil

θ_1 is the mean pitch position of the airfoil (for the test case this will be zero)

θ_0 is the rotational amplitude (peak value)

f is the flapping frequency

t is the time

The test case is defined by the parameters of Table 5.

Table 5: Parameters for 3D test case in water

Variable	Symbol	Actual Size NAV	3D Water Test Case
frequency	f	80 Hz	0.46 Hz
flap angle amplitude	Γ	38 degrees (0.66 rad)	15 degrees (0.26 rad)
pitch amplitude	θ_0	50 degrees (0.87 rad)	40 degrees (0.70 rad)
mean pitch	θ_1	0 deg	0 deg
phase shift (by which plunging leads pitching)	δ	90 deg (1.57 rad)	90 deg (1.57 rad)
airfoil chord at 77% of span (reference chord)	c_{ref}	~0.019 m	0.07 m
root chord	c_{root}		0.090m
tip chord	c_{tip}		0.047m
freestream velocity	V_∞	3 m/s	0.0635 m/s (2.5 in/s)
kinematic viscosity of fluid	ν	1.51e-5 m ² /s	1.004 e-6 m ² /s
semi span	$b/2$	0.0375 m	0.350m

4.3 Non-dimensional parameters

As before, three non-dimensional parameters will be matched as closely as possible to create a NAV-equivalent test case in water. These parameters are Reynolds number, reduced frequency, and flap amplitude to chord (H/c) ratio. For this test case, it is appropriate to calculate these parameters at the section located at 77% of the span (270 mm / 350 mm; Figure 7).

The resulting wing for the 3D water tunnel test case is approximately 3.5 times as large as an actual NAV wing.

$$H \approx \frac{S}{2} = \frac{r2\Gamma}{2} = \frac{(0.270) \left(\frac{30 \text{ deg } \pi \text{ rad}}{180 \text{ deg}} \right)}{2} = 0.070 \text{ m} \quad (36)$$

$$\frac{H}{c} = \frac{70 \text{ mm}}{70 \text{ mm}} = 1.0, \text{ which matches the notional vehicle value at 77\%.} \quad (37)$$

To calculate flapping frequency, the reduced frequency is matched and the lowest possible freestream velocity is used:

$$k = \frac{\pi f c}{V_{\infty}} = 1.6 \quad (38)$$

$$\Rightarrow f = \frac{k V_{\infty}}{\pi c} = \frac{(1.6)(0.0635 \text{ m/s})}{\pi(0.07 \text{ m})} = 0.46 \text{ Hz} \quad (39)$$

The reference velocity becomes:

$$V_{ref} = \sqrt{V_{\infty}^2 + (2\pi H f)^2} = 0.212 \text{ m/s} \quad (40)$$

Checking the Reynolds number shows that this parameter cannot be matched exactly given the minimum speed of the water tunnel. The reference velocity is

$$\text{Re}_{generalized} = 14780 \quad (41)$$

Here, it was decided to match advance ratio and the plunge amplitude to chord ratio, and let the Reynolds number differ. That being so, the Reynolds number does not differ by a meaningful amount with the NAV $\text{Re}=12595$ and the test case $\text{Re}=14780$. Because large scale flow separation seems to be dominated by the kinematics and geometry in this case, letting Reynolds number differ slightly between the two cases was deemed the best compromise.

This page intentionally left blank.

5 2D and 3D water tunnel testing

The details of the 2D and 3D water tunnel testing can be found in [2] and [5].

5.1 Water Tunnel

The standard test cases were carried out experimentally in the Eidetics Flow Visualization Water Tunnel at the NRC-IAR (Figure 9). The water tunnel features an open-surface test section and a vertical return circuit. The nominal dimensions of the test section are 38 cm wide, 51 cm high, and 163 cm long. The maximum freestream velocity achievable in the test section is 305 cm/s; 20% of this range was required for the standard test cases. The freestream turbulence intensity in the test section is rated at less than 1%.



Figure 9: Eidetics Flow Visualization Water Tunnel at the NRC Institute of Aerospace Research.

Even so, dye flow visualization revealed that fluctuations in the test section increased after approximately 240 seconds of continuous operation of the facility. The increased fluctuations were attributed to remnants of the turbulent wake, which is developed by the large amplitude plunge motion of the 2D airfoil model but was not attenuated adequately by the return circuit or the flow conditioner elements in the delivery plenum. For this reason, the operation of the motion rigs and the measurement of load data were limited to 180 seconds for both the 2D and 3D test cases.

5.2 Setup for the Standard 2D Test Case

The experimental setup for the standard 2D test case is illustrated in Figure 10.



*Figure 10: Left: the 2-DOF motion rig;
Right: the two-dimensional airfoil model between two reflection planes*

Two rigid 2D airfoil models were designed and manufactured: one with a NACA 0005 cross-section; the other, a flat plate with a thickness equal the maximum thickness of the NACA 0005 airfoil. Both models featured a span of 25.4 cm and were fabricated from stainless steel to protect against corrosion and for stiffness, especially in the case of the NACA 0005 model which has a very thin trailing edge. Tall glass endplates were placed carefully at both tips of a model to mitigate tip effects and to encourage two-dimensional flow conditions over the airfoil; Reflection planes (appearing above and below the 2D airfoil model in Figure 10) were added later to simulate the clap-fling phenomena by mimicking multi-wing interaction but in a simplified way.

The motion of the airfoil model is controlled by a two degree-of-freedom system (2-DOF). The model is connected, at its spanwise center, to a pair of vertical plunge rods. Each plunge rod is driven by a linear shaft motor integrated with a slider system; a linear encoder conveys the position of the motor to the motion controller, closing the feedback loop. The linear motion of the plunge rods is programmed to provide the sinusoidal plunge and pitch motions at the frequencies and amplitudes prescribed by the test case.

Two uniaxial load cells, each with a rating of 44.5 N (10 lbs), sensed the lift force developed by the airfoil and acting on the plunge rods. Each load cell was mounted inline between a plunge rod and its drive mechanism. The estimated uncertainty in the total lift force measurement is 0.084 N (8.6 g). The natural frequency of a plunge rod and load cell combination is 147 Hz. Drag force was not measured because the desired approach to acquire this quantity was unsuccessful.

The output signals of the load cells and position encoders were sampled at rate of 1 kHz and acquired for 81 cycles of motion. Data were collected for both “wind” and “tare” conditions. The tare accounted for inertial loading and it was acquired with a test section emptied of water. The lift force signal was corrected for inertial effects by the tare on a sample-by-sample basis and converted to engineering units. The resulting lift force signal was adjusted once more to account for buoyancy, again, on a sample-by-sample basis; the buoyancy tare was an analytical model. After the first six motion cycles were discarded, to account for transient flow conditions at the start of a run, the lift force data was parsed to formulate a three-cycle ensemble-average.

Phase-locked particle imaging velocimetry (PIV) measurements of two components of velocity, stream-wise and vertical, were performed for the 2D test case to identify features in the flow over the surface of the airfoil and in its wake. A LaVision PIV system was configured to receive a trigger signal from the motion control system; once triggered, images were acquired at intervals of 1/16-cycle to correspond with CFD results. The streamwise measurement plane was aligned with the quarter-span of the airfoil model; the laser illuminated the plane from beneath the test section. The PIV recording parameters are listed in Table 6.

Table 6: PIV recording parameters for the 2D test case.

Flow geometry	64 mm/s, parallel to the light sheet
Field of view	228 mm x 171 mm (W x H)
Recording method	15 Hz double frame/single exposure
Recording medium	2-megapixel, full frame CCD (1648 x 1214 pixels)
Recording lens	f = 50 mm, f-stop = 1.4
Illumination	Nd:YAG laser, 50 mJ/pulse, 50 Hz pulse rate
Illumination optics	Light-sheet lens, 10° divergence
Pulse delay	t = 10 ms
Seeding material	hollow glass spheres, 10 μ m nominal diameter

5.3 2D flexible wing model

A NACA0005 cross-section was used. The chord is 6.35 cm as for the rigid airfoil in water. The stiffness of the torsion spring is the added parameter for this model and several values can be used by changing the spring. A potentiometer is incorporated for measuring angular displacement of the trailing-edge segment. The attached photographs (Figure 11) depict the calibration setup and the flexible wing installed in the test section.

The water tunnel tests were never done for this model because the project ended before the system became operational.

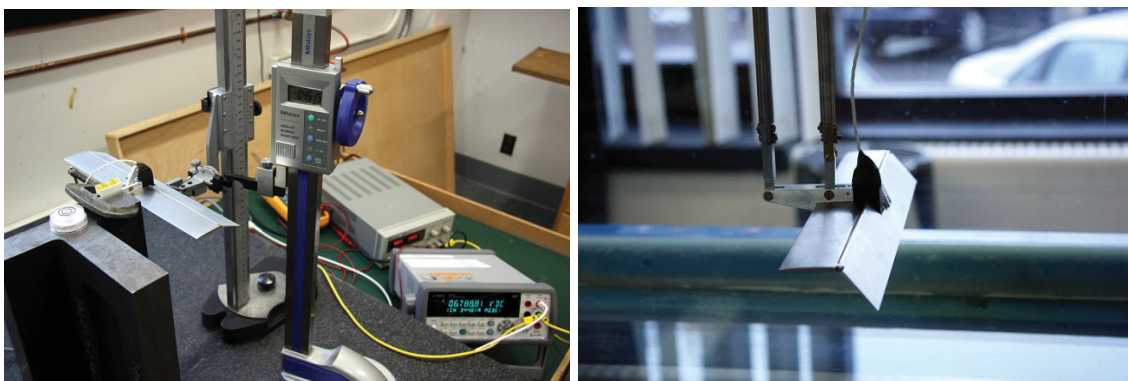


Figure 11: Calibration setup and the flexible wing in test section

5.4 Setup for the Standard 3D Test Case

The experimental setup for the standard 3D test case is illustrated in Figure 12 and Figure 13.

Similar to the 2D airfoil models, two rigid 3D wing models were manufactured with a NACA 0005 and a flat plate cross-section. The models were fabricated from aluminum for lightness and shared an interchangeable supporting arm, which connected the wing model to the balance. The center of the cross-section of the supporting arm coincides with the leading edge of the wing model so that the pitching motion rotates the wing about the leading edge.

The sinusoidal motion prescribed for the wing model was controlled by a three degree-of-freedom (3-DOF) motion system that is capable of providing flapping, pitching, and sweeping motions directly. The sweeping motion was not activated for this work. Each motion was driven by a brushless DC servomotor equipped with a gear reduction box. An angular position encoder, integrated with the servomotor, closed the feedback loop for the motion control system.

A bi-fold five-component balance (Figure 14) was mounted between the wing and the motion system, inline with the leading edge of the wing. The balance measured the normal and axial forces, and the pitching, rolling, and yawing moments in the body axes of the balance. The limit to which each component was calibrated, as well as the estimated measurement uncertainty and natural frequency are listed in Table 7.

Table 7: Balance characteristics

Balance Component	Calibration Limit	Uncertainty	Natural Frequency
Normal force	9.81 N	± 0.027 N (2.8 g)	165 Hz
Axial force	9.81 N	± 0.049 N (5.0 g)	165 Hz
Pitching moment	0.40 Nm	± 0.007 Nm	234 Hz
Yawing moment	1.82 Nm	± 0.017 Nm	350 Hz
Rolling moment	1.82 Nm	± 0.027 Nm	350 Hz

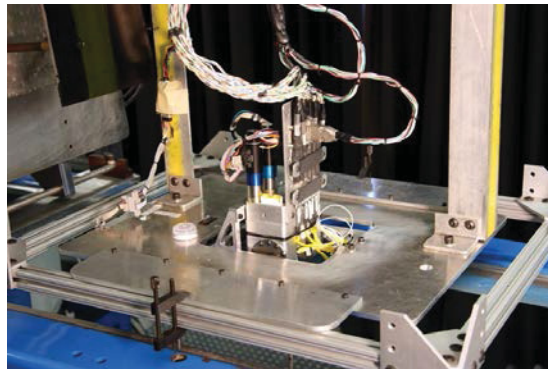


Figure 12: The 3-DOF motion rig

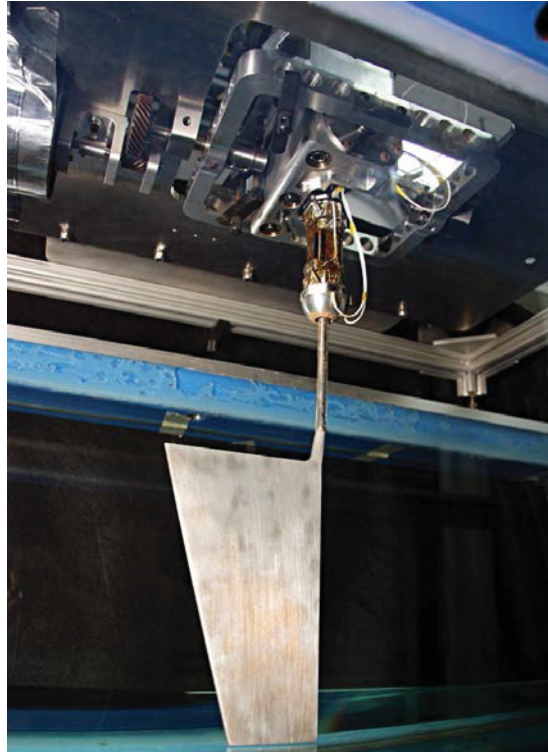


Figure 13: The three-dimensional wing model is installed in the balance.

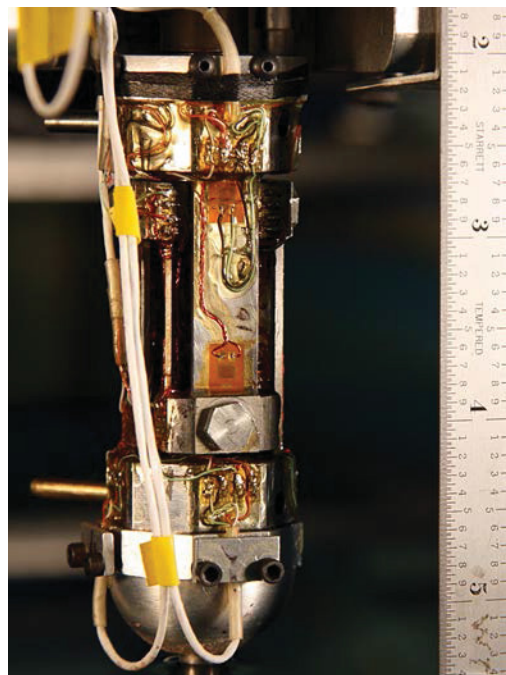


Figure 14: The bi-fold five-component balance used for the standard 3D test case

The acquisition and reduction of data, especially the adjustments for inertial and buoyancy effects in the force and moment data, followed the same procedures as for the standard 2D test case. All loading due to the supporting arm by itself was deemed negligible and was not considered in the data reduction process. The normal and axial forces were transformed into lift and drag forces in the test-section axes. The rolling

and yawing moments were transferred from the resolving center of the balance to, respectively, the flapping axis and the intersection of the flapping and pitching axes in the 3-DOF motion rig; the transfer of the pitching moment was not necessary. No PIV measurements were acquired for the 3D test cases.

6 CFD computations setup

6.1 INSflow computations

The details of the INSflow solver, the setup for the standard test cases, and results can be found in [3][5][6][8][9][11][13][20][21][23][26][27][29][30]. A brief summary is given in the sections below.

6.1.1 Flow solver

The computational-fluid-dynamics code, INSflow, was developed in-house at the NRC-Aerospace for solving three-dimensional unsteady incompressible flows. The code has been used for a number of applications including large-eddy and unsteady Reynolds-averaged Navier-Stokes simulations, low-Reynolds flows, and flapping-wing aerodynamics.

INSflow applies the integral form of the conservation laws of mass and momentum. A fully-implicit second-order temporal differencing scheme was implemented in the discretization, which made the algorithm stable for large timesteps. The discretization of the convective and diffusive fluxes was carried out in a co-located variable arrangement using a finite-volume approach that was second-order accurate in space.

A first-order upwind scheme is available. The coupling of the pressure and velocity was handled using a modified SIMPLE algorithm. The calculations were performed on moving grids; the velocity of the grid movement was included in the governing equations in an inertial frame of reference. In order to avoid artificial mass sources generated by the grid velocity, a space conservation law was introduced to ensure a fully conservative property in the computations.

6.1.2 Setup for the Standard 2D Test Case

The 2D calculations were performed on O-type meshes. The farfield boundaries were located about 25 chords away from the surface of the airfoil. The nominal mesh had 481 x 129 grid points. This mesh was designed with a grid density increasing towards the wall at a rate of 6% for the near-wall region and 8.7% for the outer region. The grid lines in the normal-to-the-wall direction were simple straight lines. Improved grid orthogonality would accelerate the calculation convergence and increase the simulation accuracy, but the modification was not investigated in this study. The calculations were started from a stationary fluid. In general, the third cycle produced comparable results to the second cycle for the cases reported in this study.

To select a suitable grid for the investigations, computations for the standard 2D test case were conducted using the second-order spatial discretization on three O-meshes: 241 x 97, 481 x 129, and 961 x 161, with corresponding timesteps for one plunging cycle of 2,888, 3,840, and 5,760, respectively. Six to eight flapping cycles were conducted for the grids. The discrepancies of the results obtained on the three grids were minimal. The aerodynamic coefficients matched well starting from the second cycle. Based on this observation, the results obtained from the medium grid are presented in Chapter 7.

6.1.3 Setup for the Standard 3D Test Case

A grid with $481 \times 129 \times 33$ nodes was used for the flow domain around the wing body, with a farfield boundary located at about 10 airfoil chords. This grid size is comparable to the medium grid used in the earlier 2D calculations, but with 33 stations located along the wing span. The computational domain contained two extensions. The first one stretched from the wing root to the flapping axis, while the second extended beyond the wing tip for 150 mm, which was equal to the spanwise dimension of the wing body. These two extended domains were discretized using grids with $481 \times 133 \times 33$ nodes, thus constituting a three-block structure. Compared with the grid around the wing body, there were 4 extra grid points in the direction normal-to-the-wing surface, to mesh the thickness of the wing root and tip surfaces.

6.2 Fluent

Unsteady simulations of the flow field were also made using the commercial CFD code Fluent (version 6.3). The implicit, incompressible, structured mesh solver was used in 2-D. The capability of Fluent to deform the grid by the use of user defined functions (UDF) was used.

Fluent includes many viscous models, from the simplest laminar model to LES passing by many two-equation models. In this study [28], we have compared the results obtained with the laminar, k- ω SST, DES with Spalart-Allmaras and LES viscous models. The quantitative comparison was done in terms of convergence speed and drag/propulsion force coefficient, and the qualitative comparison was done using contour plots of vorticity magnitude.

Two mesh motion techniques were studied to impose the airfoil motion to the grid. Both techniques used a completely structured grid with emphasis put on the region around the airfoil. The grid was organized in a way that the airfoil motion does not deform the grid in the surrounding area of the airfoil so the results do not vary from one cycle to another because of grid topography.

The first technique used a non-deforming area around the airfoil. This area had a diameter of 10 airfoil chords. The region surrounding the airfoil is showed in red in Figure 15. All the nodes in this area have the same pitching and heaving motion as the airfoil. To generate the motion, grid options “rigid body motion” and “non-conformal interface” were used in Fluent. To complete the airfoil motion, two other grid components were used. Figure 15 shows all mesh components. The green part is the heaving-only section, and the mesh motion is described only by an up and down motion of the grid with no pitching. Consequently, the “layering” grid motion type was used with the splitting and collapsing factors of 0.2 and 0.4 respectively. Layering is for applications involving linear motions. Layers of mesh are added or deleted at the boundary of the grid to satisfy the split and collapse conditions. The purple region is the non-moving part of the mesh.

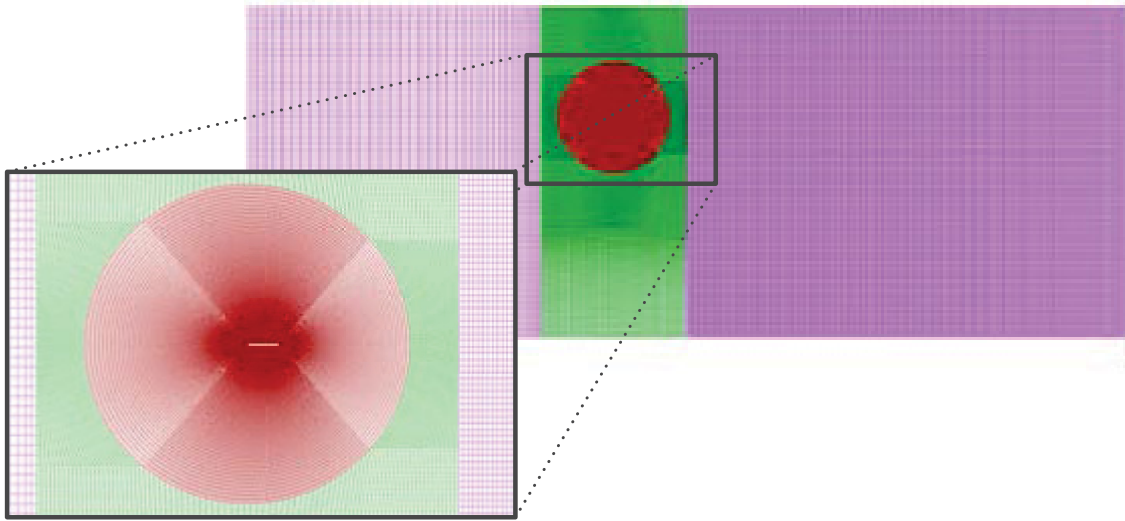


Figure 15: First moving mesh technique, in red the pitching & heaving zone (rigid body motion), in green the heaving zone (grid layering) and in purple the stationary part

The second technique used only one region. To simulate the airfoils' motion, a completely structured C-grid was generated (Figure 16). Again, the emphasis was put on the region around the airfoil. The grid, contained 830 000 cells and 1 000 nodes were placed on the unit length airfoil surface. The final scale was done in Fluent to the desired size. All nodes in the grid have the same pitching and heaving motion as the airfoil. The grid stays the same for all time steps and no node are added or subtracted. The motion was generated by the grid option "rigid body motion" of Fluent.

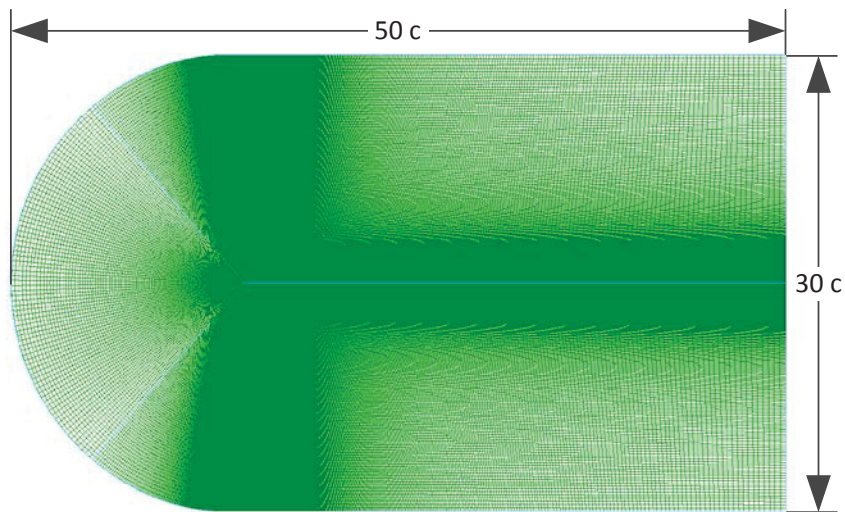


Figure 16: Second moving mesh technique, rigid body motion only

The application of Fluent for this kind of motion and this low Re was then verified [28] against test cases found in the open literature using the laminar viscous model. Instead of the standard wing and standard NAV flow conditions, a NACA 0012 airfoil profile was used in all validation test cases.

The first validation test case was a pure plunge for the free stream condition $Re = 20\,000$ and NACA 0012 airfoil. As seen on Figure 17, Fluent predicted well the position and size of the vortices shed by the airfoil. Another test case included the heaving and pitching motion of the NACA 00012. For this case, the Re was $40\,000$. The Fluent prediction agreed with the reference drag and lift coefficients generated by the airfoil motion are shown in the Figure 18.

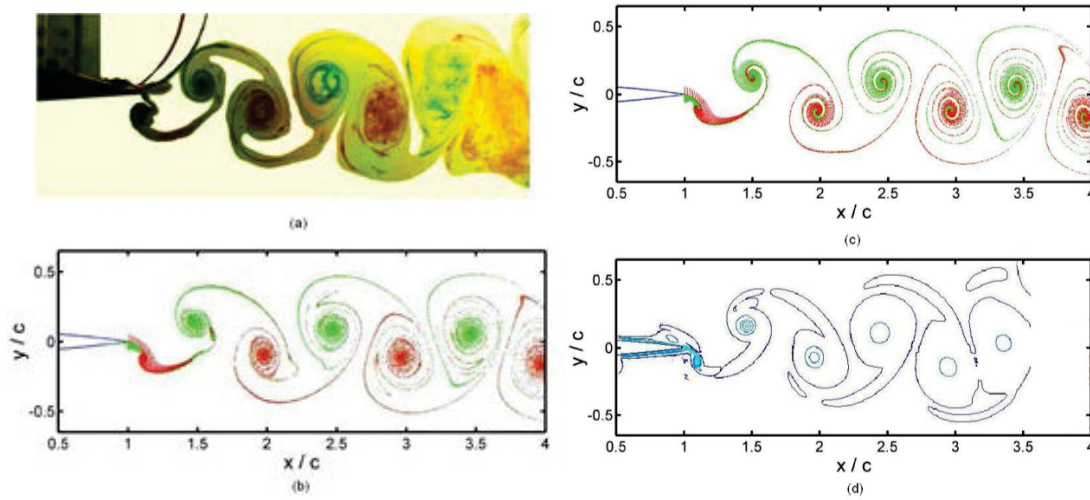


Figure 17: Vortices shed by the heaving NACA 0012 airfoil $Re=20\,000$, (a) experimental, (b) numerical laminar, (c) numerical turbulent and (d) Fluent laminar

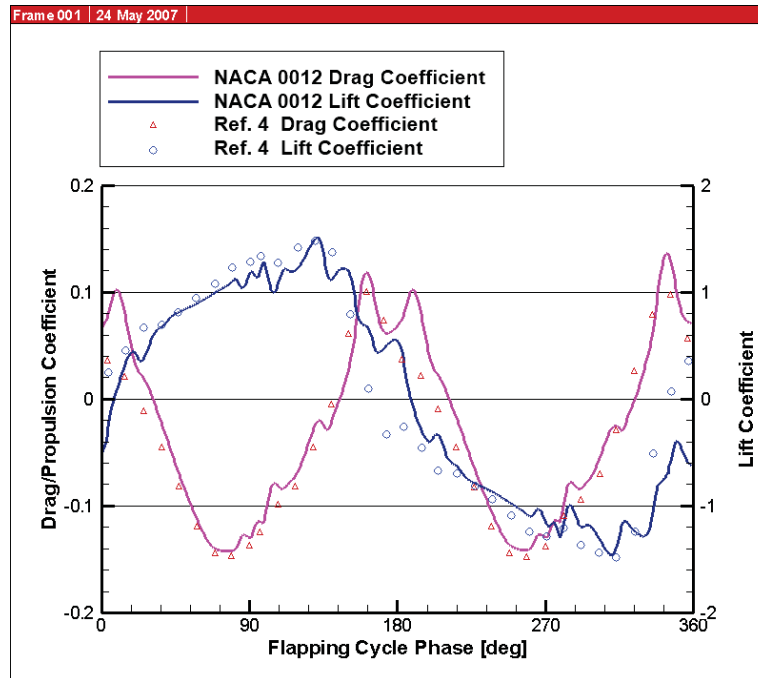


Figure 18: Lift and drag coefficient of the heaving and pitching NACA 0012 airfoil

7 Water tunnel and CFD results

Water tunnel and CFD results were published in many of the project documents. In particular, combined experimental and numerical results can be found in [2], [5] and [6].

7.1 Standard 2D Test Case

7.1.1 Drag and Lift Forces

Two cycles of lift measurements and lift predictions, produced by INSflow and Fluent, are superimposed in Figure 19 (right side). The experimental results are taken from an ensemble-average of 24 three-cycle time-series; the CFD results are two instantaneous cycles taken from a total of six computed cycles. The motion profiles synchronized the presentation of the two sets of results. Excellent agreement can be seen between the two CFD codes. Both codes predicted the same aerodynamic force amplitude and frequency. In general there is good agreement between the CFD and the experiment; for instance, there is repeatable behavior corresponding with the pitching-plunging motion schedule; the magnitudes of peak lift match well; and there are no indications of obvious or significant phase shift. For the most part, the computed lift force falls within the uncertainty band of the measured lift force. The CFD simulations reproduce successfully the sluggish development of lift force at the start of both the downstroke and the upstroke. Interestingly, the magnitude of the lift forces at the upstroke and the downstroke differ slightly; the difference could be indicative of an interaction between the airfoil and its asymmetric wake, which will be discussed later.

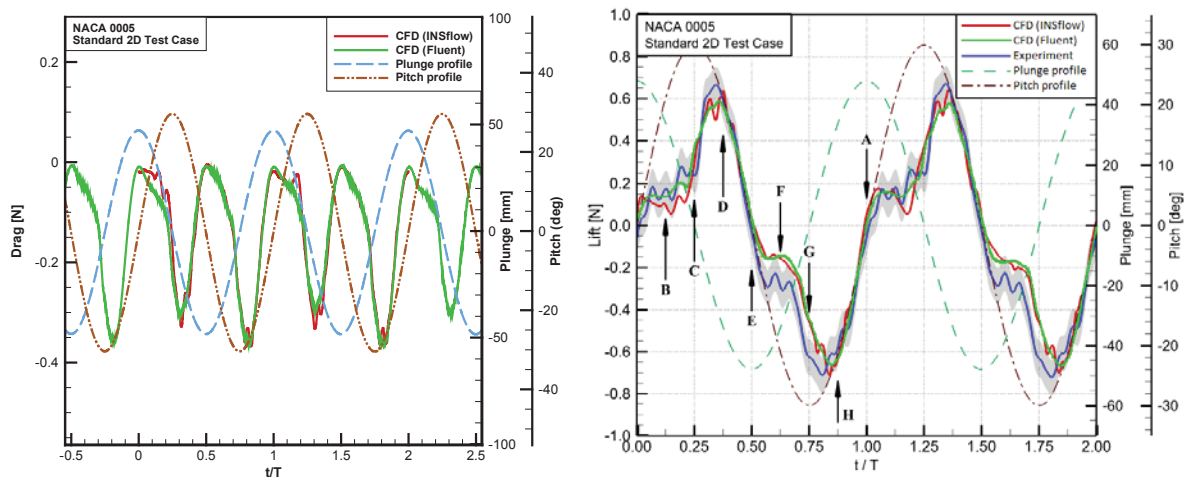


Figure 19: Measured and computed drag and lift forces for the pitching-plunging NACA 0005 airfoil.

Standard 2D test case (wing span 25.4cm). The shaded band represents uncertainty in the lift measurement. The letters represent the occurrence of the PIV and CFD results shown in the next Figure.

The most noticeable discrepancy between the experimental and computed results begins to appear following the start of the upward plunge at $t/T = 0.5$. Here, the magnitude of measured lift is higher than the computed results up to $t/T = 0.8$. This discrepancy is attributed to the attachment of the plunge rods to the upper surface of the airfoil (Figure 10); the attachment is suspected of interfering with the convection of a spanwise vortex from the leading edge to trailing edge of the airfoil. The convection of this spanwise

vortex is illustrated in the CFD results depicted in Frames (E), (F), and (G) ($t/T = 0.5, 0.625$, and 0.75 , respectively) in Figure 21. The interference disrupts the surface pressures at mid-span, giving rise to a higher local pressure than normal on the upper surface which, in turn, contributes to a small increment in the magnitude of the lift force from $t/T = 0.5$ to 0.8 .

In addition to the lift force, which relates to the power that has to be provided to the wing, the other force of interest is the thrust force that can be generated by the wing motion. Two cycles of predicted thrust force (negative drag force) produced by INSflow and Fluent, are superimposed in Figure 19. Thrust is generated during the complete cycle of the wing and no drag is noticed for the prescribed motion. The asymmetry in the down stroke force and the upstroke force can be explained by start-up condition. The wing is motion less at $t=0$ sec and accelerated to the maximum pitch rotation speed that creates asymmetric vortices carried over the following cycles.

7.1.2 Flowfield over the NACA 0005 Airfoil

Figure 20 and Figure 21 illustrates the flowfield over the NACA 0005 airfoil in terms of spanwise vorticity. Particle imaging velocimetry measurements and the results of CFD simulation (INSFlow) are compared against each other at eight equally spaced points of the motion schedule. The PIV results are an ensembled-average of 24 motion cycles; the CFD results are instantaneous and are the product of second-order calculations. Unlike the CFD simulation, PIV results for the upper surface of the airfoil are not available because the surface lay in the shadow of the laser-light sheet.

Frame A corresponds to the start of the downstroke at $t/T = 0$, as well as the end of the upstroke after Frame H. At this instant of the motion schedule, the effective angle of attack, α , is zero because the plunging velocity is zero. A vortex-pair is attached to the airfoil. The first counter-clockwise vortex (red) of this pair stands on the lower surface of the airfoil at the leading edge; the development of this vortex has its origin in the later stages of the preceding upstroke (Frames G and H). Originating from the upper surface of the airfoil, the second vortex (blue) of the pair is counter-rotating and has been shed from the trailing edge; however, it is considered attached because it continues to receive vorticity from the airfoil. The PIV results detect a third, less intense vortex (red-yellow) downstream in the wake of the airfoil. This vortex is “free” - it does not receive vorticity from the airfoil - and is a product of the preceding cycle of motion, corresponding to the current vortex standing at the leading edge of the airfoil. In Frame B, α has passed its first peak (Figure 5). No vortex has formed on the upper surface owing to a phase delay. The first vortex of the pair convects along the lower surface of the airfoil; the second vortex becomes free. The free vortex downstream convects further away in the wake of the airfoil. At the instant shown in Frame C, is midway on its approach to its second peak. Of the first pair, the first vortex has shed from the trailing edge but continues to receive vorticity from the airfoil; the second vortex continues shedding. At the leading edge of the upper surface, the first vortex of a second vortex-pair begins to emerge. By Frame D, the airfoil is approaching the end of its downstroke. The leading-edge vortex on the upper surface continues to develop in situ. The first vortex of the first vortex-pair has shed further from the trailing edge, but still receives vorticity from the airfoil; the second vortex of the pair is convecting as a free vortex.

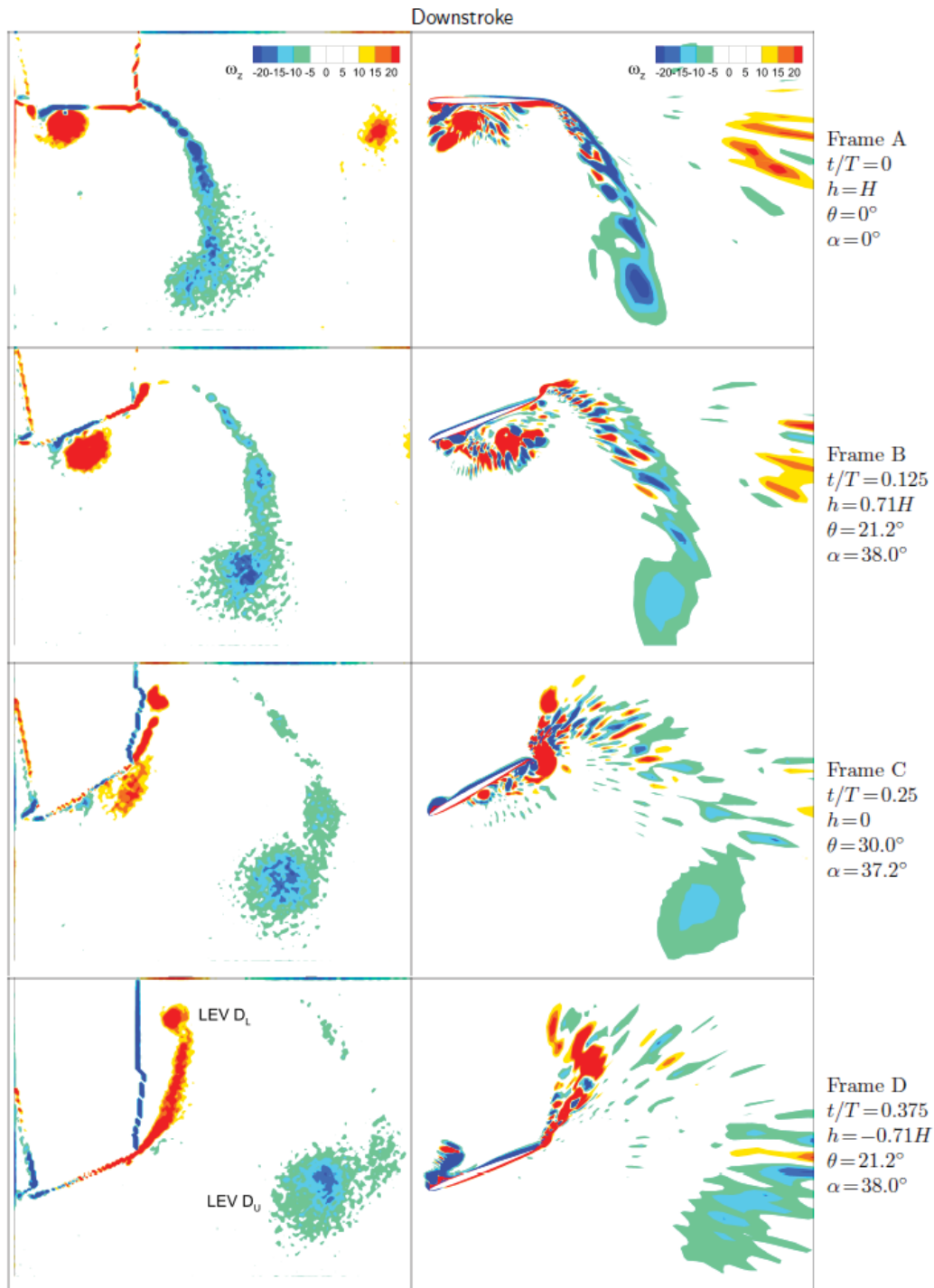


Figure 20: Downstroke : Experimental (left) and computed (right) spanwise vorticity (ω_z) distribution over the pitching-plunging NACA 0005 airfoil. Standard 2D test case; The temporal occurrence of each frame is identified in the previous Figure. The abbreviation “LEV” represents “leading-edge vortex”; the subscripts “L” and “U” represent lower and upper surface, respectively.

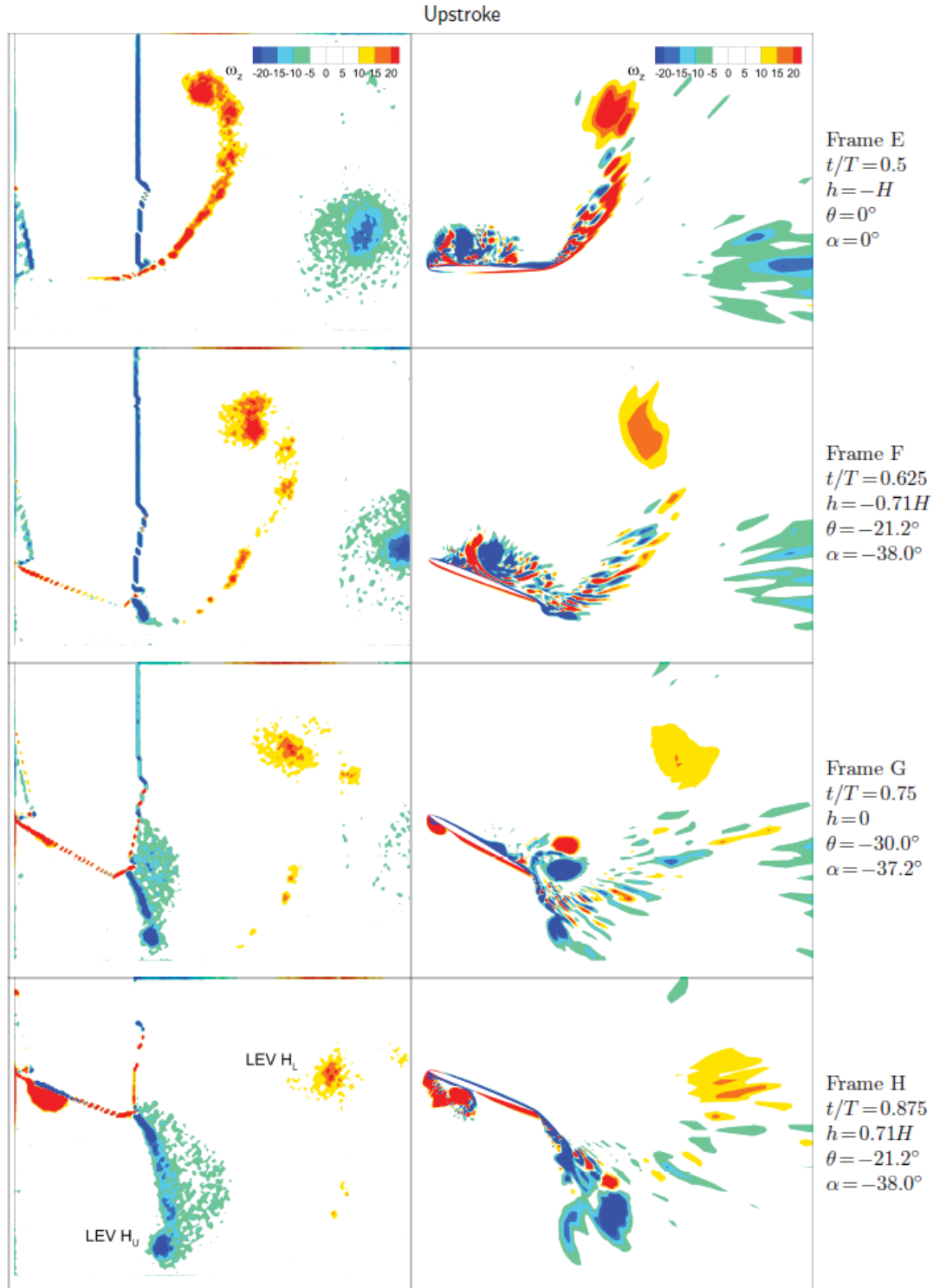


Figure 21: Upstroke (Continued from previous Figure)

After examining Frames A, B, C, and D in connection with the measured and computed lift forces in Figure 19, it becomes evident that the lift force is correlated with the leading-edge vortex, but the realization of lift is phase delayed. The counter-clockwise vortex on the lower surface at the leading edge causes the delay of lift increase, owing the downward aerodynamic force it induces (Frames A and B). As

soon as this vector sheds from the trailing edge (Frame C), the lift begins increasing significantly. At the same time, the generation of the leading-edge vortex on the upper surface augments the lift increase. The lift reaches its maximum when this vortex takes form and begins to convect downstream (Frame D).

The upstroke is represented by Frames E to H inclusive; essentially, the development of the flowfield over the airfoil is the reverse of Frames A to D, with the leading-edge vortex developing on the lower surface instead. As we have noted, the mid-span interference of the plunge rod attachment points with the convection of the upper surface vortex occurs during this portion of the motion schedule.

In general, the flowfield around the airfoil has been simulated reasonably well by the current computations. The numerical simulation has captured successfully the alternating development, convection, and shedding of a leading-edge vortex over both the upper and lower surfaces of the airfoil. However, there are inaccuracies: first, the free vortex convecting downstream in the wake of the airfoil is not detected well; and second, in the latter stages of the downstroke (Frames C and D) and the upstroke (Frames G and H), the vorticity sheet feeding the vortex shed from the trailing edge of the airfoil is not reproduced very well. These are attributed mainly to an insufficient grid density, in particular, in the region extending one chord length from the trailing edge of the airfoil into its wake. The coarse density of the grid generates numerical dissipation which tends to smear the vortex-shedding process.

Earlier, we introduced the notion of an asymmetric wake. This phenomenon is illustrated in the PIV and CFD results presented in Figure 20 and Figure 21. Consider the leading-edge vortices shed from the airfoil at the start of the downstroke (“LEV D_L ” in Frame D) and the beginning of the upstroke (“LEV H_U ” in Frame H). From the PIV results, a cursory sampling of the vorticity magnitudes at the core of these vortices has revealed that the vorticity within LEV D_L is greater than the vorticity within LEV H_U by a factor of approximately two. Farther downstream in the wake, vortices LEV H_L and LEV D_U have dissipated somewhat, having comparable vorticities. Although the motion of the airfoil is symmetric, the wake it creates seemingly is not, which results in an asymmetric lift curve in time. At the end of the downstroke, vortex LEV D_L acts like a counter-clockwise circulation which induces an “additional” downward force on the upper surface of the airfoil. Understandably, this force is larger than the upward force induced by vortex LEV H_U - at the end of the upstroke - causing the aforementioned asymmetry of lift in time.

7.1.3 Effect of Cross-Sectional Profile

The measurements of lift force acting on an airfoil with a NACA 0005 cross-sectional profile and a flat plate of constant thickness (i.e., 5% of chord) are compared in Figure 22. The two sets of results agree reasonably well, although the peak lift developed by the flat plate is slightly less than that developed by the NACA 0005 airfoil. The good agreement suggests the development of aerodynamic loading is driven mainly by the kinematics of the airfoil, not its cross-sectional profile.

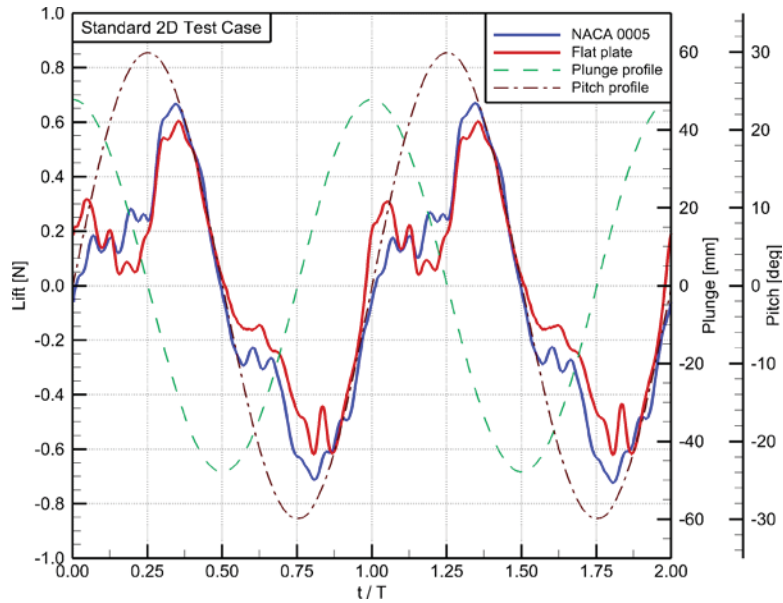


Figure 22: Measured lift force for pitching-plunging NACA 0005 and flat-plate airfoils. Standard 2D test case.

7.2 Standard 2D Test Case with reflection planes

As mentioned in Section 3.3, the reflection planes were used for simulating experimentally and numerically (INSFlow) the clap-fling effect associated with wing-to-wing interaction. Due to mechanical restrictions of the 2D motion rig, the closest position of the reflection planes was chosen to be 1.03 chords (1.03c), as shown in Figure 23. The longitudinal length of the reflection planes was 6 chords (38 cm) in the experiments while it was 21 chords in the CFD simulations. In the numerical simulations, the reflection planes were assumed to be symmetry planes, which indicate fully symmetric flowfields about the reflection planes or, in reality, between interacting wings. The computational domain was split into two blocks (meshes) as the upper and lower parts. Two-dimensional H-type dynamic meshes were used, which allowed for mesh deformation during the computations. Each mesh had 497×129 grid points. Laminar flow was assumed. Since numerical instabilities were experienced in the second-order computations, results from first-order simulations are reported only.

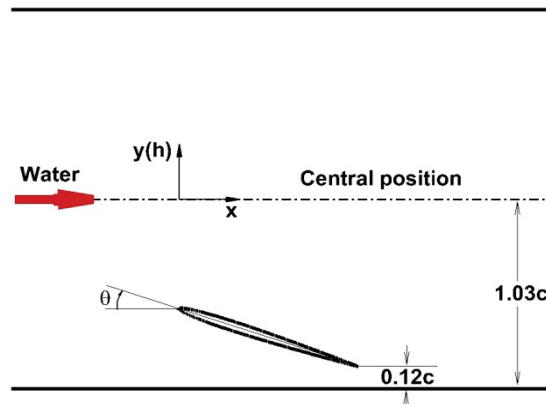


Figure 23: The setup of the reflection planes simulates clap-fling wing-wing interaction

The PIV-measured and CFD-computed flowfields of one pitching-plunging cycle are depicted in Figure 24 and Figure 25. The PIV results are the product of an ensemble-average over 23 cycles. The CFD results presented are for an instantaneous solution. In the CFD simulations for the no-reflection-plane case, the third cycle produced results comparable to the second cycle; however, for the computations with the reflection planes, more than 20 cycles were needed to converge to a steady state of the periodic solution. Although there were discrepancies between the experimental and numerical results, the CFD results captured the major physical features of vortex generation and shedding.

As shown in Figure 24 and Figure 25, the flowfields showed some similarities to those of the test case without the reflection planes. However, noticeable differences were observed:

1. The sizes of the vortices are larger in the wing-wing interaction as compared with those in the no-reflection-plane case, suggesting that the reflection planes, or wing-wing interactions, intensify vortex generation.
2. During the downstroke period of the cycle (plot b), the leading-edge vortex (in blue) on the upper surface of the airfoil occurred earlier, compared with the no-reflection-plane condition. Furthermore, an additional trailing-edge vortex (in red) was also generated on the upper surface. These features are believed to intensify the generation of thrust, as discussed later.
3. At the same time, it appears that suction affects vortex shedding on the lower surface. As shown in plots b and c, the leading-edge vortices (e.g., the counter-clockwise vortex in red on the lower surface near the leading edge) generated during the previous half cycle, shed slower than those in the no-reflection-plane case. In plot c, the counter-clockwise vortex has nearly reached the trailing edge; at this instance in the cycle, it had already started shedding from the trailing edge at the no-reflection-plane case.
4. When the airfoil approached the bottom reflection plane (plot d), a high-speed flow was observed on the lower surface. The flow speed reached five times higher than the freestream speed while it was about three times the freestream speed in the no-reflection-plane case. In plot e, a flow reversal was observed between the airfoil and the reflection plane, which allows the flow to turn the leading edge of the airfoil.

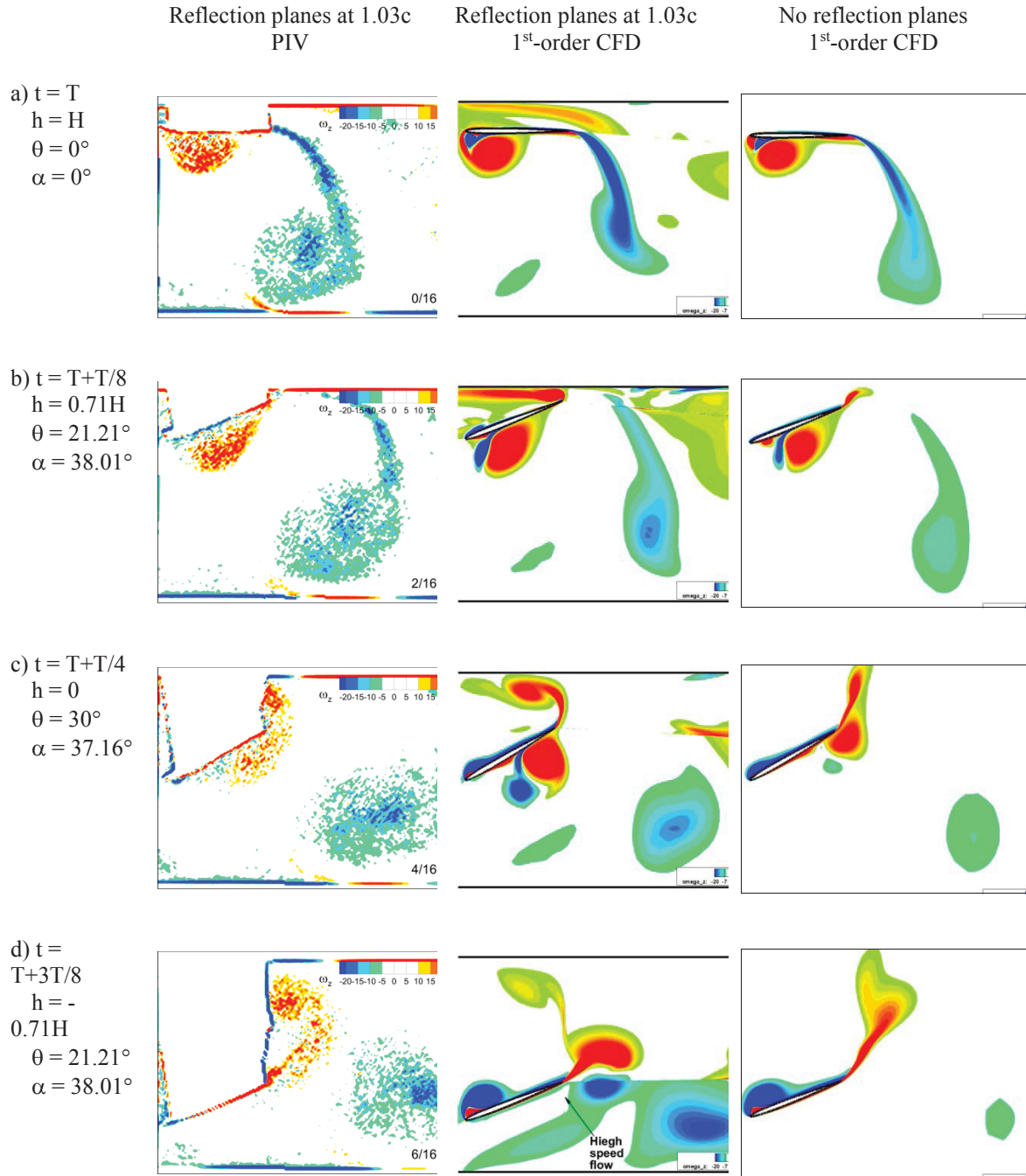


Figure 24: Downstroke; at left and centre are spanwise vorticity (ω_z) distributions over the pitching-plunging NACA 0005 airfoil at $Re = 10.5 \times 10^3$, with reflection planes at 1.03c from the central position.

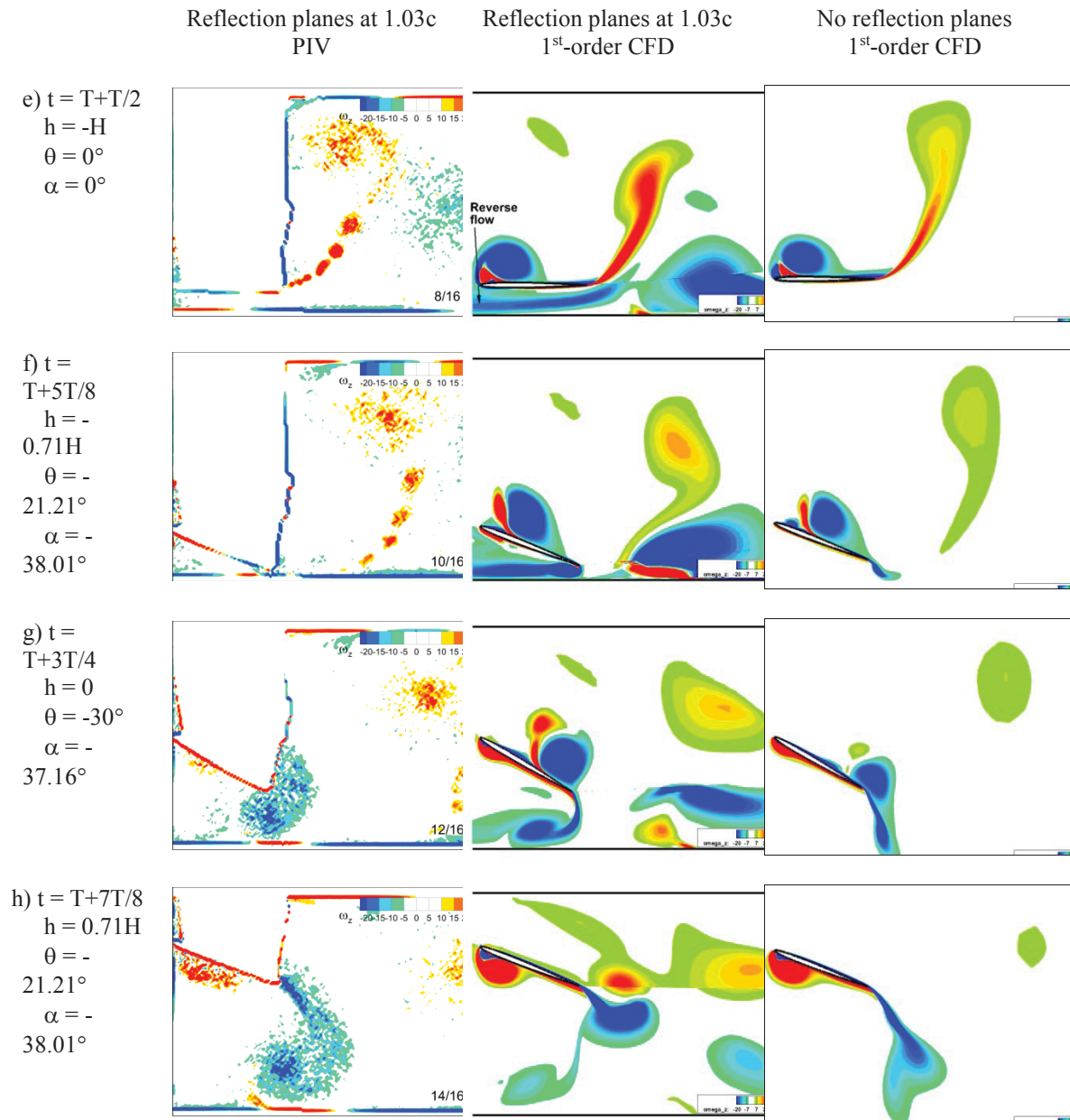


Figure 25: Upstroke: Continued from previous figure

Figure 26 compares the computed lift coefficient with that obtained in the experiment. While both instantaneous and ensemble-averaged experimental data are presented here, only instantaneous CFD results are depicted since the first-order CFD simulations produced nearly periodic solution as soon as the computations converged. Although apparent discrepancies between the numerical and experimental results are noticeable, the agreement is considered suitable for the validation of an engineering tool.

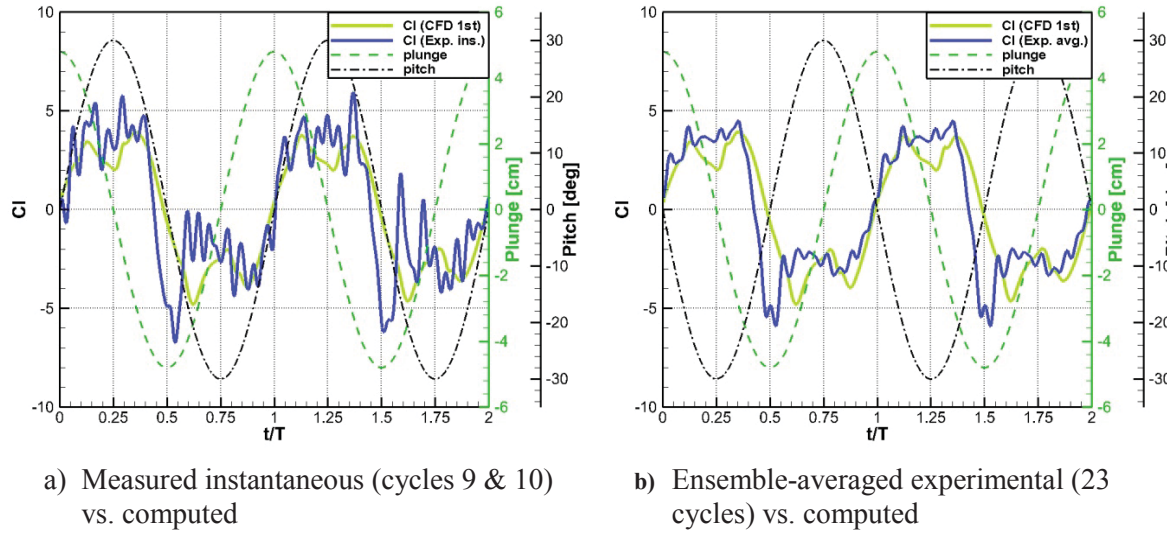


Figure 26: Computed lift coefficients compared with experimental results for the case with reflection planes located at $1.03c$ from the central position

Figure 27 further compares the effects of the reflection plane location on the aerodynamic coefficients. In general, the reflection planes intensified the force generation at the test conditions. The closer the reflection planes were, the stronger effects were observed. Table 8 summarizes the reflection plane effects on the thrust generation and propulsion efficiency. Negative drag coefficients indicate thrust generation. As expected, the clap-fling mechanism improved the thrust generation. At the closest reflection plane placement ($1.03c$), the thrust coefficient is greater by 170%, compared with the no-reflection-plane case. Surprisingly, the propulsion efficiency deteriorated slightly.

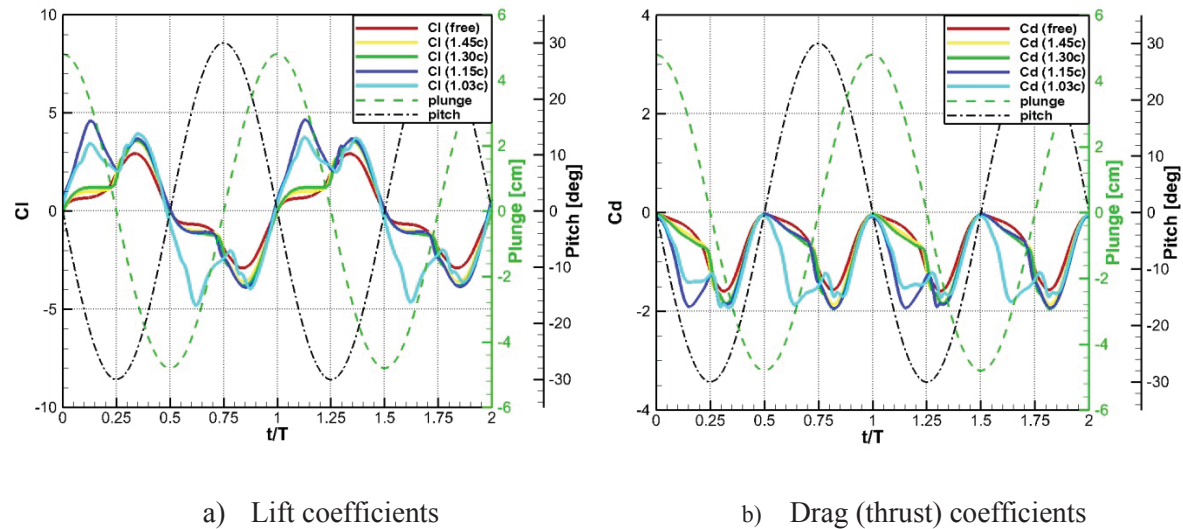


Figure 27: Effect of the proximity of the reflection plane on the lift and drag coefficients

Table 8: Summary of clap-fling (wing-wing interaction) effect (1st-order CFD results)

Reflection plane location	Averaged drag coefficient C_d	Propulsion efficiency η_p
No planes (Freestream)	-0.64	25.4%
1.45c	-0.74	24.7%
1.30c	-0.78	24.7%
1.15c	-0.99	24.5%
1.03c	-1.08	24.6%

Asymmetry in time of the flowfield behaviour and the resulting aerodynamic coefficients was observed for no-reflection-plane case, as shown in Figure 19 to Figure 21. These results are believed to be attributed to influence of the leading-edge vortices shed from the airfoil but remained in the wake [5][6]. This phenomenon was not observed in the 1st-order CFD simulations for the no-reflection-plane case (Figure 24 to Figure 26). This is understandable because 1st-order simulations are more dissipative and numerically smear the asymmetric distributions. However, despite the use of 1st-order CFD simulation, asymmetry was apparently shown for the test case with reflection planes at 1.03c. This was attributed to the wing-wing interaction as supported by plots b and f in Figure 24 and Figure 25, which is a potential indication that wing-wing interaction has a stronger influence on the flowfield than the wake of the airfoil.

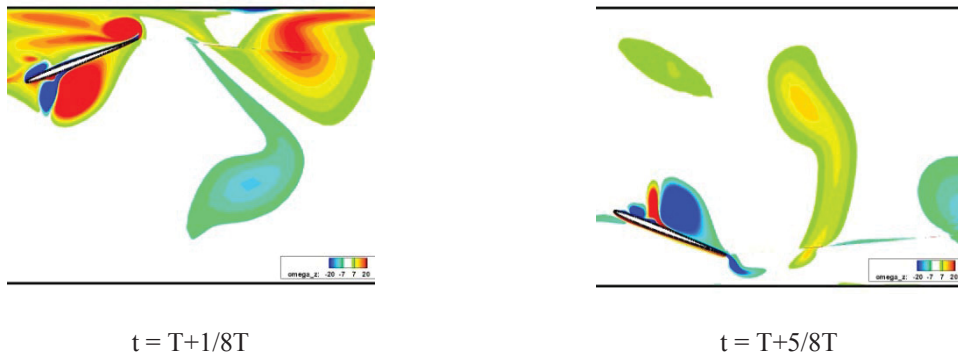


Figure 28: Computed spanwise vorticity (ω_z) distribution over the pitching-plunging NACA 0005 airfoil at $Re = 10.5 \times 10^3$, with reflection planes at 1.15c

It is interesting that the test case with reflection planes located at 1.15c showed strong asymmetry in time. In Figure 27, a peak in the lift coefficient is observed clearly at $t = T + 1/8T$, but not correspondingly at $t = T + 5/8T$. In order to help understand the relevant flow physics or correlations, the flowfield of the selected test cases at these time instances in the cycle are illustrated in Figure 28. At $t = T + 1/8T$, as the airfoil plunges downward from the upper reflection plane, leading-edge and trailing-edge vortices are observed on the upper surface of the airfoil, which is similar to that of the 1.03c case. A flow reversal is also observed between the airfoil and the upper reflection plane. However, this is not the case for $t = T + 5/8T$; neither the leading-edge vortex, nor the reverse flow are observed on the lower surface of the airfoil.

7.3 Flexible cambered thin airfoil results

As described in Section 3.5, an artificial test case with a flexible cambered thin airfoil was defined. Numerical simulations (INSFlow) were performed using the second-order scheme. The grids were similar to those used for the reflection-plane cases, but the farfield boundaries were located at 10 chords away from the airfoil. Investigations were carried out for the NACA 0005 airfoil. The computed aerodynamic coefficients are depicted in Figure 29; the propulsion efficiencies of the flexible thin airfoil and the NACA 0005 airfoil are compared in Table 9. The simulations revealed the potential benefit that the cambering feature could bring. The flowfields are depicted in Figure 30 to Figure 32. It is apparent that the leading-edge vortices of the flexible cambered airfoil shed slower compared with those of the NACA 0005 airfoil. The leading-edge vortex on the cambered airfoil was still nearly attached to the airfoil at time instant $t = T+7T/8$ while it started shedding on the NACA 0005 airfoil at $t = T+3T/4$. It is believed that this vortex is responsible for intensifying the generation of thrust, which appears in Figure 29.

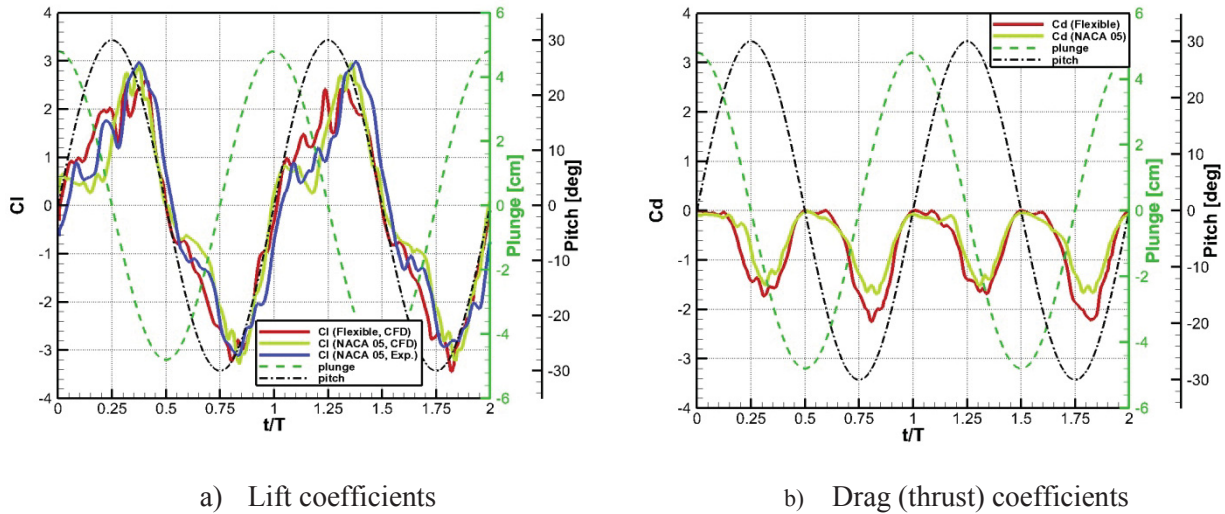


Figure 29: Computed aerodynamic coefficients of the cambered airfoil in comparison with NACA 0005 airfoil

Table 9: Aerodynamic performance of the cambered airfoil (2nd-order CFD results)

	Averaged drag coefficient C_d	Propulsion efficiency η_p
Rigid NACA 0015	-0.62	25.3%
Cambered thin airfoil	-0.79	27.2%

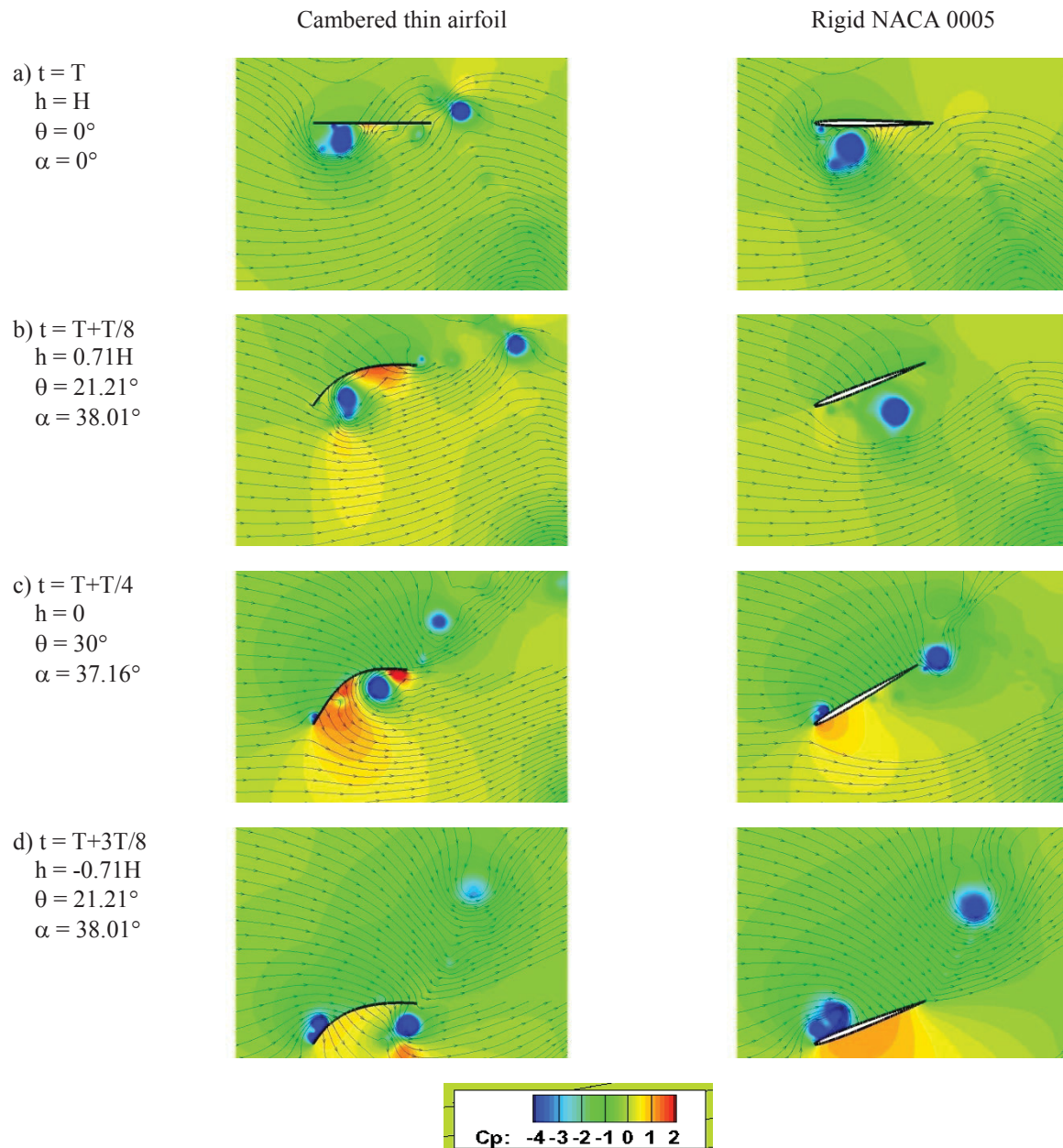


Figure 30: Downstroke: Computed dimensionless pressure distribution over the airfoils at $Re = 10.5 \times 10^3$, $V_\infty = 0.0635$ m/s, second-order CFD solution

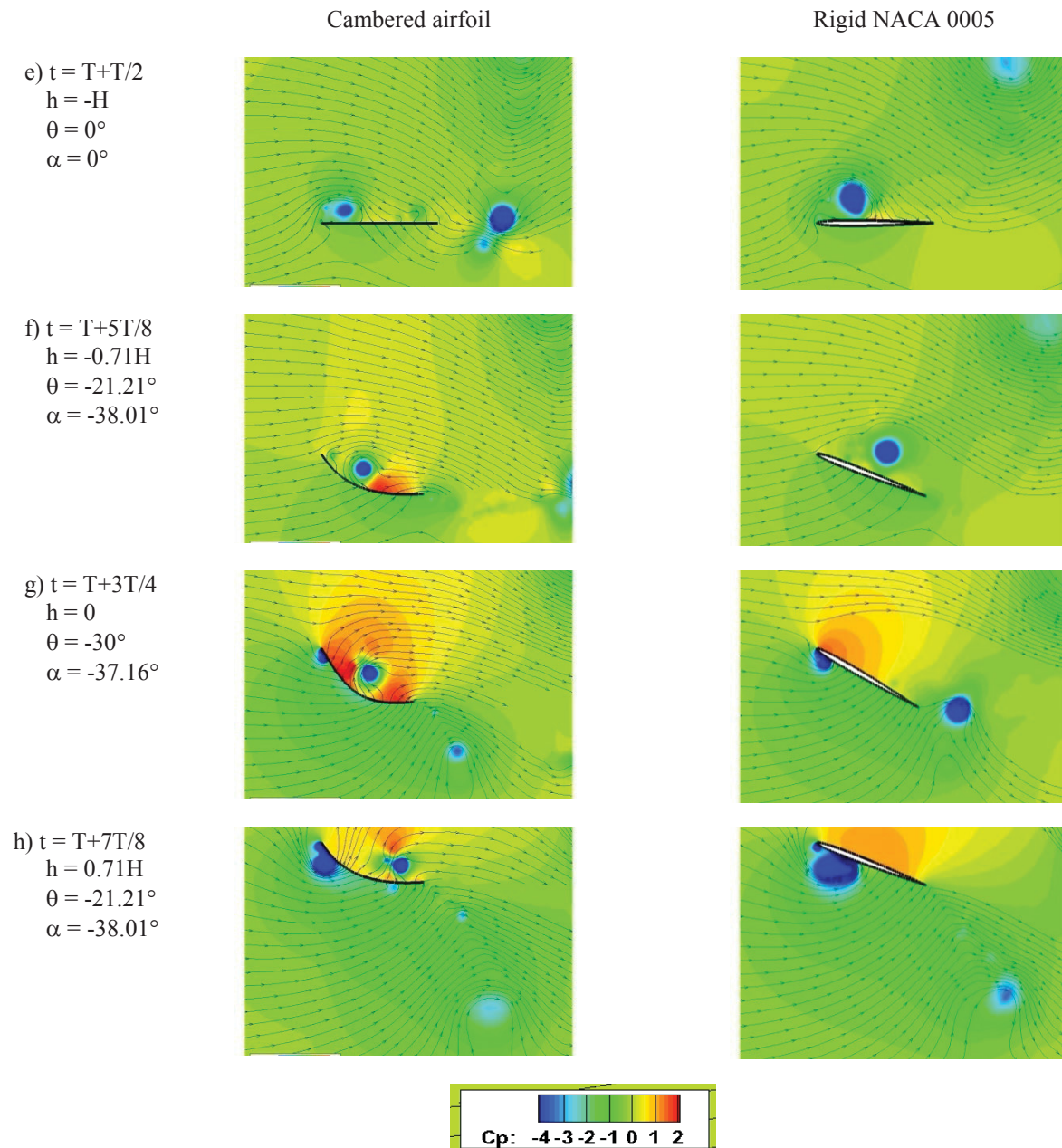


Figure 31: Upstroke: Continued from previous figure

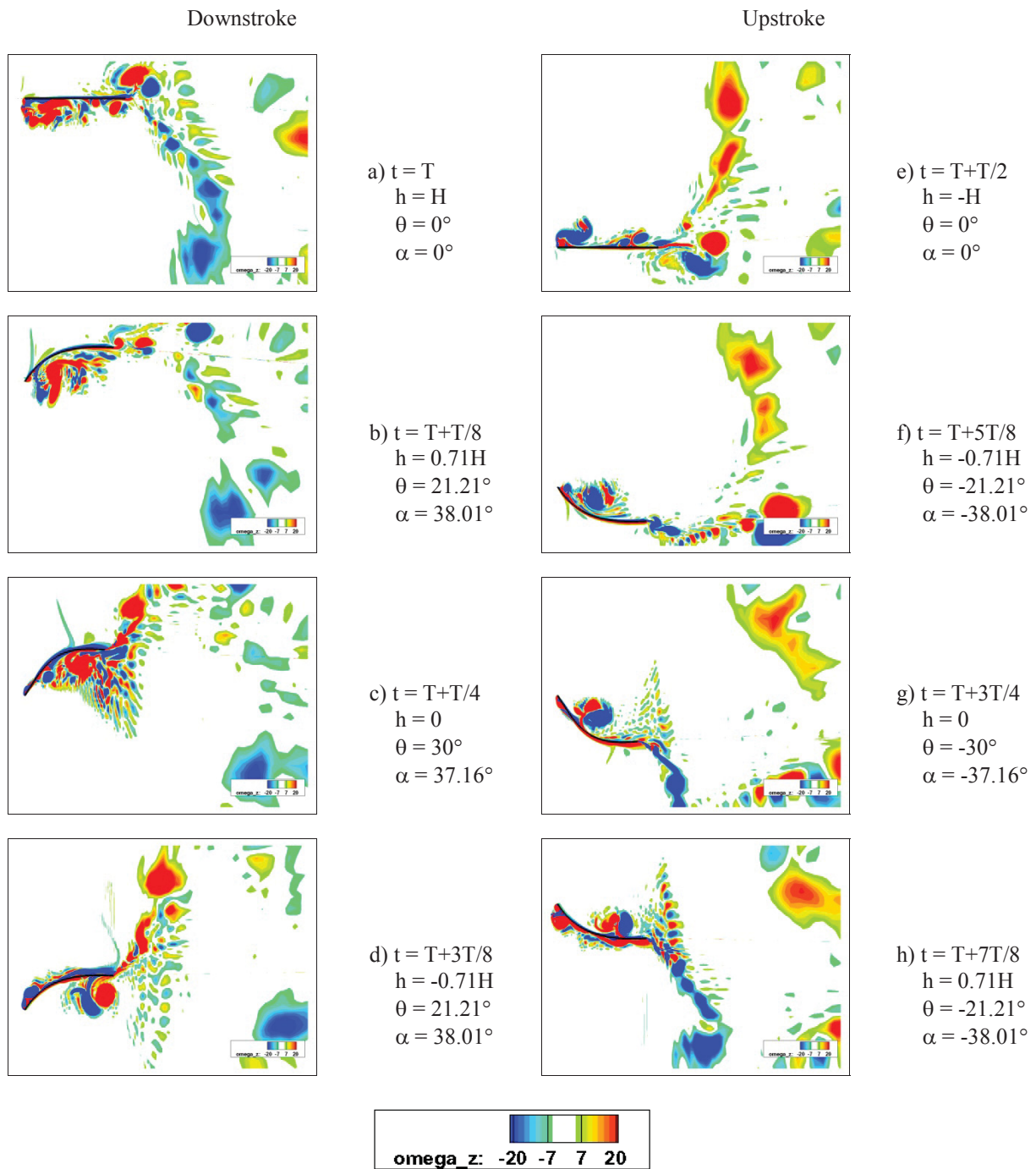


Figure 32: Computed spanwise vorticity (ω_z) distribution over the flexible cambered thin airfoil at $Re = 10.5 \times 10^3$, $V_\infty = 0.0635$ m/s, second-order CFD solution

7.4 Standard 3D Test Case

7.4.1 Lift and Drag Forces

One cycle of measured and computed lift and drag forces are superimposed in Figure 34. Again, the experimental results are a subset of an ensemble-average of 24 three-cycle time series; the CFD results are from the fourth cycle of a four-cycle computation. The motion profiles, again, synchronize the presentation of the two data sets.

Similar to the results of the 2D test case, there is good agreement between the measured and computed results. There is repeatable behavior with the flapping schedule and a phase shift is not noticeable. For the most part, the computed lift force falls within the uncertainty band of lift measurement, while the computed drag force agrees very well with the drag measurement and its associated uncertainty. The peaks in the measured lift and drag forces exhibit an asymmetry which is attributed to the interaction of the wing model with its asymmetric wake. The computed lift and drag forces, on the other hand, are symmetric, indicating that the simulation has not captured the interaction of the wing model and an asymmetric wake, which we suspect exists based on the findings from the 2D test case. The simulation may have missed the interaction because the computed results are the product of first-order calculations which tended to be too dissipative.

Another discrepancy in the results is evident as the wing model begins to return from its peak flapping amplitude of 15 degs. From either of these flap positions, for a duration of approximately one-quarter of a cycle, the measured lift and drag forces are slightly higher than the computed results. The discrepancy is suspicious because of its regularity and its effect on both lift and drag simultaneously, but could not be resolved.

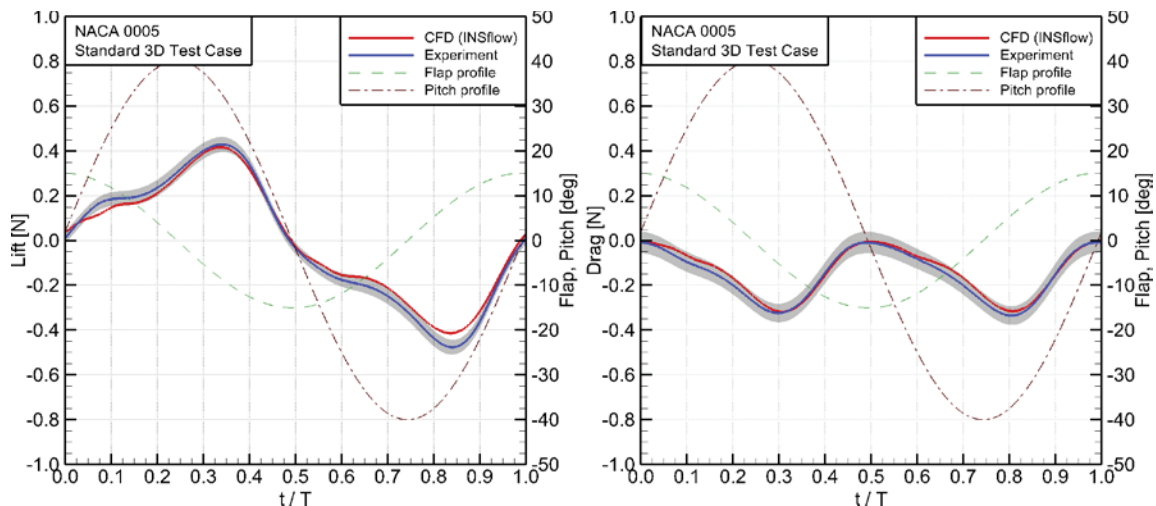


Figure 33: Measured and computed lift and drag forces for the flapping NACA 0005 wing. Standard 3D test case; The shaded bands represent the uncertainty in the lift and drag measurements.

7.4.2 Effect of Cross-Sectional Profile

The measurements of lift and drag forces on wing models with a NACA 0005 cross-sectional profile and a profile of constant thickness (flat plate) are compared in Figure 34. Similar to the 2D test case (Figure 22), the two sets of data agree very well. The good agreement reinforces the earlier suggestion that the development of aerodynamic loading is influenced largely by the kinematics of the airfoil/wing.

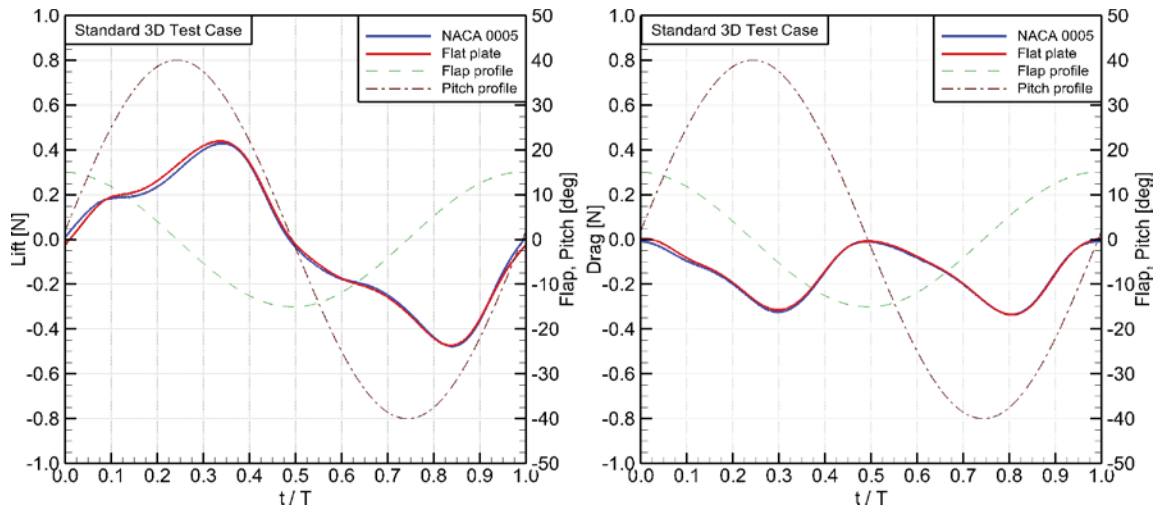


Figure 34: Measured lift and drag forces for flapping NACA 0005 and flat plate wings.
Standard 3D test case: $V_\infty = 0.0635$ m/s, $Re_f = 14.3 \times 10^3$, $f = 0.46$ Hz.

7.5 Remarks

Except for the 2D standard test cases, numerical instability was encountered in all calculations, owing to complex flow physics or/and severe grid deformation. Further investigation is needed to improve both numerical stability and accuracy.

Both flexibility of the airfoil and the clap-fling mechanism help generation of thrust.

As an ancillary finding of the experimental work, a perfunctory investigation of the PIV results revealed that the immediate wake of the pitching-plunging 2D airfoil is not symmetric in time, i.e., the leading-edge vortices of the upper and lower surfaces of the airfoil possess significantly different magnitudes of vorticity after shedding from the trailing edge. This finding has prompted the notion that these vortices, in turn, have an asymmetric influence on the loading of the airfoil. Further reflection of this notion, however, is necessary.

In addition, a cross-check with the experiments has shown that further refinement of the grid in the wake region is needed, if a more accurate wake solution, in terms of resolving shed vortices, is required from the numerical simulations.

Kinematic motion schedule plays the primary role in the generation of thrust force while airfoil profile seems a secondary parameter, implying that the non-circulatory component (added mass) is dominant over the circulatory aerodynamic component.

Also, the formation of the leading-edge vortex on the suction surface of the airfoil/wing augments the generation of aerodynamics forces (lift and thrust); however, the downstream convection of the vortex on the pressure surface causes a delay of the force increase.

8 Engineering design and optimization tool

In order to both understand and exploit the aerodynamics of a vigorously flapping insect-type wing suitable for hovering flight, a vortex panel based engineering model was developed. Both two dimensional (2D) and three dimensional (3D) versions were created and their development and use are briefly described in this chapter. Details of the model are given in [10] [22]. Because panel models solve much more quickly than full Navier-Stokes solutions, they are well suited to design and optimization tasks. Both the 2D and 3D models were additionally used as the objective function in an optimization routine.

The engineering model is written for Matlab, however, given the methodologies presented in this report it would be possible to implement the method in any language.

Note that a compiled language would give even faster solution times than does Matlab which is an interpreted language.

The present work builds upon work done on the Mentor program at the University of Toronto Institute for Aerospace Studies [34][24]. Mentor was the world's first hovering flapping wing vehicle and it first hovered stably in March 2002.

8.1 2D model

The detailed description of the 2D model can be found in [10] [22]. Only a brief overview is given below.

8.1.1 Attached flow model

The attached flow model, which forms the foundation for the separated flow model to be discussed later is a 2D vortex panel method and is relatively unchanged from the model devised for the Mentor program [34]. Tangential flow boundary conditions are enforced at panel control points. An additional boundary condition that conserves vorticity between time steps fixes the strength of the nascent trailing edge wake vortex. The wake vortices are allowed to move freely with the local velocity at their centres. Instantaneous pressure values on the airfoil are calculated using the unsteady Bernoulli equation. Pressures are integrated to calculate forces and moments. From this, power usage and efficiency is calculated.

The very nature of an engineering model allows certain aspects of the model to be turned off. Alternately, the effects of certain elements may be artificially amplified to determine the strength of their influence on important parameters such as thrust production, or power consumption. This capability gives the user very useful insights into which parameters within the problem space dominate and then how to manipulate them for greatest effect.

The model is capable of modeling stall and the creation of a leading edge vortex (LEV). This capability may be switched on or off. When the leading edge stall model is switched off, a wake emanates only from the trailing edge. Attached flow over the airfoil is prescribed through the no-normal-flow boundary conditions at the control points.

8.1.1.1 Application of Attached Flow Model

The standard 2D test case is known to produce separated flow from the sharp leading edge as can be seen from CFD and PIV flow-visualization. Nevertheless, it was desired to see to what extent the leading edge vortex affected the solution and so the standard 2D test case (variant with $H/c = 1$) was run with the LEV model turned off. The result is plotted with a comparison to the Fluent Navier-Stokes solution for the same case in Figure 35. The agreement is excellent, especially given the simplicity of the model. This result is encouraging in that the simpler, more robust, attached-flow model gives useful results for this test case where large-scale separated flow is known to exist. This solution gives average values of thrust that are within 3% of the Navier-Stokes solution. This level of accuracy is sufficient for mapping the design space and for optimization. In this case the LEV does not substantially affect the solution. The traditional bound circulation model of lift captures the dominant source of force. The main effect of the LEV in this case is to at first slightly reduce the drag spike and then to subsequently increase it. This can be seen by comparing the drag peaks of the two solutions in Figure 35. There is also a slight phase difference, with the panel model solution slightly leading the Navier-Stokes solution.

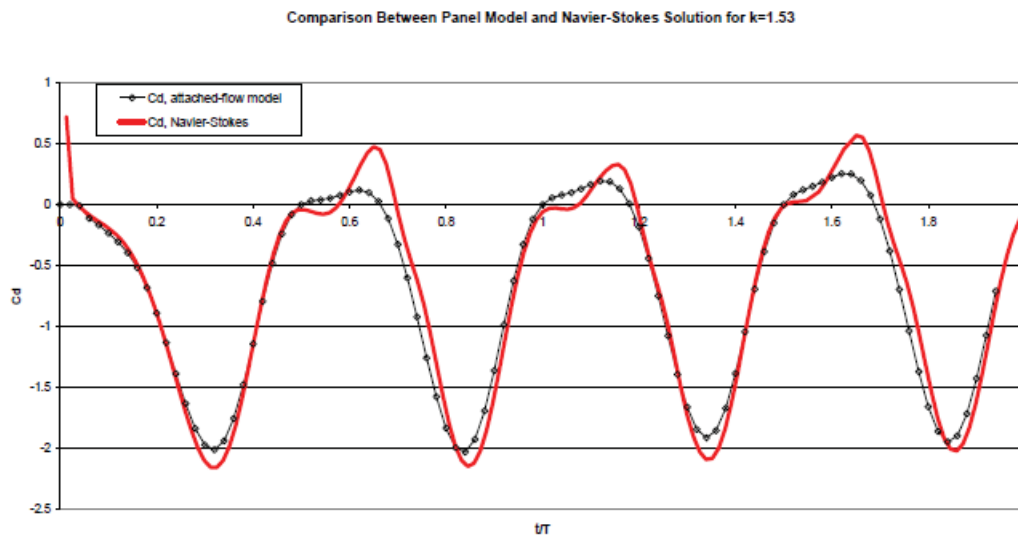


Figure 35: Drag coefficient comparisons between the attached-flow panel model and Fluent. Note the slight phase shift and discrepancies at the extremes of thrust/drag production.

To determine how robust the panel model is over the design space, seven different variations on the standard test case were run. Only the flapping frequency of the standard test case was altered to give reduced frequencies ranging from $k = 0.1$ to 10. In all cases, the reduced amplitude (H/c) was kept constant as this is a geometric property of the Mentor type wing and actuation scheme. Figure 36 shows a comparison of the drag coefficient (negative values show thrust production) for the different reduced frequencies.

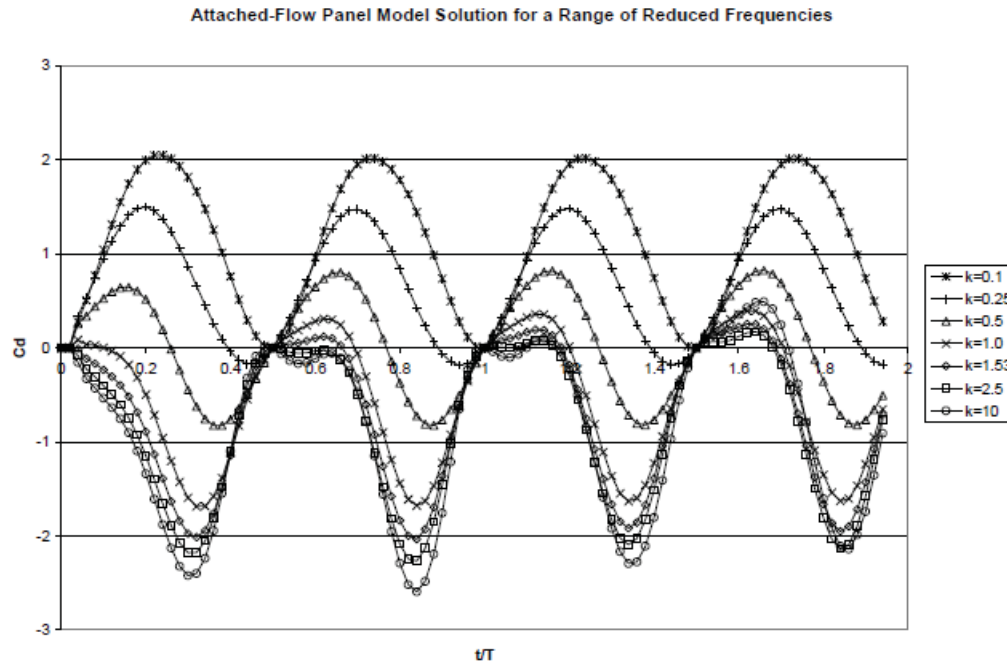


Figure 36: Attached-flow panel method to compare drag coefficient for a range of reduced frequencies that cover fast forward flight to near-hover.

Note that the shape of the drag coefficient curve is very similar between cases where reduced frequency is greater than one. For reduced frequency $k > 1$, the flapping velocity dominates to such a degree that these cases are all functionally similar to a hover. This shows the validity of imposing a freestream velocity in the standard test case that was equal to the induced velocity predicted by actuator disk theory. In the standard NAV test case, the imposed freestream velocity gives a reduced frequency of $k=1.53$ which is in the hover equivalent range.

Figure 36 also shows the reference velocity used for nondimensionalization is appropriate. Though actual thrust production varied substantially between these cases since flapping frequency varied by two orders of magnitude, the maximum values of drag coefficient does not vary largely between functionally similar cases ($k > 1$).

8.1.2 Separated Flow Model

To obtain even better agreement at the peaks of thrust and drag, and to determine if the LEV is, or could be, a major contributor to efficient thrust production, a new model for leading edge separation was developed. This leading edge separation model can be broken down into two parts. The first determines if the airfoil is stalled. The second then determines the instantaneous strength of the stalled leading edge wake.

8.1.2.1 Stall Angle of Attack

Because the leading edge stall model can be turned on and off during the cycle, a trigger is needed to tell the model that the airfoil has stalled and that separation is occurring. To do this, the instantaneous angle of attack at the leading edge is calculated. The angle of attack at the leading edge is the result of two separate elements. The first is due simply to geometry and the airfoil motion. The second element is the

result of the disturbance velocity. In other words, it is the velocity due to the presence of all vortex elements. The wake emanating from both the leading and trailing edges affects the angle of attack at the leading edge. At some times in the cycle it may delay stall and at others it may prolong it. The angle of attack is calculated and compared to a stall trigger angle, which may be higher than the steady state stall angle due to dynamic effects, and the stall model is switched on or off. The stall trigger angle may be set from experiment or to match the behaviour of known cases. In general, a value of 20 degrees for onset of dynamic stall works well in the model.

8.1.2.2 Stall Location

Unlike conventional fixed-wing airfoils with thickness on the order of 12%, on very thin membrane-type wings as used on Mentor, the stall location is governed by geometry and not pressure gradient. This has been confirmed with experimental flow visualisation and with CFD. Therefore, within the present model, the stall location is set right at the leading edge. The nascent leading edge wake vortex is placed slightly ahead of the leading edge and tangent with the chord line and with spacing consistent with bound vortex spacing. This placement is sufficiently close to the leading edge so as to model separation from the sharp leading edge. Also, a vortex released slightly ahead of the airfoil is free to move either above or below the airfoil with the local velocity at its centre. This is important since the airfoil is constantly changing direction and separated vortex elements from the leading edge must be free to move over either side of the airfoil.

8.1.2.3 Stall (LEV) Model

The leading edge vortex model is similar in concept to a stall model developed by Katz [36] which was applied in the case of stalled flow over a fixed, thin airfoil at a high angle of attack. Whereas the Katz LEV model was applied to a fixed airfoil that was known to be stalled at all times, in the present model, the airfoil may be stalled or unstalled at different points in the cycle. Furthermore, the top and bottom of the airfoil change places over the cycle, and the sign (rotational sense) of the leading edge wake may alternate which adds some computational complexities. The Katz model for the LEV calculates the nascent leading edge vortex strength using the difference in velocity over the shear layer that emanates from near the leading edge as a result of the stall. The nascent LEV's strength, Γ_{LE} , is calculated using:

$$\Gamma_{LE} = \frac{1}{2} K (V_{upper}^2 - V_{lower}^2) \Delta t \quad (42)$$

Where:

K is a correction factor (set to K=1 for all results presented here)

V_{upper} is the velocity above the separated shear layer

V_{lower} is the velocity below the separated shear layer

Δt is the time step

Katz calculates the upper and lower velocities by taking a velocity survey above and below the shed vortex sheet. This calculation for the strength of the newest leading edge wake vortex is not a part of the linear system of equations that is solved at every time step, but a separate calculation. In a given time step, the system of equations is solved first, fixing the values of the bound vortices and the nascent trailing edge wake vortex. Then the strength of the nascent leading edge wake vortex is calculated from the information in the current time step.

Katz states that the solution was dependent on the location of the velocity survey points and their proximity to the vortex sheet. This variation is likely due to the nature of discrete vortex models where the tangential velocity right at the centre of a point vortex is infinite. In the present model a more direct method to solve for these velocities is utilized that is not dependent on the location of a velocity survey point. The velocity over the top of the airfoil at the leading edge is known from the solution for the bound circulation. This velocity is assumed to be equal to the velocity that goes over the shear layer, since the shear layer emanates from very close to the leading edge. The velocity under the shear layer is assumed to be small, since it is in the separation bubble. It is set to zero as Katz does in some versions of his model. The sense of rotation of the nascent leading edge wake vortex is set by using the sign of the angle of attack at the leading edge.

8.1.2.4 Application of the Separated Flow Model

The panel model with the stall model switched on was applied to the standard 2D NAV test case (variant with $H/c = 1$). The agreement in the areas of the thrust/drag force peaks is improved compared to the attached flow model. A comparison between the panel model and the Fluent solution is shown in Figure 37.

In this test case, introduction of the LEV does not dramatically alter the solution. The thrust and drag peaks match more closely with the Navier-Stokes solution and the phase shift between solutions is nearly eliminated. Comparing the wakes between the attached-flow and separated-flow models running the same standard test case was instructive. The main role of the LEV was to delay the drag production phase of the cycle, and then subsequently to increase drag production. The reason for this can be seen clearly in the vorticity contours taken from CFD and experiment for this case (Figure 20 and Figure 21). In Frame H, the airfoil is moving up, and the positive thrust direction is to the left. Here the position of the LEV is favourable with respect to thrust production. That is, the low pressure vortex produces force in the desired thrust direction (left). A short time later in the same cycle (Frame B), the airfoil is now moving down and the LEV has traveled along the airfoil to the right and the airfoil's pitch orientation has changed such that the low pressure vortex now causes drag. Appropriate pitch and plunge profiles, including non-sinusoidal motions, may allow for a better exploitation of the LEV. Because the present model solves so quickly compared to Navier-Stokes solutions, it is well suited to optimization routines.

Comparison Between Panel Model and Navier-Stokes Solution for $k=1.53$

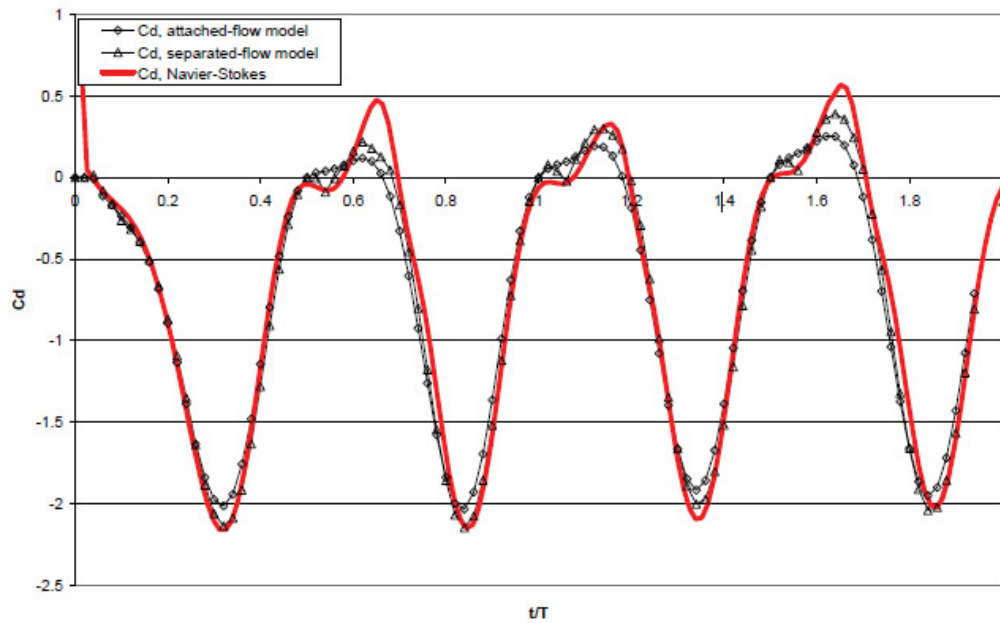


Figure 37: The separated-flow panel model captures the jog in the drag portion of the cycle, where initially drag production is decreased then increased. The attached-flow solution is plotted for comparison.

Navier-Stokes solutions for the largest and smallest reduced frequencies ($k=0.1$ and $k=10$) of Figure 36 were obtained for comparison to panel model solutions. The low reduced frequency case (Figure 38) represents the vehicle in fast forward flight. In this case, no thrust is produced at all, only drag. Figure 39 presents the results for $k=10$ which is close to the hover condition.

Where flow phenomena that are driven by the flapping frequency dominate, such as in the $k=10$ case, the separated-flow panel model does an adequate job of predicting forces. In contrast, the attached-flow model underpredicted peak thrust force by approximately 30%.

When flow phenomena exist at frequencies higher than the driving frequency, the panel model did not capture these effects though it did capture their average trend. All panel model solutions in this section were obtained with only 50 time steps per flap cycle. Perhaps substantially increasing time-step resolution would allow the panel model to capture higher frequency behaviour, though this would increase the computation time. Nevertheless, near the important hover condition, where the dominant flow phenomena occur at close to the driving frequency, the separated-flow panel model does an adequate job of force prediction.

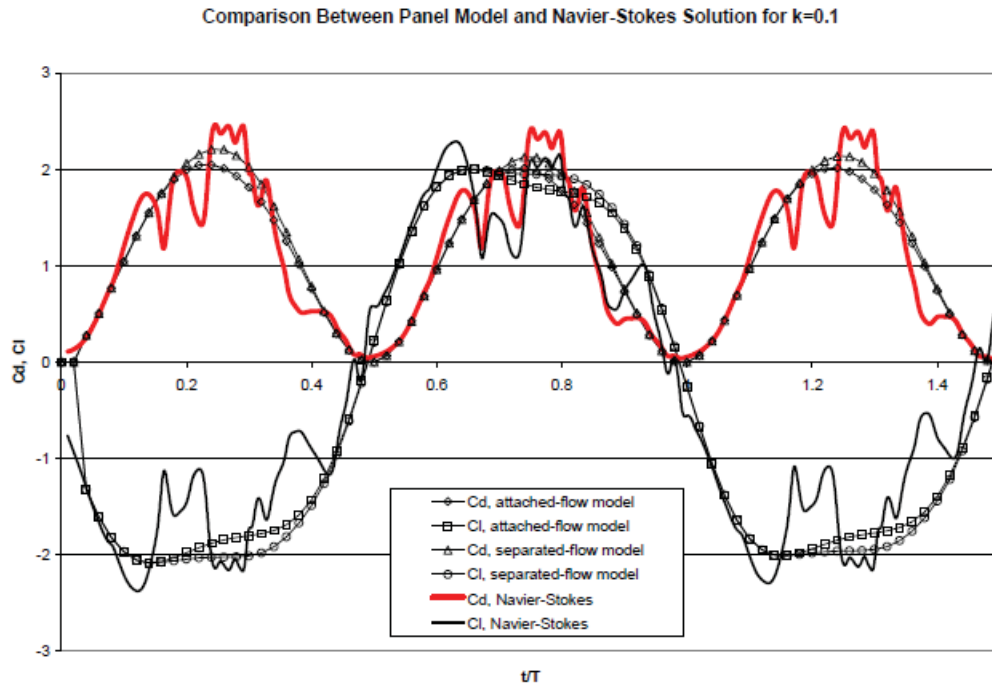


Figure 38: Low reduced frequency case ($k=0.1$) comparison of panel model to Fluent Navier Stokes solution.

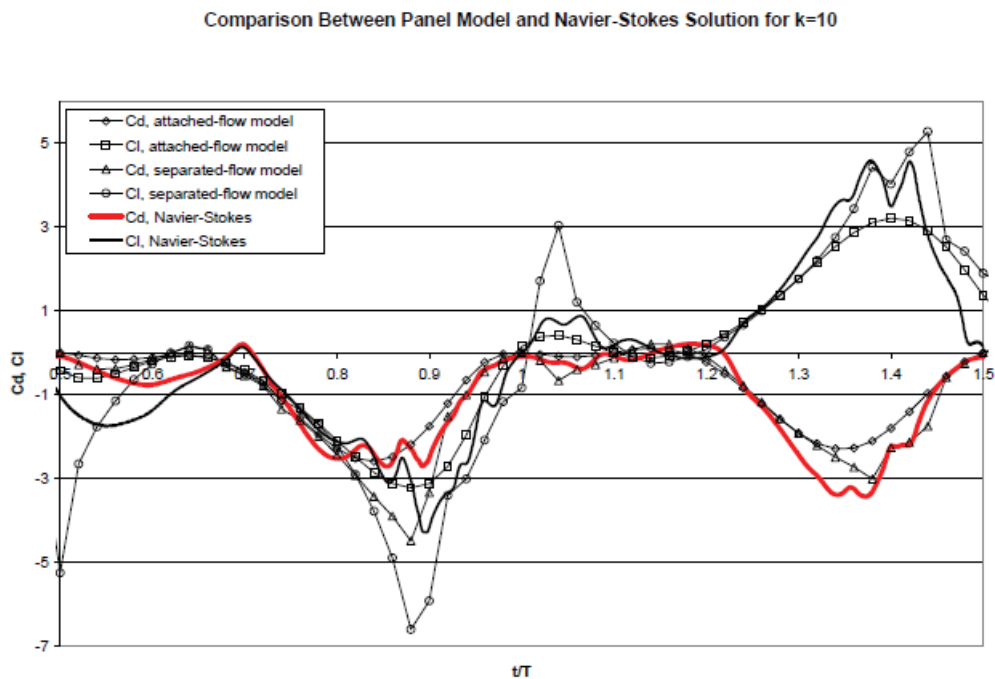


Figure 39: High reduced frequency case ($k=10$) comparison of panel model to Fluent Navier-Stokes solution.

8.1.3 Output from the code

The output from the code includes :

Force coefficients: Time-dependent force coefficients normalized in the usual manner using the reference velocity V_{ref} .

Aerodynamic Power Required: The power required to move a single panel of the airfoil is the force on that panel times the velocity that the panel moves in the direction of the force. The total power required at a given time step to overcome the aerodynamic force is the sum of the power required to move all panels:

$$P_{aero} = -\sum_{i=1}^n (\vec{V}_{kin})_i \cdot d\vec{F}_i \quad (43)$$

Inertial Power Required: The power required to overcome inertia is given by the product of the mass of a panel and the acceleration of that panel:

$$P_{inertia} = -\sum_{i=1}^n (dm \vec{A}_{kin})_i \cdot (\vec{V}_{kin})_i \quad (44)$$

Where dm is the mass of the panel, and in the present model the total airfoil mass is distributed evenly between the panels. The kinematic acceleration is found as:

$$(\vec{A}_{kin})_i = \frac{(\vec{V}_t - \vec{V}_{t-\Delta t})_i}{\Delta t} \quad (45)$$

Thrust to Power Ratio: The thrust to power ratio is found by dividing the mean thrust produced during a cycle by the power required during that cycle. Because in theory the wing could require negative power as it is decelerating, though this would be difficult to harness in reality, negative portions of the power requirement are set to zero. The total power requirement is given by the positive components of:

$$P_{required} = P_{aero} + P_{inertia} \quad (46)$$

The thrust to power ratio is the mean thrust over a cycle divided by the mean power requirement during the cycle:

$$T/P = \frac{\bar{T}}{\bar{P}_{required}} \quad (47)$$

Figure of Merit: The figure of merit is the ratio of the ideal minimum power required to generate a given thrust to the actual power required to produce that thrust. To calculate the FOM first the disk area, or the maximum area swept by the flapping airfoil is found. This is done by finding the maximum total Y -axis displacement of any point on the airfoil and multiplying it by the span. The swept area is denoted A_{disk} .

The induced velocity is the constant velocity induced in the fluid by an ideal actuator disk of area A_{disk} producing thrust, T and is calculated as follows:

$$V_{induced} = \sqrt{\frac{\bar{T}}{2\rho A_{disk}}} \quad (48)$$

The minimum ideal hover power is then given by:

$$P_{min} = \bar{T} V_{induced} \quad (49)$$

Finally the figure of merit is given by:

$$FOM = \frac{P_{min}}{\bar{P}_{required}} \quad (50)$$

The FOM and T/P should only be compared at the same disk loading which is given by:

$$T/A = \frac{\bar{T}}{A_{disk}} \quad (51)$$

8.2 3D model

The detailed description of the 3D model can be found in [10]. Only a brief overview is given below.

The 3D model was based on the 2D model. The main difference between the two is that the infinite vortex strands of the 2D model are replaced with quadrilateral vortex rings. The method of using rings for the bound and trailing edge wake vortices is taken from Katz and Plotkin [37]. The boundary conditions and the stall model are identical though implemented in three dimensions.

The numerical implementation of the 3D model differs from the 2D implementation primarily in the calculation of influence coefficients, in the use of reflection planes to model multiple wings, the 3D kinematics and some computational bookkeeping features used to facilitate the 3D implementation. The ring vortices also introduce some subtleties with respect to calculation of the pressure on the wing.

Complex 3D kinematics are created by superimposing several simpler, single degree of freedom motions. The flat, undeformed wing is first defined and then twisted and then any desired heave and flap motions are superimposed on the twisted wing. Wing twist is controlled by the user-set twist angles at the wing root and tip as well as a twist exponent. The smaller the twist exponent, the more twisting occurs inboard. In 3D, the flap motion is analogous to the Y-axis heave motion in 2D. Flapping refers to a motion like that of a bird's wing which pivots about a point at or near the root chord. Heave may occur along the X or Z axes. To model Mentor-type flapping kinematics, Z-axis heave is not needed, however, it is useful in reproducing the 2D test cases using a high AR wing for comparison and calibration. The X-axis heave occurs parallel to the flap axis and plays the same role as X-axis heave did in the 2D model.

In order to model clap-fling, the wings must come very close to one another. As a result of large amplitude flapping combined with twisting, portions of a wing may go outside its quadrant. This is both unrealistic, and may introduce numerical problems because of vortices occupying the same space. On the Mentor, the wings were not permitted to exceed their quadrant because of adjacent wings. At the extremes of the flap motion, adjacent wings would actually touch and remain touching until they began to move in the opposite direction. On Mentor, the peak to peak flap angle at the leading edge spar was approximately 76 degrees. However, because the wings were flexible, they would move more than this. The wings were

designed so that the leading edges flexed until they almost touched. To mimic this in the panel model, motion constraints were developed. Wing motion constraints prevented the wing from exceeding the limits of its quadrant, or some user-set subset of the quadrant. This was done at every time step by comparing the coordinates of every wing point to the reflection planes, or some small offset from these planes. The small offset is called the wing proximity parameter and in practice was less than 10% of chord. If, from one time step to the next, any point would have crossed that plane, the component of the position vector that is perpendicular to that plane is set to the plane value. It is held at this value until the wing kinematics dictate that the point is no longer violating the bounds of the proximity plane at which point the kinematic equations again fully drive the motion.

Reflection planes are used to reduce the computational time needed to model multiple wings. They can only be used for axi-symmetric flapping and when the freestream is aligned with the X-axis. The use of reflection planes does not reduce the number of influence coefficients that need to be calculated. The influence of the reflected wing on the actual wing still needs to be found. Rather, the use of reflection planes allows multiple wings to be modelled with the same number of unknowns as that present on a single wing. This is because when flow and flapping are axi-symmetric, the solution on every wing is identical. In the case of modelling four wings as on the notional NAV, this results in a four-fold reduction in the number of unknowns. Because much of the computational time is expended solving the system and the time is proportional to square of the number of unknowns, using reflection planes reduces the time required to solve the system of equations by a factor of sixteen.

The reference velocity used in the non-dimensionalization of forces and moments is the sum of the maximum wing tip velocity due to flapping (and not twisting or pitching) and the freestream velocity as given by:

$$V_{ref} = \sqrt{V_{\infty}^2 + (2\pi f \Psi b_{tip})^2} \quad (52)$$

Where Ψ is the flap angle amplitude in radians.

9 Optimum flapping motions identified from VLM

9.1 Optimization in two dimensions

9.1.1 Target disk loading

Comparisons of hover efficiency using either FOM or T/P ratio, should only be done at identical, or similar disk loadings. This holds true for any hovering vehicle whether it is a helicopter, a Harrier jump-jet or a dragonfly. Therefore in order to compare different flapping kinematics, a realistic disk loading with respect to the target NAV was established. All 2D optimizations will therefore be compared at a disk loading of 22.2N/m^2 . Note that for different 2D flapping kinematics, the disk area will vary, especially when vertical heave amplitude is manipulated. Therefore the disk area is calculated by finding the maximum total excursion of any part of the airfoil and multiplying this by the unit span. Because of this, in cases with vastly different flapping kinematics, even with this disk area correction, a perfect comparison is not guaranteed though it is far better than not attempting to match disk loading at all.

9.1.2 Thrust relationship to V^2

In the course of using the engineering model as a design tool for optimization an interesting relationship between mean thrust and flapping frequency was noticed. This relationship is very useful in cutting optimization time, and in scaling data. In a true hover, where $V_\infty = 0$, the thrust produced by a given flapping motion is directly proportional to the square of the flapping frequency. Because flapping velocity is proportional to flapping frequency, this is equivalent to saying that the force production is proportional to V^2 . This is consistent with the steady aerodynamic relationship between force and velocity. In a hover the instantaneous angle of attack and local velocity at the airfoil is a function only of the flapping kinematics ($V_\infty = 0$), therefore it is not altogether surprising that this relation holds.

Numerically, the scaling is done as follows. First a frequency scaling constant is calculated based on the actual reference velocity and thrust of the point to be scaled. Then the scaled frequency is calculated for the value of thrust that is desired. The desired thrust value is set based on the desired disk loading. A power scaling constant is then calculated based on the original power requirement and flapping frequency. Finally the new power requirement is calculated using the power constant and the scaled frequency.

9.1.3 Single variable optimization

Single variable optimizations were initially carried out because they illustrate the effect of each parameter, and serve to give a reasonable starting point for the multi-variable optimization. Furthermore, these single variable optimizations give a reasonable range over which each parameter should be varied to be utilized in the multi-variable optimizations. If the range for each parameter can be minimized, the optimization is less dependent on the starting point, is faster and more robust and is more likely to succeed in finding a global optimum. Also, if the optimum parameter is equal to one of the extremes of the range, it is obvious that the chosen range is inappropriate or the optimizer has found a solution that is outside the calibrated range.

The single variable optimization reported in [10] includes:

Y-axis Heave Phase Angle Optimization

Y-axis Heave Amplitude Optimization

Pitch Angle Amplitude Optimization

X-axis Heave Amplitude Optimization

X-axis Heave Phase Angle Optimization

Camber Amplitude Optimization

Camber Phase Angle Optimization

Optimization of Vertical Heave Phase Angle Given Higher Suction Efficiency

Wing Mass Optimization

Non-Sinusoidal Y-Axis Heave Dwell Time Optimization

9.1.4 Multi-variable optimization

Several different all-variable optimizations were run and three main promising kinematic “shapes” were identified. One optimum resembles a variation of a shape which roughly approximates the kinematics of Mentor. The second shape appears to utilize apparent mass as well as the pressure resulting from flow normal to the plate in order to produce force in the thrust direction. For reasons discussed in the report [10], the veracity of this optimum is more suspect and so it would be useful to corroborate this optimum with a Navier-Stokes solution. The third shape utilizes a large amount of pitching and little to no vertical plunging and resembles a fish tail type motion.

The result of one case, the fish tail type motion, is given here.

This optimum has a small heave amplitude and a large pitch amplitude as described below:

$30 \leq \Theta \leq 70$ degrees	$\Theta = 70$ degrees
$0.005 \leq H_Y \leq 0.06$ m	$H_Y = 0.006$ m
$60 \leq \delta_Y \leq 120$ degrees	$\delta_Y = 60$ degrees
$0 \leq H_X \leq 0.02$ m	$H = 0$ m
$-45 \leq \delta_X \leq -135$ degrees	$\delta_X = -97$ degrees
$250 \leq \delta_{\text{camber}} \leq 290$ degrees	$\delta_{\text{camber}} = 290$ degrees

This results in a motion that resembles a fish tail motion, or the motion used with a hand-held fan. This motion actually produced the best 2D efficiency with $T/P = 21.9$ g/W in a hover. This corresponds to a $FOM = 0.65$. In this case the non-sinusoidal motion parameters were available to the optimizer, however, because of the small heave motion resulting in this optimum, the non-sinusoidal motion had little effect. In fact, if the same optimum is run with sinusoidal motion, the result is nearly unchanged with $T/P = 23.4$ g/W which corresponds to $FOM = 0.69$. These values are not adjusted values but represent calculated solutions at the predicted scaled frequency. The forces are plotted in Figure 40. All run data is contained in the figure.

Note that this optimum has a higher degree of uncertainty since it deviates the most from the calibration cases. Furthermore, this level of performance is not captured when the parameters are run without camber

and the efficiency is exceptionally low ($T/P = 2.3$ g/W in a hover). The other optima yielded poorer performance without camber, but not to this degree. It is very probable that the performance here is an erroneous artefact of the camber implementation in the model. A Navier-Stokes solution would be useful here to confirm or dispute the performance of these kinematics.

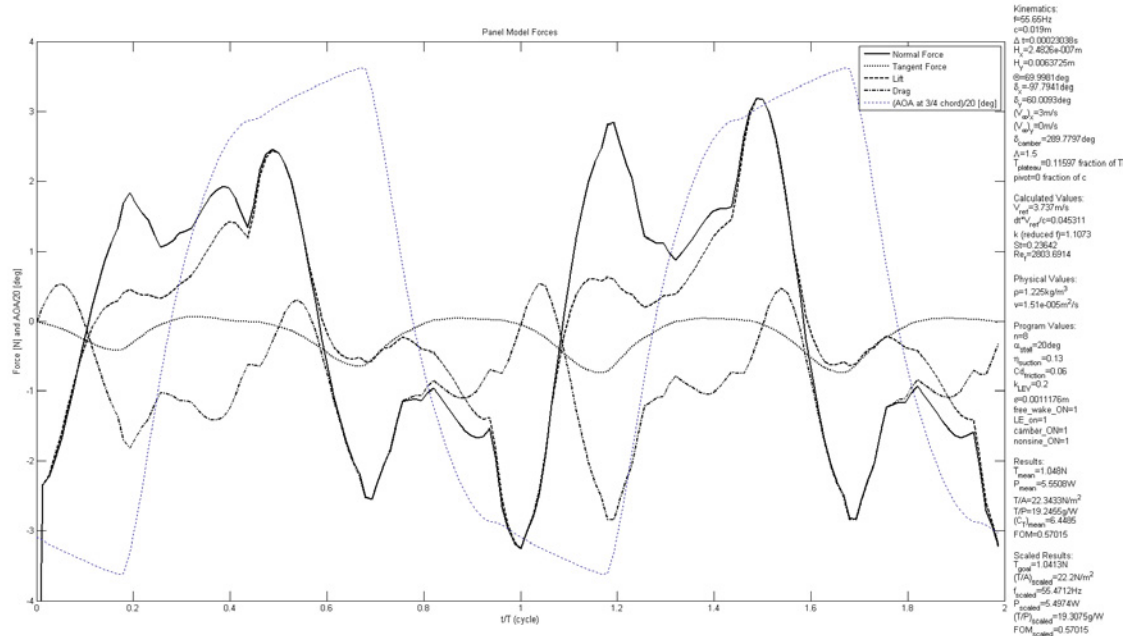


Figure 40: Forces resulting from fish-tail type optimum (2D)

9.2 Optimization in three dimensions

Several optimum wing planform and flapping kinematics were extracted from the VLM optimization tool and are well described in [10]. They are :

- Optimum suitable for the NRC water tunnel facility using a rigid wing (forward sweep not allowed)
- Optimum suitable for the NRC water tunnel facility using a rigid wing (forward sweep allowed)
- Optimum for a NAV rigid wing in air
- Optimum for a NAV rigid wing in air (reduced chord)
- Optimum for a NAV flexible wing (flap limited to 40 degrees)
- Optimum for a NAV flexible wing using clap-fling

The last two are described in the sections below

9.2.1 NAV flexible wing optimization (flap < 40 degrees)

This optimization sought to find the optimum wing planform and flapping kinematics to produce the target thrust within the dimensional restrictions of the NAV. Here a seven variable optimization was performed with the variables used, their bounds and the results listed here:

$-70 \leq \beta_{\text{tip}} \leq -40$ degrees	$\beta_{\text{tip}} = 60$ degrees
$0.01 \leq c_{\text{root}} \leq 0.04$ m	$c_{\text{root}} = 0.01$ m
$0.01 \leq c_{\text{tip}} \leq 0.04$ m	$c_{\text{tip}} = 0.04$ m
$70 \leq \delta_{\text{flap}} \leq 130$ degrees	$\delta_{\text{flap}} = 120$ degrees
$10 \leq \Psi \leq 40$ degrees	$\Psi = 40$ degrees
$-0.02 \leq d_{\text{tip}} \leq 0.02$ m	$d_{\text{tip}} = 0.008$ m
T/P = 10.49 g/W	

In this optimization the twist at the root was set to zero in order to reduce the number of manipulated parameters. Note, however, that the optimizer can still manipulate the twist exponent to give considerable twist at the root if this is found to be advantageous. In addition, the span variables were not included in this optimization because when they were, in other trial optimizations, they were inevitably pushed to the imposed limits so as to maximize disk area. This result is predicted by momentum theory alone.

This optimization was done with the separated-flow model active. In other words, it was done as realistically as possible using the present model. The resulting wing planform is shown in Figure 41. Note the small root chord and larger tip chord. This planform is the opposite of the Mentor planform which utilized a wing planform suitable for efficient lift production in steady flow. In other words, Mentor had a wing with a tip chord smaller than the root chord. It is hypothesized that the root chord was minimized in this case because with the reduced wing speeds at the root, thrust production is not as effective and so its area was minimized. With respect to a physical wing, the larger tip chord is actually helpful in achieving large twist angles because it increases the moment arm of the aerodynamic forces with respect to the primary spar located at the leading edge.

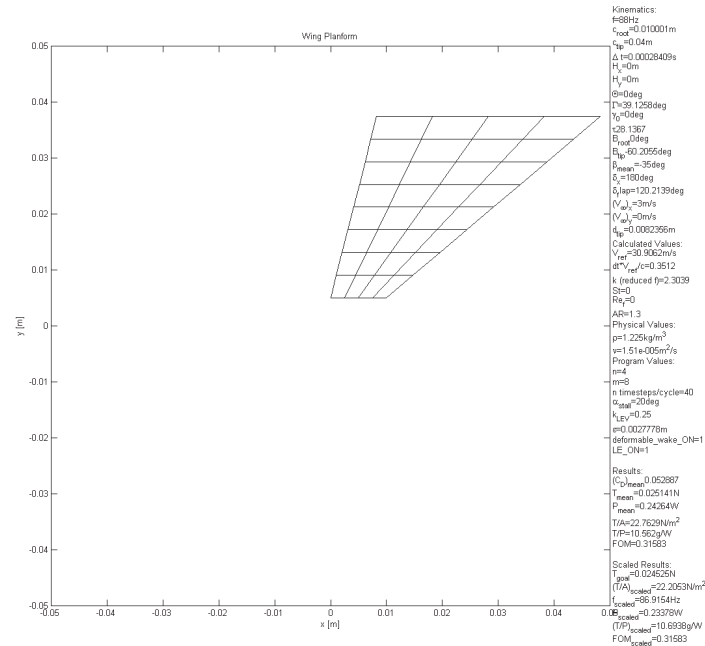


Figure 41: Optimal planform for flexible NAV wing

In addition, positive sweep was chosen by the optimizer and this has the effect of increasing the velocity of the wing near the tip due to the flapping motion. The sweep also allows wing twist to be achieved through both the bending and twisting of the leading edge spar and because of this it, would aid the passive aeroelastic twisting of the wing if large twist angles are desired. This in fact was the reason this optimum was selected for explanation here over others that had similar performance. This design appears very well suited to passive aeroelastic twisting. There were a few designs that had the same restrictions on chord and gave performance around $T/P = 10 \text{ g/W}$. Note that no substantially better solutions were found with similar chord restrictions. Lastly, the large tip chord coupled with a high twist angle has the result of increasing the actuator disk area as can be seen in Figure 42. It can be seen that the wing excursion considerably exceeds a circle with a radius equal to the semi-span value of 0.0375 m . If four wings were present in a clap-fling configuration, these excursions would be blocked and the disk area would be identical for all motions.

This optimization was run using $n = 4$ and $m = 8$ with 20 time steps per cycle since each solution took less than 10 seconds. After an optimum was found, the solution was solved using finer time steps such that there were 40 per cycle.

This optimization yielded a scaled thrust to power ratio of $T/P = 10.49 \text{ g/W}$ operating at the scaled frequency of $f = 88 \text{ Hz}$. When solved at this scaled frequency, the actual thrust to power ratio was $T/P = 10.69 \text{ g/W}$. The corresponding figure of merit is $\text{FOM} = 0.32$. This optimum was close to the required frequency predicted by scaling the Mentor parameters as discussed in the test case documents. Interestingly, if the same kinematics and planform are run with attached-flow the performance is slightly improved with $T/P = 10.97 \text{ g/W}$. Therefore in this case, the optimizer has found a solution where separation, and the leading edge vortex, has little effect.

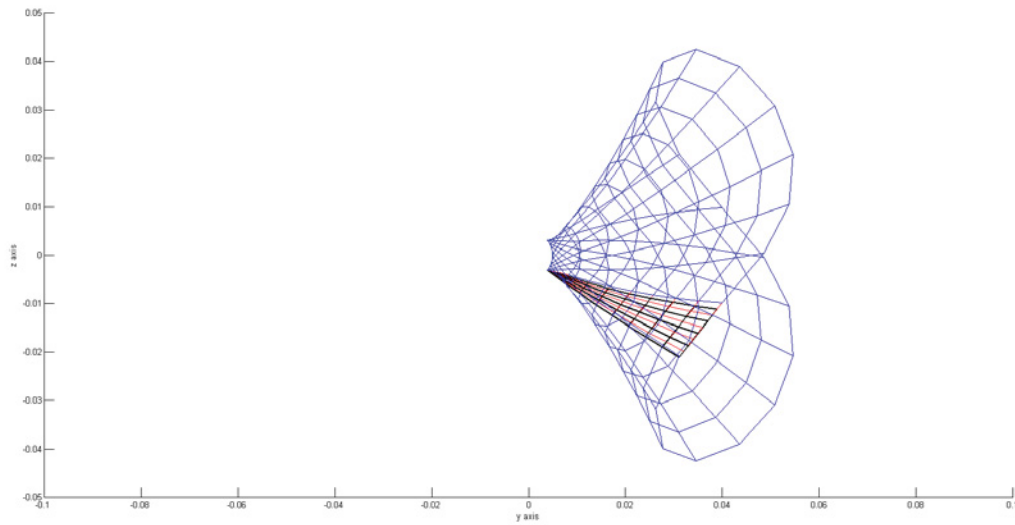


Figure 42: Rear view showing "time-lapse" of the wing's TE deformation

Note that this seven variable optimization was completed for a single wing with the flap amplitude limited to 40 degrees so that overall leading edge excursion was within the 90 degree quadrant, however the hard quadrant limits on the wing and the wake were not active and so the wing could exceed the quadrant due to twisting.

9.2.2 NAV flexible wing optimization (using clap-fling)

Optimizers are very good at exploiting any weaknesses in objective functions. One such weakness was found when the optimizer selected parameters that kept the wings pressed up against the quadrant boundaries for much of the cycle so that when the wings did begin to move away from the boundaries, the velocities and accelerations were very high. This in turn produced very large forces on the wings with unrealistically good efficiencies. Therefore to explore the role of clap-fling, which was experimentally proven to boost performance by up to 40 % on the Mentor program a single example of flapping kinematics, that did not exhibit the above described problem, was run both as an isolated wing and as a set of four wings operating in close proximity. In addition, a semi-free wake (more stable but less physical model) was used because it was found that a free wake would often be unstable when the reflection planes were used.

The single wing optimum used as the basis for this comparison is the optimum identified above in Section 9.2.1. For equitable comparison the same solution was recalculated using a semi-free wake and with attached flow and with the quadrant constraints in place. The resulting thrust to power ratio after two cycles is $T/P = 9.43 \text{ g/W}$ and the FOM = 0.28.

To investigate the role of clap-fling, these same flapping kinematics were re-run, except with four rather than one wing, with the wing and wake quadrant constraints turned on. The quadrant constraint plane was offset from the symmetry planes by $c=50$. In other words, the wings were allowed to come within $c=25$ of one another. In this case the thrust to power ratio was found to increase to $T/P = 14.45 \text{ g/W}$ which represents an increase of 53%. Here the $FOM = 0.43$. The increase in thrust to power is consistent with the experimentally measured results from the Mentor program. Part of the reason the power consumption is improved is because the clap-fling effect allows the same thrust production at a lower flap frequency and with power consumption proportional to the cube of frequency, this is a very useful effect. If the minimum separation distance was doubled to $c=12.5$ then the thrust to power ratio decreased such that $T/P = 13.34 \text{ g/W}$. Even when the gap is increased to 20% of chord, the benefit of clap-fling remains and $T/P = 11.53$ which represents a 20% increase in thrust to power.

One cannot, however, make the separation distance infinitesimally small with this model. For example, if the separation distance is reduced to $c=500$, the thrust to power ratio increases to the unrealistic value of $T/P = 383 \text{ g/W}$. Therefore in the absence of experimental calibration data for clap-fling cases, the separation distance is limited to the value of $c=25$ such that the thrust to power ratio only improves by approximately 50% which was shown to be achievable with Mentor and may represent a conservative value.

It should also be noted that a single wing with the quadrant constraints turned on does not exhibit the clap-fling improvement as expected. This shows that this effect within the model is not an effect of having the quadrant constraints and the particularities of how a flexible wing is treated in the model. It is the effect of multiple wings operating in close proximity.

Recall that for the optimized single wing, with a free wake, in a true hover the thrust to power ratio was $T/P = 12.6 \text{ g/W}$. It seems reasonable to postulate that clap-fling could be utilized to increase this value by 50% or possibly more. A 50% increase would mean that $T/P = 19.3 \text{ g/W}$ which corresponds to $FOM = 0.57$ which is just over the performance goal of $FOM = 0.5$ set out at the beginning of the program. Because this performance is not dependent on laminar or attached flow, but comes about from a calculation that includes the effects of separated flow, it is reasonable to expect the goal would also be achievable with an actual wing set.

This page intentionally left blank.

10 Fluid-structure interaction for flexible flapping airfoils in 2D

The CFD laboratory LMFN (Laboratoire de Mécanique des Fluides Numérique) at Laval University in Quebec City, under the supervision of professor Guy Dumas, has developed over the past several years a recognized expertise in the accurate numerical modelling of unsteady aerodynamic problems involving moving bodies and instantaneous, resulting force predictions. Eulerian CFD approaches (typically based on the finite volume code FLUENT also used at DRDC-Valcartier) as well as innovative lagrangian approaches (known as the "Vortex method") have been developed and successfully tested for various applications by the researchers of the LMFN.

Two Master's student projects were carried out at the LMFN on aeroelasticity problems with particular applications to the Aero-NAV project.

The first one considered the airfoil made up of a series of interconnected rigid members linked together by rotating joints characterized by inner angular springs and dampers. This approach may offer a better opportunity to control chordwise flexibility, and to optimise an actual wing design for certain criteria such as maximum energy efficiency or maximum force production.

The second one considered that the chordwise elastic deformation of the airfoil is continuous and depends on the material used and its thickness distribution.

10.1 Aeroelastic study of multi-segment wings in 2D

This Master's thesis project [17][18] studied chordwise flexibility effect on flapping-wings aerodynamics in low Reynolds number propulsion regime for nano-air vehicle applications. A fluid-structure interaction numerical solver, considering a wing as a series of interconnected rigid segments linked together by rotating joints, was developed and validated. This approach meant solving rigid body dynamics coupled with an incompressible flow. The lagrangian vortex particles method was used to solve the flow around multiple arbitrarily moving rigid bodies. The fluid-structure coupling implemented allows taking into account N rigid segments which dynamics is governed by an imposed motion on one of them, by instantaneous aerodynamic forces generated by the flow and by elastic forces in the hinges. Adding an extra subiteration loop to the vortex method was necessary to ensure a "strong" coupling fluid-structure interaction (FSI).

The development of this tool was used to study the impact of various discrete flexibility parameters in flapping-wing propulsion at low Reynolds number. Results indicate that a low flexibility could improve aerodynamic performances, if flexibility parameters (such as location and rigidity of the elastic joints) are chosen carefully. If not, performances could also deteriorate instead of benefiting from the flexibility effect. To obtain high efficiency and forces production, one has to make sure the wing deformation is governed by the aerodynamic forces and not by the wing inertia, which could induce a bad phasing between the deformation and the imposed motion of the wing. This work opens the way toward optimization of chordwise flexibility distribution for aerodynamic applications at low Reynolds numbers. Typical results are shown in Figure 43.

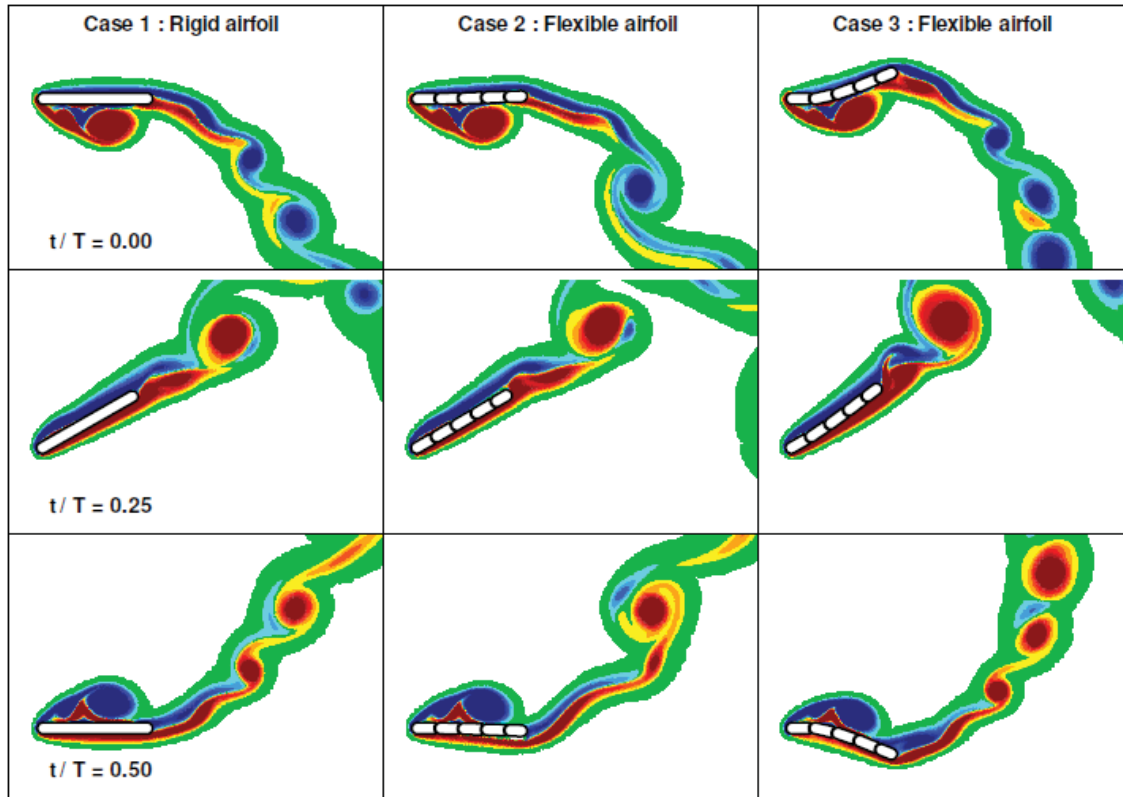


Figure 43: Computed vorticity field in propulsion regime at three instants over a flapping cycle, comparing a totally rigid wing (on the left) to two flexible wings.

10.2 Fluid-structure interaction using OpenFOAM

This Master's thesis project [12][16][19] studied 2D flexible flapping airfoils using a fluid-structure interaction solver. The governing equations associated to elastic solids with large deformations but small strains, and to incompressible fluids were used in the context of the unified theory of continuous media. The fluid-structure interaction solver is implemented in the OpenFOAM software.

The fluid-structure coupling is handled by an iterative partitioned algorithm where each field (the solid and the fluid) are treated separately. The spatial discretization is achieved with the segregated finite-volume method for both fields. The fluid module implements the Navier-Stokes equations using a SIMPLE algorithm whereas the solid module implements the St.Venant Kirchhoff constitutive law in a Lagrangian formulation where nonlinear and component-coupled terms are treated iteratively in a fixed point manner. Typical test simulations are carried out and results are found to be in good agreement with literature and with results from other software.

The results of flexible flapping wings simulations show that the solver is well suited for this kind of application. Furthermore, the analysis of the results provides information on the impact of dimensionless parameters on the physics of flexible flapping wings. It is shown that, in most cases, deformations associated to dynamic pressure are beneficial for thrust and efficiency whereas deformations caused by inertia are not unless care is taken to synchronise deformation mechanisms correctly. Typical results are shown in Figure 44.

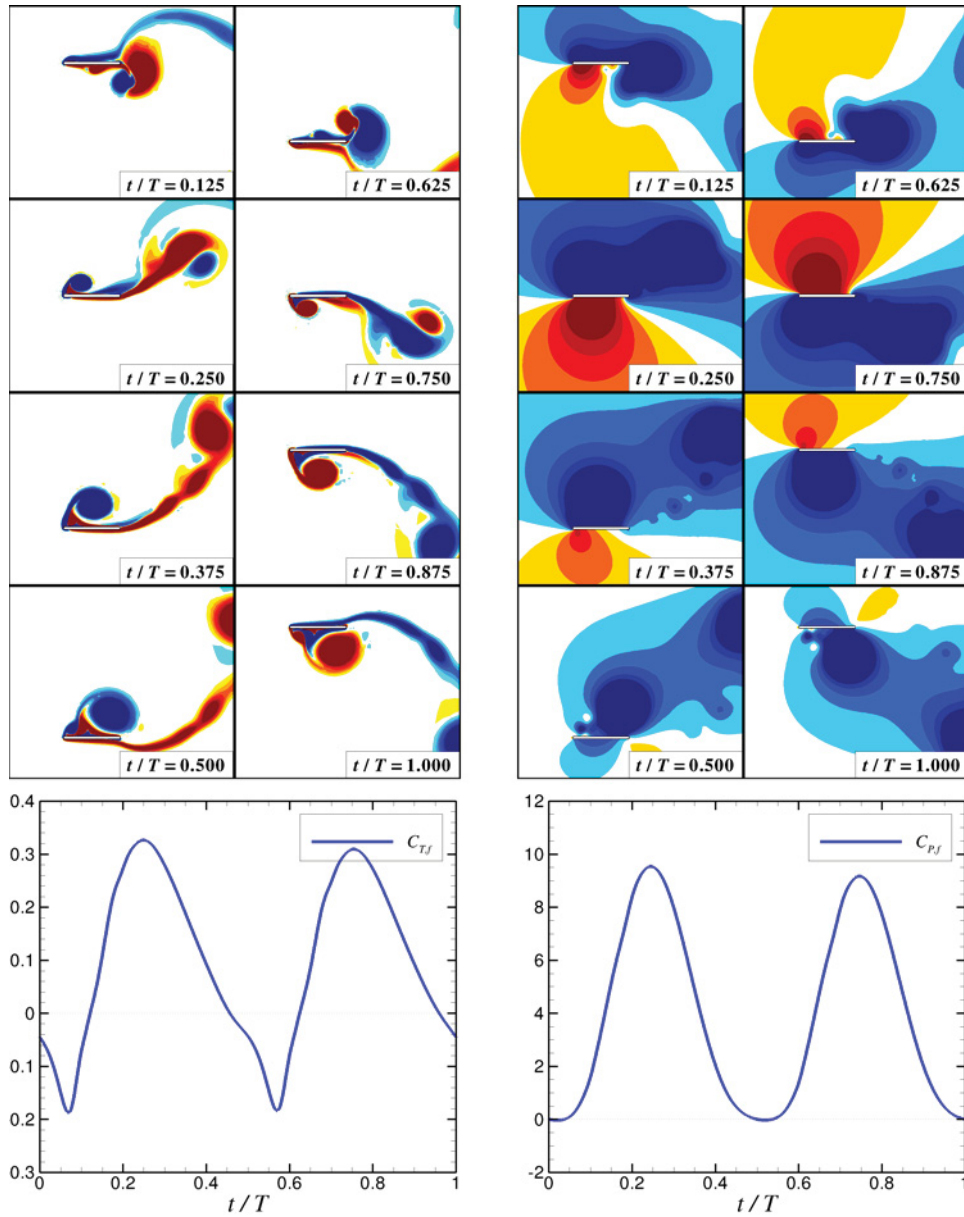


Figure 44: Case 100 : vorticity (top left) and pressure (top right) fields; instantaneous thrust (bottom left) and power (bottom right) coefficients

This page intentionally left blank.

11 Conclusion and recommendations

11.1 Novelty, Technical Advances, Knowledge Gained

The project was carried out over four years. The main accomplishments are:

- The definition of notional nano air vehicle to focus on particular dimensions, motion characteristics and performance parameters.
- The development of a two-dimensional and a three-dimensional test case representing the aerodynamics of the target vehicle flapping wing and that could be tested in the NRC water tunnel.
- The design, fabrication and preliminary testing of a rig to perform pitching and plunging two-dimensional tests in the water tunnel.
- A two-dimensional and three-dimensional time-stepping vortex-lattice model (VLM) capable of determining the aerodynamic forces generated and power consumed by the wings was developed.
- The development of an in-house 2D grid generating program (NRC).
- Two Master's theses on the modelling of wing flexibility in 2D and its impact on lift and thrust.
- The two-dimensional force and dye visualisation tests of the airfoil in water tunnel were completed. The high amplitude of the pitching and plunging motion, required for hovering, is a motion regime that was not studied previously and hence unique experimental data were acquired. The vortex fields and instantaneous vertical forces were compared with CFD.
- The two-dimensional force and dye visualisation tests of the airfoil with two opposite reflection planes to simulate clap-fling were completed. This simplified approach to simulate interactions of multiple wings through reflection planes allows the observation of larger vortices when the airfoil moves away from the reflection plane (or opposite wing).
- A 2-D flexible wing with one hinge point and a potentiometer was designed and fabricated. Water tunnel testing did not take place however because of the project ended before the system was operational.
- The existing 3D rig was improved (backlash reduced). The wings (flat plate and NACA0005) for the 3D test case were designed and built and force tests were carried out.
- The velocity field measurements (PIV) for the 2D tests were carried out.
- CFD computations of the 2D and 3D test cases were completed. The in-house INSflow code and the commercially-available Fluent code were both used to solve these unsteady incompressible flows. Among the challenges, there is the complex and large amplitude motion involving both pitch and plunge schedules of the wing and the time dependent simulation of the leading edge vortex and its subsequent trajectory past the airfoil, which required high grid resolution and accurate viscous closure models.
- A 2D and 3D time-stepping vortex-lattice model (VLM) capable of generating the aerodynamic forces generated and power consumed by the wings was completed. It solves the basic problem of modeling vortex shedding from both the leading and trailing edges of a flapping wing of arbitrary thin cross-sectional shape. The VLM is an engineering-type model where the variables are fewer and easily

manipulated compared to CFD, and can yield design rules and optima. The preliminary CFD results were used to calibrate the VLM which appears to provide results with quality sufficient for design purposes. The code is now adapted to be called by an optimization routine and was improved for much greater speed. The code is now running within multi-variable, multi goal, non-linear optimizer. Optimization results have been obtained for multiple flexible wings and the three rotations possible. The model was also used to produce results for the standard 2D and 3D test cases.

11.2 Project Successes

The main successes are:

- Based on system considerations, the general characteristics of a target NAV to be studied such as size, mass, and wing kinematics were established.
- The focus was on hovering, which requires high amplitude flapping and twisting motion not studied previously elsewhere.
- Optimization with the engineering method (VLM) identified several complex 3D flexible wing planforms and flapping kinematics resulting in significantly improved thrust-to-power ratio while producing the target thrust.
- The engineering method was calibrated with results from CFD and water tunnel which captured with higher accuracy the complex unsteady fluid flow dominated by vortices.
- Experiments with a larger wing at a lower flapping frequency in a water tunnel allowed a match of the three main non-dimensional parameters: Reynolds number, reduced frequency and flapping amplitude to chord ratio. Special motion rigs and wings (flexible) were designed and built.
- The CFD was successful but challenging because of the complex and large amplitude motion of the wing and the time dependent simulation of the leading edge vortex and its subsequent trajectory past the airfoil, which required high grid resolution and accurate viscous closure models.

11.3 Intellectual Property

No Patent resulted from the project. However, two unique items resulting from the project are worth noting:

The engineering model for the aerodynamics of flapping wings using the vortex lattice method is a unique tool.

The design of the notional nano-air-vehicle based on Mentor is unique.

11.4 Impact of the Project

The impact of the project on Canadian Defence will be to provide advice on the potential and the perspectives of nano-air-vehicle for future military applications. The capabilities resulting from the project were presented at the Soldier System Technology Roadmap Workshop [14] and at the Matinée S&T at DRDC Valcartier [7].

The impact of the project on the scientific community has been contributions to TTCP (WPN KTA 2-25: Critical technologies for Micro-munitions) and RTO (AVT-149: Unsteady Low Reynolds Number Aerodynamics for MAVs) activities as well as presentations at various international conferences (AIAA, ICAS, CFDSC, CASI, UVS Canada). The project was successful for generating links between our team members and scientists from other laboratories working on similar or interconnected fields. All Canadian researchers interested in flapping wings are likely to have links with our team.

There are still many technical challenges before operational NAVs play a role in the battlefield (aero, navigation w/o GPS, power/propulsion efficiency, structures with multi-functions, command, communication and control, miniature sensors, manufacturing, autonomous operation). This project focused on one challenge (aero). The other challenges will have to be addressed in the future in order to study integrated NAV systems for the Forces.

11.5 Follow-on Plans

The follow-on to this project is still at the level of basic research. Universities should be involved. It could deal with some of the issues identified in the section above. The tools and the optimised configurations developed in the TIF project will serve in these further analyses.

Several companies with potential interests in NAVs have been contacted and were informed of the capability acquired under this project. There was however no immediate interest from them in a joint effort to pursue the development of the NAV design capability because they see the payoff too far away.

The logical plan to pursue the development would be, as a first step, to design and build a flapping-wing NAV at full scale (7.5 cm, 80 Hz) and to demonstrate the thrust and efficiency of the optimized configuration. This would be done with the simulation tools and experiments developed during the TIF project. The emphasis would be on aerodynamic performance; power source would be external, the wing motion would be generated with conventional mechanical components, and the flight path could be along a rail or cable. A physical demonstration would clearly establish the design capability and would reduce the risk for integrated systems.

A project to integrate technologies for full NAV capability demonstration could then follow.

11.6 Recommendations

There was a spectacular increase in research in this field worldwide over the last five years. It is therefore recommended that funding for a follow-on project be identified in order to (1) maintain the team and our current expertise, (2) be recognised as a credible contributor to this field when collaboration opportunities arise, and (3) maintain our awareness of the state-of-the-art.

This page intentionally left blank.

12 References

- [1] Lesage, F., Hamel, N., Huang, X., Yuan, W., Khalid, M., Zdunich, P., "Definition of a notional nano air vehicle and related test cases", DRDC Valcartier TM, to be completed
- [2] Lee, R., Levasseur, L., Hoogkamp, E., Yuan, W., "Experimental Study of FlappingWings for Nano-Air-Vehicles", NRC-IAR Aerodynamics Laboratory, LTR-AL-2011-0101, September 2011
- [3] Yuan, W., Lee, R., Khalid, M., "Summary of INSFlow Results", Sep 2011
- [4] Lesage, F., "Flapping wing aerodynamics for insect-sized UAVs", presented at the UASWG Workshop 2011, DRDC Suffield, Alberta, June 2011
- [5] Lee, R., Yuan, W., Levasseur, L., Hoogkamp, E., "Experimental Simulation of Flapping Wings for Nano-Air-Vehicles", AIAA 2011-3790, 29th AIAA Applied Aerodynamics Conference, Honolulu, Hawaii, USA, June 27-30 2011
- [6] Yuan, W., Lee, R., Hoogkamp, E., Khalid, M., "Numerical and Experimental Simulations of Flapping Wings", International Journal of Micro Air Vehicle, Vol. 2, No. 3, September, pp. 1174–1194, 2010
- [7] Lesage, F., Hamel, N., "L'aérodynamique du battement d'aile pour les drones de taille insecte", Matinées Science et Technologies, RDDC Valcartier, May 2010
- [8] Yuan, W., Lesage, F., Poirel, D., "Flapping-wing Aerodynamics Studies", NATO RTO AVT-184 on Characterization of Bio-Inspired Micro Air Vehicle Dynamics, Antalya, Turkey, 12-15 April 2010
- [9] Lesage, F., Hamel, N., Yuan, W., Lee, R., Zdunich, P., "Simulation and experiments of flapping wing aerodynamics used for NAV", presented at the 35th TTCP WPN TP-2 Panel Meeting, United Kingdom, April 2010
- [10] Zdunich, P., "Development and Application of a 3D Vortex Panel Method with Leading Edge Separation Suitable for Hovering Flapping-Wing Flight", DRDC Valcartier Contract Report CR 2010-124, March 2010
- [11] Yuan, W., Khalid, M., "Simulation of Insect-sized Flapping-wing Aerodynamics", AIAA 2010-67, 48th AIAA Aerospace Science Meeting and Exhibit, Orlando, Florida, Jan. 4-7 2010
- [12] Olivier, M., "Développements numériques en interaction fluide-structure appliqués aux ailes oscillantes flexibles", DRDC Valcartier Contract Report CR 2009-399, December 2009
- [13] Yuan, W., "Flow Analysis of a Flapping SD7003 Airfoil at Transitional Reynolds Numbers", AIAA 2009-3955, 27th AIAA Applied Aerodynamics Conference, San Antonio, June 22-25 2009
- [14] Lesage, F., "Flapping Wing Aerodynamics for Insect-Size Drones" – luncheon conference, Soldier Systems Technology Roadmap Workshop 1: Visioning and Future Capabilities, Gatineau, June 16-17 2009
- [15] Lesage, F., "Flapping wings for nano air vehicles", presented to Bob Walker, CEO DRDC, 8 June 2009

- [16] Olivier, M., Dumas, G., Morissette, J.-F., "A Fluid-Structure Interaction Solver for Nano-Air-Vehicle Flapping Wings", AIAA 2009-3676, 19th AIAA Computational Fluid Dynamics Conference, San Antonio, TX, June 2009
- [17] Morissette, J.-F., "Simulations aéroélastiques d'ailes oscillantes multi-segments par méthode vortex", DRDC Valcartier Contract Report CR 2009-400, December 2009
- [18] Morissette, J.-F., Dumas, G., "A Meshless Approach for Fluid-Structure Interactions Analysis in Flapping-Wing Flyers", CFDSC2009-5B3, 17th Annual Conference of the CFD Society of Canada, Ottawa, Canada, May 2009
- [19] Olivier, M., Dumas, G., "Non-Linear Aeroelasticity Using an Implicit Partitioned Finite- Volume Solver", CFDSC2009-5B1, 17th Annual Conference of the CFD Society of Canada, Ottawa, Canada, May 2009
- [20] Lesage, F., Hamel, N., Yuan, W., Khalid, M., Huang, X. Zdunich, P., "Aerodynamic design and analysis tools for flapping-wing nano air vehicles", UVS Canada 2008, Ottawa, Canada, November 2008
- [21] Lesage, F., Hamel, N., Yuan, W., Khalid, M., Huang, X., Zdunich, P., "Aerodynamic study of a flapping-wing NAV using a combination of numerical and experimental methods", AIAA 2008-6396, presented at the 26th Applied Aerodynamics Conference, Honolulu, US, August 2008
- [22] Zdunich, P., "Separated-Flow Discrete Vortex Model for Nano-Scale Hovering Flapping Wings", AIAA 2008-6245, presented at the 26th Applied Aerodynamics Conference, Honolulu, US, August 2008
- [23] Yuan, W., Khalid, M., Huang, X., "Computations of Flows past an Insect-Like Flapping Wing", AIAA 2008-6395, presented at the 26th Applied Aerodynamics Conference, Honolulu, US, August 2008
- [24] DeLaurier, J., "Flapping-Wing Research at University of Toronto Institute for Aerospace Studies", Matinées Science et Technologies, RDDC Valcartier, May 2008
- [25] Lesage, F., Hamel, N., Zdunich, P., Yuan, W., Lee, R., "Initial investigation on the aerodynamic performance of flapping wings for nano air vehicles", DRDC Valcartier TM 2007-550, February 2008
- [26] Yuan, W., Khalid, M., "Preliminary CFD Studies of Flapping-Wing Aerodynamics", Canadian Aeronautic and Space Journal, Vol. 54, No. 3/4, pp. 51-63, 2008
- [27] Lesage, F., Hamel, N., Yuan, W., Huang, X., Khalid, M., Zdunich, P., "Flapping Wings for Nano-air Vehicles - Project update", Proceedings of the 33rd TTCP WPN TP-2 meeting, Adelaide, Australia, November 2007
- [28] Hamel, N., Lesage, F., "Model Comparison of Viscous Flow over a Pitching and Plunging Wing for Nano-Air Vehicles", paper presented at the 15th Annual Conference of the CFD Society of Canada, Toronto, June 2007

- [29] Lesage, F., Hamel, N., Yuan, W., Huang, X., Khalid, M., Zdunich, P., “Flapping Wings for Nano-air Vehicles TIF project - 12pz12”, presented at the 3rd meeting of TTCP WPN KTA 2-25, Ottawa, Canada, April 2007
- [30] Yuan, W., Khalid, M., “Preliminary CFD Simulations of Flapping-Wing Aerodynamics”, paper presented at the 12th CASI Annual Aerodynamics Symposium, Toronto, Canada, April 2007
- [31] Zdunich, P., “System Considerations for directions to flapping wing aerodynamic studies – AERO-NAV Final Report”, DRDC Valcartier Contract Report CR 2007-087, Advanced Subsonics Inc, March 2007
- [32] Keating, T., “Flapping wings”, STIA Information Report #CTI-0041, NRC Canada Institute for Scientific and Technical Information, March 2007
- [33] Lesage, F., Hamel N., Yuan W., Huang X., Zdunich P., “Flapping Wing Aerodynamics for Efficient Insect-Size Crafts”, Proceedings of the 32nd TTCP WPN TP-2 meeting, Point Mugu, CA, US, October 2006
- [34] Zdunich, P., Bilyk, D., et al., "Development and Testing of the Mentor Flapping-Wing Micro Air Vehicle" *Journal of Aircraft*, Vol. 44, No. 5, 2007.
- [35] Huang, X., Brown, T., “Preliminary Experiment of Flapping Wing in Three-Degrees-of-Freedom Motion” paper presented at the 25th International Congress of the Aeronautical Sciences, Hamburg, Germany, September 2006
- [36] Katz, J., “A discrete vortex method for the non-steady separated flow over an airfoil.” *J. Fluid Mech.*, vol. 102, pp 315-328, 1981
- [37] Katz, J. and Plotkin, A., *Low Speed Aerodynamics*, 2nd ed., Cambridge University Press, New York, 2006, Chap. 15

This page intentionally left blank.

List of symbols/acronyms

2D	Two-dimensional
3D	Three-dimensional
A	Disk area
b	Span
Cd	Drag coefficient
CFD	Computational Fluid Dynamics
c	Chord
c_{ref}	Reference chord
c_{root}	Root chord
c_{tip}	Tip chord
d	Airfoil maximum thickness
DOF	Degree of freedom
DRDC	Defence Research and Development Canada
f	Frequency
FOM	Figure of merit
H	Plunge amplitude (at 58% of span)
H_x	Horizontal heave (2D)
H_y	Vertical heave (2D)
k	Reduced frequency
LES	Large Eddy Simulation
LEV	Leading edge vortex
m	Mass
MAV	Micro air vehicle
NAV	Nano Air Vehicle
PIV	Particel Image Velocimetry
r	Radius at 58% span
Re	Reynolds number
Re_f	Reynolds number based on frequency
$Re_{generalized}$	Generalized Reynolds number
Re_{RMS}	Reynolds number based on RMS wing speed
S	Arc length of path at 58% span
T	Thrust
t	time
T	Period
TIF	Technology Investment Fund
UAV	Unmanned air vehicle
UDF	User defined function
VLM	Vortex Lattice Method
V	Velocity
V_{∞}	Free-stream velocity
$V_{induced}$	Plunging induced velocity
V_{plunge}	Velocity of the wing
V_{ref}	Reference velocity
V_{RMS}	RMS value of wing's velocity
V_{yMax}	Maximum value of wing flap velocity
W	Weight
Γ	Flap angle amplitude

Θ	Rotational amplitude (peak value) (2D)
Ψ	Angular position of the wing due to flapping
α	Angle of attack
β_{tip}	Tip twist angle
δ	Phase shift
δ_{camber}	Camber phase angle
δ_x	Angle by which horizontal heaving lags pitching (2D)
δ_y	Angle by which vertical heaving lags pitching (2D)
γ	Flap angle
η_p	Propulsion efficiency
ν	Kinematic viscosity
θ	Pitch angle
θ	Rotational displacement (2D)
ρ	Fluid density

DOCUMENT CONTROL DATA		
(Security markings for the title, abstract and indexing annotation must be entered when the document is Classified or Designated)		
1. ORIGINATOR (The name and address of the organization preparing the document. Organizations for whom the document was prepared, e.g. Centre sponsoring a contractor's report, or tasking agency, are entered in section 8.) Defence Research and Development Canada – Valcartier 2459 Pie-XI Blvd North Quebec (Quebec) G3J 1X5 Canada		2a. SECURITY MARKING (Overall security marking of the document including special supplemental markings if applicable.) UNCLASSIFIED
		2b. CONTROLLED GOODS (NON-CONTROLLED GOODS) DMC A REVIEW: GCEC JUNE 2010
3. TITLE (The complete document title as indicated on the title page. Its classification should be indicated by the appropriate abbreviation (S, C or U) in parentheses after the title.) Aerodynamics of flapping wings: Aero-NAV project final report		
4. AUTHORS (last name, followed by initials – ranks, titles, etc. not to be used) Lesage, F.; Hamel, N.; Yuan, W.; Zdunich, P.; Lee, R.		
5. DATE OF PUBLICATION (Month and year of publication of document.) August 2013	6a. NO. OF PAGES (Total containing information, including Annexes, Appendices, etc.) 104	6b. NO. OF REFS (Total cited in document.) 37
7. DESCRIPTIVE NOTES (The category of the document, e.g. technical report, technical note or memorandum. If appropriate, enter the type of report, e.g. interim, progress, summary, annual or final. Give the inclusive dates when a specific reporting period is covered.) Technical Report		
8. SPONSORING ACTIVITY (The name of the department project office or laboratory sponsoring the research and development – include address.) Defence Research and Development Canada – Valcartier 2459 Pie-XI Blvd North Quebec (Quebec) G3J 1X5 Canada		
9a. PROJECT OR GRANT NO. (If appropriate, the applicable research and development project or grant number under which the document was written. Please specify whether project or grant.) 12pz12	9b. CONTRACT NO. (If appropriate, the applicable number under which the document was written.)	
10a. ORIGINATOR'S DOCUMENT NUMBER (The official document number by which the document is identified by the originating activity. This number must be unique to this document.) DRDC Valcartier TR 2013-012	10b. OTHER DOCUMENT NO(s). (Any other numbers which may be assigned this document either by the originator or by the sponsor.)	
11. DOCUMENT AVAILABILITY (Any limitations on further dissemination of the document, other than those imposed by security classification.) Unlimited		
12. DOCUMENT ANNOUNCEMENT (Any limitation to the bibliographic announcement of this document. This will normally correspond to the Document Availability (11). However, where further distribution (beyond the audience specified in (11) is possible, a wider announcement audience may be selected.) Unlimited		

13. **ABSTRACT** (A brief and factual summary of the document. It may also appear elsewhere in the body of the document itself. It is highly desirable that the abstract of classified documents be unclassified. Each paragraph of the abstract shall begin with an indication of the security classification of the information in the paragraph (unless the document itself is unclassified) represented as (S), (C), (R), or (U). It is not necessary to include here abstracts in both official languages unless the text is bilingual.)

The development of a new class of military systems known as Nano Air Vehicle (NAV) (7.5 cm and 10 g) is possible in the not too distant future as a result of technological progress in a number of areas. The NAVs will likely use flapping wings as there is strong evidence that, for very small craft, flapping-wing performance is superior to other options due to dynamic effects. This report summarizes the work done under the Aero-NAV project, a Technology Investment Fund project that investigated flapping wing aerodynamics for NAV applications. A vehicle concept was defined in order for the project to focus on particular dimensions, motion characteristics, and performance parameters. From this concept, simpler test cases were defined to assist in understanding the physical phenomena. Tools and capabilities were developed by combining high-accuracy predictions and experimentations with engineering modelling. The detailed flow physics were captured using a highly accurate unsteady CFD solution at low Reynolds number. A tailored experimental facility (water tunnel at NRC) was developed for flapping wings operating at high frequency with a complex 3-dimensional pattern. A less computationally intensive engineering-type method (Vortex Lattice Method) capable of capturing the fundamental aerodynamics and approximating the forces and moments generated over a wide range of wing motions, was developed and used to identify optimum wing shape and motion. Optimization results were obtained for multiple flexible wings giving a thrust-to-power ratio of 19.3 g/W.

Le développement d'une nouvelle classe de systèmes militaires connus sous le nom Nano Air Vehicle (NAV) (7,5 cm et 10 g) est possible dans un avenir pas trop lointain, à la suite des progrès technologiques dans un certain nombre de domaines. Ils utiliseront probablement des ailes battantes comme il y a des preuves solides que pour les très petits véhicules, la performance des ailes battantes est supérieure à d'autres options en raison des effets dynamiques. Ce rapport résume le travail réalisé dans le cadre du projet Aero-NAV, un projet du Fonds d'investissement technologique qui a étudié l'aérodynamique du battement d'aile pour des applications NAV. On a défini un concept de véhicule pour que le projet se concentre sur des dimensions, caractéristiques de mouvement et paramètres de performance particuliers. A partir de ce concept, on a défini des cas test simples pour aider à la compréhension des phénomènes physiques. On a développé des outils et des capacités en combinant des prédictions et des expérimentations de haute précision avec la modélisation d'ingénierie. On a capturé la physique détaillée des fluides à l'aide d'une solution CFD instationnaire à bas nombre de Reynolds. On a développé une installation expérimentale sur mesure (tunnel hydraulique au CNRC) pour des ailes battantes à haute fréquence avec un mouvement tridimensionnel complexe. On a développé une méthode d'ingénierie (méthode Vortex Lattice) demandant moins de capacité de calcul, capable de capturer l'aérodynamique fondamentale et d'approximer les forces et de moments engendrés sur une large gamme de mouvements d'ailes. On a utilisé celle-ci pour identifier une forme d'aile et de mouvement optimale. On a obtenu des résultats d'optimisation pour des ailes flexibles multiples donnant un rapport poussée-puissance de 19,3 g/W.

14. **KEYWORDS, DESCRIPTORS or IDENTIFIERS** (Technically meaningful terms or short phrases that characterize a document and could be helpful in cataloguing the document. They should be selected so that no security classification is required. Identifiers, such as equipment model designation, trade name, military project code name, geographic location may also be included. If possible keywords should be selected from a published thesaurus, e.g. Thesaurus of Engineering and Scientific Terms (TEST) and that thesaurus identified. If it is not possible to select indexing terms which are Unclassified, the classification of each should be indicated as with the title.)

flapping wings; nano air vehicle; flow physics; water tunnel; flexible wings; NAV

Defence R&D Canada

Canada's Leader in Defence
and National Security
Science and Technology

R & D pour la défense Canada

Chef de file au Canada en matière
de science et de technologie pour
la défense et la sécurité nationale



www.drdc-rddc.gc.ca